

**PRECIPITATION OF INTERMETALLIC PHASES FROM
RAPIDLY SOLIDIFYING ALUMINUM ALLOY**

**PRECIPITATION OF INTERMETALLIC PHASES FROM RAPIDLY
SOLIDIFYING ALUMINUM ALLOYS**

By

DAMON PANAHI

A Thesis

Submitted to the School of Graduate Studies

In Partial Fulfillment of the Requirements

For the Degree of

Master of Applied Science

McMaster University

©Copyright by Damon Panahi, July 2009

MASTER OF APPLIED SCIENCE (2009)
(Materials Science and Engineering)

McMaster University
Hamilton, Ontario

TITLE: Precipitation of Intermetallic Phases from Rapidly Solidifying Aluminum Alloys

AUTHOR: Damon Panahi, MSc (Iran University of Science and Technology)

SUPERVISOR: Dr. Dmitri V. Malakhov

NUMBER OF PAGES: iii , 139

Abstract

Despite all efforts during the last 30-40 years, the formation of metastable Fe-rich and Si-rich intermetallics in dilute aluminum alloys is still an unsolved mystery. Based on the equilibrium Al-Fe-Si phase diagram, in dilute aluminum alloys only one equilibrium intermetallic, namely $\text{Al}_{13}\text{Fe}_4$, is expected. It is known, however, that a rapid solidification, i.e. solidification at a high cooling rate, results in dozens of metastable phases seen in the as-cast alloys. It is firmly established that the greater the cooling rate (i.e. the rate of heat extraction), the greater the supercooling (supersaturation) achieved in the course of solidification.

Understanding the nature and a sequence of formation of these intermetallic phases precipitating from the supersaturated melt is at the centre of this research. In fact, this endeavor was launched to answer the following fundamental question: “What governs the formation of intermetallic c phases from a rapidly solidifying alloys, in general, and from aluminum alloys, in particular?” Prior to starting this investigation, it was believed that the concept of the driving forces for the beginning of precipitation originated by Miroshnichenko, Cahn and Hillert, could be used to explain experimental findings. Was that belief justified? Although a definite answer to this question has not been found, there are strong indications that the concept is likely operative, although it has to be refined by taking into account the surface energies.

To evaluate applicability of this concept to the formation of Fe-rich and Si-rich intermetallics in aluminum alloys, in this research an array of experimental information

related to microstructures of as-cast alloys having different compositions are obtained. Then, the collected experimental results are interpreted using the concept of the driving forces for the beginning of precipitation.

Acknowledgment

My foremost thank goes to my supervisor Dr. Dmitri V. Malakhov. I thank him for his patience and encouragement that carried me on through difficult times, and for his insights and suggestions that helped to shape my research skills. His valuable feedback contributed greatly to this dissertation.

I would also like to express my sincere gratitude to Dr. Sumanth Shankar, Professor Nikolas Provatas and Dr. Hatem Zurob for their invaluable guidance over the last two years. Their suggestion in research discussions provided me great opportunities to look at the challenging problems from different angles.

My sincere thanks also go to Dr. Mark Gallerneault, Dr. Paul A. Wycliffe and Dr. Kevin M. Gatenby from Novelis for their fruitful collaboration and sharing their research experiences with me. I especially would like to express my appreciation to Mr. Pierre Marois for his great help in analyzing the X-ray diffraction patterns of the intermetallic particles.

Appreciation also goes out to John Rodda, Doug Culley, Ed McCaffery, Connie Barry and to the materials department office staff for all the instances in which their assistance helped me along the way.

The generous support from Ontario Centres of Excellence (OCE) is also greatly appreciated.

My deepest gratitude goes to my parents for their unflagging love and support throughout my life. I am indebted to my father, Jalil Panahi, and my mother, Pourandokht Mohammad-Hosseini, for their unconditional care and love.

Last but not the least I must acknowledge my beautiful wife and best friend, Tannaz, for her patience and understanding during this research. Without her love, encouragement and generous support this dissertation was simply impossible.

Table of Contents

Chapter 1 (literatur)	1
1.1 Production of aluminum sheet.....	1
1.2 Iron-rich and Silicon-rich intermetallics in the Al-Fe-Si system.....	6
Al ₁₃ Fe ₄	10
Al ₆ Fe	11
Al _x Fe	13
Al _m Fe.....	16
Al ₉ Fe ₂	17
α-AlFeSi	18
β-AlFeSi.....	24
1.3 Theories explaining the formation of Fe-rich and Si-rich intermetallics in as-cast alloys....	27
1.3.1 Scheil- Gulliver model and metastable intermetallics	34
1.4 Driving forces for onset of precipitation	38
1.5 Effect of impurities in nucleation of metastable intermetallics.....	41
Chapter 2 (experimental observations)	44
2.1 Project objective and experimental approach	44
2.2 Experiments.....	46
2.2.1 Making the alloys	46
2.2.2 Casting (different cooling rates).....	49
2.2.3 Dissolution step (extraction of intermetallics).....	54
2.2.4 Microscopy observations	56
2.2.4.1 Optical Microscope.....	56
2.2.4.2 Scanning Electron Microscope (SEM).....	72
2.2.5 X-Ray Diffraction analysis	78
Chapter 3 (discussion)	81
3.1 Microstructural investigations	81
3.2 EDAX examinations	86

3.3	XRD results	87
3.4	The theory of driving forces for onset of nucleation	92
3.4.1	Scenario number one: FCC phase is not allowed to precipitate (Global Undercooling)	95
3.4.2	Scenario number two: FCC phase is allowed to precipitate	98
	Conclusions	105
Appendix #1:	ICP results.....	107
Appendix #2:	Weight fraction of the extracted particles in phenol dissolution step	108
Appendix #3:	XRD patterns	110
Appendix #4:	Solute redistribution (Scheil model, Lever rule)	122
Appendix #5:	Driving forces for onset of precipitation.....	126
Appendix #6:	Heat equation (temperature profile).....	131
References	135

Table of Figures

Chapter 1 (literature)

Figure 1-1	Mean consumption of Aluminum in Kg/Vehicle in European automobiles.....	1
Figure 1-2	Direct Chill casting (a) final product (b) schematic of the process.....	3
Figure 1-3	Different types of strip-casters (a) twin-roll caster (b) twin-belt caster (c) block-caster	5
Figure 1-4	Al-Si phase diagram	9
Figure 1-5	Al-rich corner of the equilibrium Al-Fe binary phase diagram.....	9
Figure 1-6	Liquidus projection near the Al-corner of the Al-Fe-Si phase diagram.....	9
Figure 1-7	Extracted crystal of plate-shaped $Al_{13}Fe_4$ by using butanol	11
Figure 1-8	SEM image of Al_6Fe fibers in deep etched sample, Al-3.0 wt % Fe, solidified at 1.24 mm sec ⁻¹	13
Figure 1-9	SEM image of Al_xFe grown at	15
Figure 1-10	Extracted dendrite-like particles of Al_mFe by using butanol	16
Figure 1-11	A group of Al_9Fe_2 particles in strip casting sample in Al-0.55 Wt%Fe-0.16 Wt%Si alloy	17
Figure 1-12	TEM pictures of a) q_1 and b) q_2 in Al-0.28 wt%Fe-0.13 wt%Si alloy	21
Figure 1-13	Morphology of α -AlFeSi in deep etched samples of Al-Mn-Mg0.5-Fe0.2-Si alloy, (type of the etchant is not specified in the paper).....	23
Figure 1-14	Different morphologies of α_c -AlFeSi in 6xxx Al series a) script particle formed at 5 mm/min b) cluster of blocky particles formed at 30 mm/min and c) elongated particles formed at 80 mm/min	23
Figure 1-15	Optical microscope images of a) δ - Al_3FeSi_2 and b) β - $Al_9Fe_2Si_2$ intermetallics....	25
Figure 1-16	Three different chemical composition diagrams reported by different researchers	26
Figure 1-17	Schematic representation of competitive nucleation and competitive growth between α and β	28
Figure 1-18	The influence of growth rate on required interface undercooling for rough and smooth surfaces	29
Figure 1-19	(a) Variation of cooling rate across the width of DC cast billets (b) Fir-tree zone in DC cast AA1200 sheet ingot, NaOH is used as the etchant.....	30
Figure 1-20	Suggested metastable AlFeSi liquidus surfaces by Langsrud	37
Figure 1-21	Driving forces for attainment of full equilibrium (a) and for onset of precipitation	39
Figure 1-22	Schematic of effect of supercooling on the Gibbs energy and driving forces of nucleation.....	39
Figure 1-23	Driving forces for onset of precipitation stable and metastable phases	40

Chapter 2 (experimental results)

Figure 2-1	System used for making the master alloys	48
Figure 2-2	Schematic of casting on the surface of the water-cooled copper mould	50
Figure 2-3	Ribbon formation by melt spinner	50
Figure 2-4	Different parts of the melt spinner donated by Novelis to McMaster university	51
Figure 2-5	Schematic of the casting step (different cooling rates)	53
Figure 2-6	a) Dissolution setup b) Phenol dissolution reaction	55
Figure 2-7	Microstructure of A1.G-Fe.3-Si.05 solidified in the graphite crucible at different magnifications - Optical Microscope.....	57
Figure 2-8	Microstructure of A1.C-Fe.3-Si.05 solidified in the copper mould at different magnifications - Optical Microscope.....	58
Figure 2-9	Microstructure of A1.W-Fe.3-Si.05 solidified on the water-cooled copper mould - Optical Microscope	59
Figure 2-10	Microstructure of A1.W-Fe.3-Si.05 solidified on the water-cooled copper mould - Optical Microscope	60
Figure 2-11	Microstructure of A2-Fe.3-Si.15 solidified in the graphite crucible at different magnifications- Optical Microscope.....	61
Figure 2-12	Microstructure of A2.C-Fe.3-Si.15 solidified in the copper mould at different magnifications- Optical Microscope.....	62
Figure 2-13	Microstructure of A2.W-Fe.3-Si.15 solidified on the water-cooled copper mould- Optical Microscope	63
Figure 2-14	Microstructure of A2.W-Fe.3-Si.15 solidified in the water-cooled copper mould- Different magnifications-Optical Microscope	64
Figure 2-15	Microstructure of A3.G-Fe.3-Si.45 solidified in the graphite crucible- Different magnifications Optical Microscope	65
Figure 2-16	Microstructure of A3.C-Fe.3-Si.45 solidified in the copper mould- Optical Microscope	66
Figure 2-17	Microstructure of A3.W-Fe.3-Si.45 solidified on the surface of the water-cooled copper mould- Optical Microscope (a) Free surface (b) Contact surface	67
Figure 2-18	Microstructure of A3-Fe.3-Si.45 solidified on the water-cooled copper mould- Different sections and magnifications- Optical Microscope	68
Figure 2-19	Microstructure of alloy #4 solidified in the graphite crucible- Different magnifications- Optical microscope	69
Figure 2-20	Microstructure of A4-Fe.5-Si.2 solidified in the cylindrical copper mould –Optical microscope	70
Figure 2-21	Microstructure of the of A4-Fe.5-Si.2 solidified on the water-cooled copper- Optical microscope (a) free surface (b) Contact surface	71
Figure 2-22	Microstructure of A4.Fe.5-Si.2 solidified on the water-cooled copper- different locations and magnifications- Optical microscope	72

Figure 2-23 SEM images of microstructure of the ribbons produced by melt spinner- A1-Fe.3-Si.05	73
Figure 2-24 SEM images of intermetallics observed in deep-etched sample of A1-Fe.3-Si.05 solidified in the graphite crucible.....	75
Figure 2-25 SEM images of intermetallics observed in deep-etched sample of A1-Fe.3-Si.05 solidified in the copper mould (a), (b) and (c) cross-linked rods (d) spiral-like particles (e) and (f) chest-bone morphology	76
Figure 2-26 SEM images of intermetallics observed in deep-etched sample of A1-Fe.3-Si.05 solidified in the water-cooled copper mould (a) and (b) dense population of rod-like and plate-like structures (c), (d) and (e) globular particles (f) connected globular particles (dumbbell-shaped precipitates)	77

Chapter 3 (discussion)

Figure 3-1 Different configurations of particles observed in the microstructures of the samples	81
Figure 3-2 schematic of the sample solidified on the surface of the water-cooled copper mould	83
Figure 3-3 Backscattered images from an aluminum alloy (Fe=0.55 wt% Si=0.62 wt%) solidified in a graphite crucible.....	85
Figure 3-4 Average amount of iron and silicon obtained from EDAX examinations in alloy #1 with 0.3 wt% Fe and 0.05 wt% Si	86
Figure 3-5 Average amount of iron and silicon in different intermetallics based on the reported results in literature.....	87
Figure 3-6 Structure factor $S(Q)$ of non-superheated and superheated an aluminum alloy with 1 wt% Fe showing the medium range order of composition $Al_{13}Fe_4$ in non- superheated sample.	92
Figure 3-7 Schematic of temperature profile development in a melt during casting.....	93
Figure 3-8 Driving forces for onset of precipitation when none of the phases (except liquid) are participating in the equilibrium.....	97
Figure 3-9 Scheil in the case when all phases are participating in the equilibrium for alloy #1 with Fe=0.3 wt% Si=0.05 wt%	100
Figure 3-10 Scheil when only liquid and FCC participate in the equilibrium for alloy #1 with Fe=0.3 wt% Si=0.05 wt%	101
Figure 3-11 Driving forces for onset of precipitation Vs Temperature (Scheil-Gulliver model)– A1-Fe.3-Si.05	102
Figure 3-12 Driving forces for onset of precipitation Vs Temperature (Scheil-Gulliver model)– A2-Fe.3-Si.15	102

Figure 3-13 Driving forces for onset of precipitation Vs Temperature (Scheil-Gulliver model)–
 A3-Fe.3-Si.45103
 Figure 3-14 Driving forces for onset of precipitation Vs Temperature (Scheil-Gulliver model) –
 A4-Fe.5-Si.2103

Appendix #3

Figure 1 XRD result of Alloy #1 (Fe=0.3 Si=0.05), Graphite Crucible112
 Figure 2 XRD result of Alloy #1 (Fe=0.3 Si=0.05), Copper Mould112
 Figure 3 XRD result of Alloy #1 (Fe=0.3 Si=0.05), Water-Cooled Copper Mould112
 Figure 4 XRD result of Alloy #1 (Fe=0.3 Si=0.05), Melt Spinner, Ribbon Thickness = 300 µm 113
 Figure 5 XRD result of Alloy #1 (Fe=0.3 Si=0.05), Melt Spinner, Ribbon Thickness = 150 µm 113
 Figure 6 XRD result of Alloy #1 (Fe=0.3 Si=0.05), Melt Spinner, Ribbon Thickness = 70 µm..113
 Figure 7 XRD result of Alloy #2 (Fe=0.3 Si=0.15), Graphite Crucible114
 Figure 8 XRD result of Alloy #2 (Fe=0.3 Si=0.15), Copper Mould114
 Figure 9 XRD result of Alloy #2 (Fe=0.3 Si=0.15), Water-Cooled Copper Mould.....114
 Figure 10 XRD result of Alloy #2 (Fe=0.3 Si=0.15), Melt Spinner, Ribbon Thickness = 300 µm
115
 Figure 11 XRD result of Alloy #2 (Fe=0.3 Si=0.15), Melt Spinner, Ribbon Thickness = 150 µm
115
 Figure 12 XRD result of Alloy #3 (Fe=0.3 Si=0.45), Graphite Crucible115
 Figure 13 XRD result of Alloy #3 (Fe=0.3 Si=0.45), Copper Mould116
 Figure 14 XRD result of Alloy #3 (Fe=0.3 Si=0.45), Water-Cooled Copper Mould, TOP OF THE
 SAMPLE.....116
 Figure 15 XRD result of Alloy #3 (Fe=0.3 Si=0.45), Water-Cooled Copper Mould, CONTACT
 SURFACE116
 Figure 16 XRD result of Alloy #3 (Fe=0.3 Si=0.45), Melt Spinner, Ribbon Thickness = 300 µm
117
 Figure 17 XRD result of Alloy #3 (Fe=0.3 Si=0.45), Melt Spinner, Ribbon Thickness = 150 µm
117
 Figure 18 XRD result of Alloy #3 (Fe=0.3 Si=0.45), Melt Spinner, Ribbon Thickness = 70 µm.117
 Figure 19 XRD result of Alloy #4 (Fe=0.5 Si=0.2), Graphite Crucible118
 Figure 20 XRD result of Alloy #4 (Fe=0.5 Si=0.2), Copper Mould118
 Figure 21 XRD result of Alloy #4 (Fe=0.5 Si=0.2), Water-Cooled Copper Mould.....118
 Figure 22 XRD result of Alloy #4 (Fe=0.5 Si=0.2), Melt Spinner, Ribbon Thickness = 300 µm.119
 Figure 23 result of Alloy #4 (Fe=0.5 Si=0.2), Melt Spinner, Ribbon Thickness = 150 µm119
 Figure 24 result of Alloy #4 (Fe=0.5 Si=0.2), Melt Spinner, Ribbon Thickness = 70 µm119
 Figure 25 XRD result of Alloy #1 (Fe=0.3 Si=0.05), Melt Spinner, Thickness = 150 µm,
 SUPER HEAT≥ 1000 °C120

Figure 26 XRD result of Alloy #2 (Fe=0.3 Si=0.15), Melt Spinner, Thickness = 150 μm ,
 SUPER HEAT \geq 1000 $^{\circ}\text{C}$ 120

Figure 27 XRD result of Alloy #3 (Fe=0.3 Si=0.45), Melt Spinner, Thickness = 150 μm ,
 SUPER HEAT \geq 1000 $^{\circ}\text{C}$ 120

Figure 28 XRD result of Alloy #4 (Fe=0.5 Si=0.2), Melt Spinner, Thickness = 150 μm ,
 SUPER HEAT \geq 1000 $^{\circ}\text{C}$ 121

Appendix #4

Figure 1 Schematic of concentration profiles in a solidifying system with complete liquid mixing
 and some solid state diffusion [Kurz_1986].....123

Figure 2 Solidification under equilibrium conditions (Lever rule).....125

Appendix #5

Figure 1 Illustration of the driving force for the beginning of precipitation of a stoichiometric
 binary phase α from a supersaturated liquid solution.....126

Figure 2 An example of how the driving force for the start of precipitation depends on the
 initial composition of melt (7).....128

Figure 3 Driving forces for onset of precipitation of two competing stoichiometric phases.....129

Figure 4 Illustration of how the likelihood of phase formation depends on the melt's
 composition.....130

Appendix #6

Figure 1 Heat balance in a three dimensional system132

Figure 2 Calculated temperature profiles across a 100 μm Al melt spun ribbon during cooling
 and solidification (initial attained undercooling in this simulation is considered 100 K)
134

Figure 3 Calculate solid/liquid interface velocity V.s the position of the interface for different
 values of initial undercooling achieved in the region adjacent to the surface of the
 copper drum.....134

1. Chapter 1

1.1 Production of aluminum sheet

Aluminum was, is and likely always will be in the centre of attention as one of major materials in such areas as structural applications, architectural, machine tools, electrical conductors, and especially in the transportation area: aircrafts, ships, road vehicles and etc.

Among all these applications, casting of aluminum in the form of sheet for different applications (especially for body panels of road vehicles), has attracted significant attention among important industries such as auto makers. The trend of aluminum content in road vehicles in European countries shown in Figure 1-1 is an example of this growing interest.

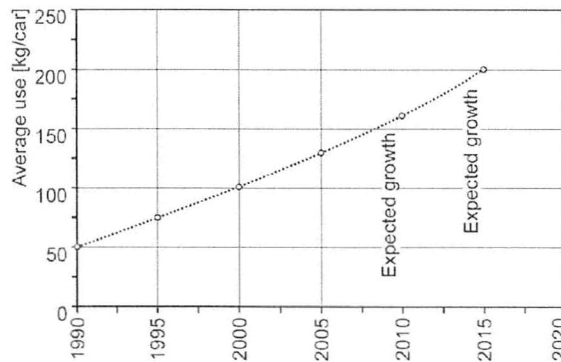


Figure 1-1 : Mean consumption of Aluminum in kg/Vehicle in European automobiles [Smolej 2002]

Annual statistic reports in the USA show that wrought aluminum alloys make a great portion of the total aluminum consumed. Over 65 percent of these alloys are in the form of sheets, plates and foils [Plunkert 1999]. It is worth mentioning that the

world aluminum production statistics show that around 40 percent of the annual world aluminum products are in the form of flat rolled sheets [Allen 1998] which indicates the importance of these types of products.

Table 1-1 U.S. NET SHIPMENTS OF ALUMINUM WROUGHT AND CAST PRODUCTS,
(All numbers are in thousand metric tones) [Plunkert 1999]

	1998	1999
Wrought products:		
Sheet, plate, foil	4,760	5,040
Rod, bar, pipe, tube, shapes	1,560	1,620
Rod, wire, cable	551	573
Forgings (including impacts)	110	118
Powder, flake, paste	54	54
Total	7,040	7,410
Castings:		
Sand	134	NA
Permanent and semipermanent mold	511	NA
Die	584	NA
Other	119	NA
Total	1,350	NA
Grand total	8,390	NA

Aluminum alloys can be divided into two major groups: wrought alloys, which are generally subjected to further processes such as rolling, and cast alloys, which are used to be cast into near final shape products. Among different methods available for shaping aluminum products; casting as one of the major production methods always receives a great attention.

In general, aluminum cast products can be categorized into three major groups including 1) ingot casting for re-melting, 2) shape casting, in which aluminum is directly casted into the final shape (no further deformation is needed), and 3) casting of aluminum alloy in the form of bars, stripes, billets and sheets for further working into extrusions, forgings, wire, rod, bar, and a variety of rolled products.

In the third group, over 90 % of aluminum sheets are produced with Direct Chill (DC) casting in which large rectangular or cylindrical billets (as huge as 10 meter in length and 1 meter in diameter) of alloys are made (Figure 1-2). After an extensive thermo-mechanical process, produced billets are transformed into aluminum sheet with desired thicknesses [Allen 1998]. Considering the amount of deformation and heat treatment steps, one can expect a completely different microstructure from as cast products i.e. depending upon the composition and expected application, different groups of intermetallics will be seen in the microstructure.

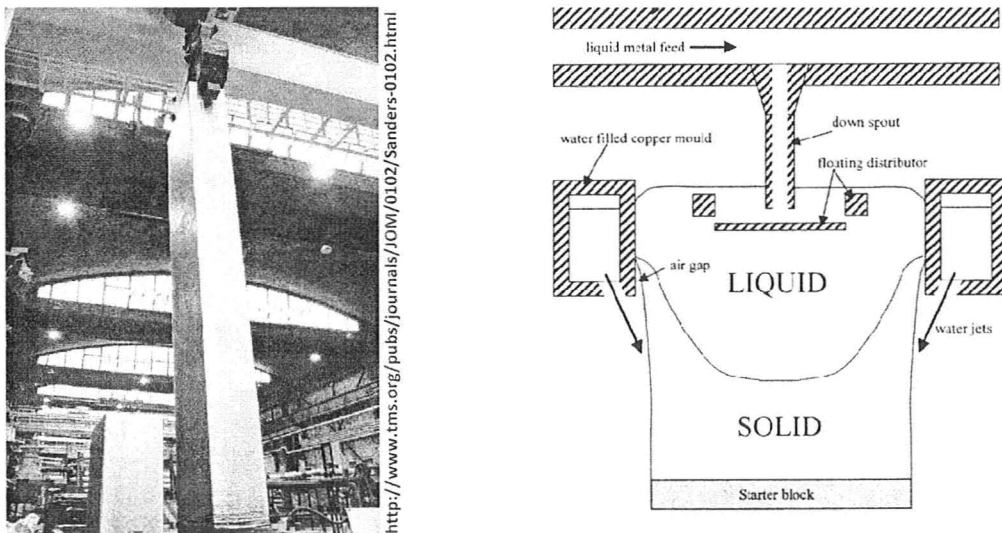


Figure 1-2 Direct Chill casting (a) final product (b) schematic of the process [Allen 1998]

Another major method for production of aluminum sheets is continuous casting (CC) in which a thin stream of molten alloy comes in contact with a cooled substrate and rapidly solidifies in the form of sheet or strip.

Moderate post-casting treatment (such as rolling) and as a result, more cost effective products is the main attractiveness of this method over other types of procedures [Altenpohl 1998].

There are three major types of casters which are widely used for production of wide strips:

1. **Twin-roll casters:** which are suitable for alloys with a short freezing range such as 3XXX series or pure aluminum. Width of the strips produced by this method usually varies between 1500 to 2000 mm (Figure 1-3-a).
2. **Twin-belt casters:** in which molten metal solidifies between rotating steel belts. And results in the production of slabs with 15-20 mm thick and up to 1500 mm wide (Figure 1-3-b).
3. **Block-casters:** in which a molten metal is solidified by using a chain of water-cooled steel mold blocks rotating like caterpillar tracks. This method is usually used for production of strips of up to 600mm width (Figure 1-3-c).

There are other types of strip casters which are used for production of narrow strips up to 300 mm wide.

Beside these industrially favorable properties, it is worth noticing that partially inherited as-cast microstructure in strip cast products and existence of inevitable metastable intermetallics in inter and intra-dendritic regions of microstructure, has limited their applications in many areas including the body panels of road vehicles.

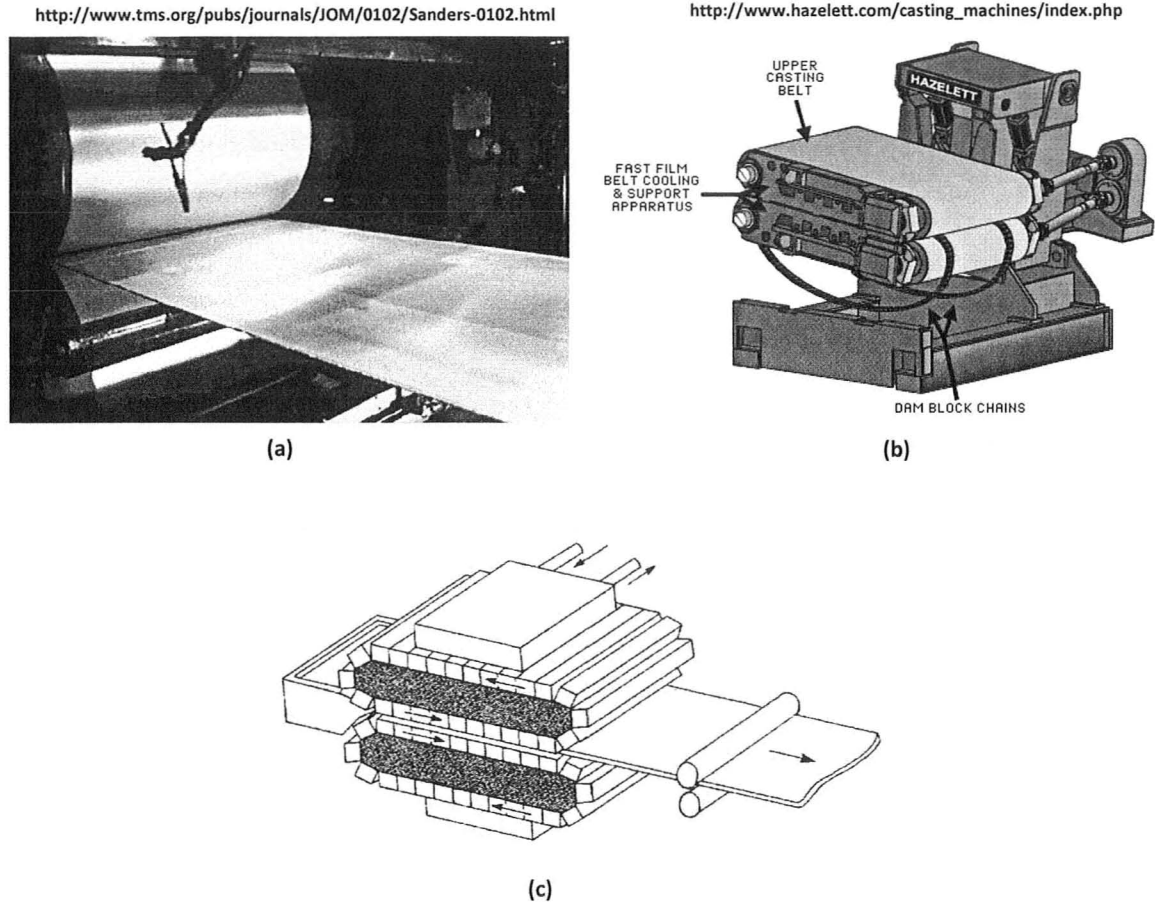


Figure 1-3 Different types of strip-casters (a) twin-roll caster (b) twin-belt caster (c) block-caster [Altenpohl 1998]

In other word, despite a low amount (less than 5 vol %) of these intermetallics in as cast microstructure, nucleation and growth of common binary (Al-Fe) and ternary (Al-Fe-Si) intermetallics [Allen, O'Reilly 1998], have detrimental effects on both the properties (such as ductility) and performance of the alloy during service in subsequent steps.

For example, corrosion resistance and surface quality of aluminum sheets can be affected by cathodic nature of Al_3Fe and $\alpha\text{-AlFeSi}$ to aluminum matrix [Khalifa 2003].

This can be crucial in some sensitive products such as high quality lithographic printing sheets [Allen 1998].

Inter-dendritic distribution of plate-like β -AlFeSi particles and their negative effects on mechanical properties of products is also another example of injurious effect of these intermetallics [Khalifa 2003].

It can be concluded that controlling and manipulating the formation of the metastable intermetallics during “non-equilibrium solidification” are of great technological interests. In fact, these are the key parameters which despite all efforts done in this area, still have many unclear aspects from both academic and industrial points of interest. A comprehensive understanding of the governing factors can significantly affect the aluminum industry in general, and especially those which are dealing with aluminum sheet products.

It is worth mentioning that in the present research the term “non-equilibrium solidification” is used for the conditions of solidification which result in deviation from the phase portrait predicted by equilibrium phase diagram.

1.2 Iron-rich and Silicon-rich intermetallics in the Al-Fe-Si system

Iron is almost always present in commercial aluminum alloys. As a result of its very low solid state solubility in the aluminum matrix (maximum 0.04 wt % in binary Al-Fe system), iron is rejected into interdendritic regions during solidification [Todd 1996].

It is seen from the equilibrium Al-Fe phase diagram (Figure 1-5) that in aluminum alloys with less than 37 wt% Fe one may expect the formation of $Al_{13}Fe_4$ in the interdendritic spaces. Surprisingly, a number of intermetallics such as Al_6Fe , Al_xFe , Al_mFe , Al_9Fe_2 , and Al_pFe which are not seen in the equilibrium phase diagram have been reported in literature [Griger 1996, Allen 1998, Todd 1996]. These kinds of deviations from equilibrium are usually related to the non-equilibrium solidification conditions such as solidification at high cooling rates.

In the presence of Si, the situation is even more complicated. The equilibrium Al-Si phase diagram is shown in Figure 1-4. Low solid state solubility of silicon, which results in the rejection of silicon into the interdendritic spaces and its possible interaction with iron, increases the complexity of the conditions during solidification. For example, some authors [Khalifa 2003] believe that during rapid solidification, the lowered diffusivity of Fe in aluminum matrix resulting from the presence of silicon, affects the iron content at interdendritic regions and consequently, possibility of the formation of some phases may be influenced.

In Al-Fe-Si alloys (with the liquidus projection is shown in Figure 1-6), depending on the composition and casting conditions, ternary intermetallics such as α -AlFeSi, β -AlFeSi and δ -AlFeSi, or both ternary and binary intermetallics, may form throughout the microstructure.

Traces of both Fe and Si are almost always present in commercial aluminum alloys. It is worth mentioning that in these Al-Fe-Si alloys there is no specific limit of Si or Fe concentration below which systems can be considered as binary. However, since 0.1-0.2 wt% of silicon can be accommodated in the structure of both the Al matrix and Al-Fe intermetallics, some authors believe that one should not expect a significant difference (in terms of type of the metastable intermetallics) between Al-Fe and Al-Fe-Si alloys with Si content less than 0.1 wt%. At least, in DC casting and other conventional industrial casting processes (sand casting, lost foam and etc.), in which very high solidification rates are not attained, these differences are not expected. Based on this, Allen *et.al* [1998] recommended that alloys with less than 0.1 wt% Si should not be considered as ternary systems i.e. could be treated as binary systems.

As mentioned before, the formation of these metastable phases is usually related to the non-equilibrium solidification conditions occurring during industrial processes. It was observed that depending upon solidification conditions and composition of the alloys, the nature and sequence of the formation of these intermetallics could be completely different. Surprisingly, in some cases, different authors have reported various assemblies of intermetallics in alloys having the same composition and solidified under similar conditions [Todd 1996].

All these firmly established experimental findings suggest that one cannot rely solely on the traditional thermodynamics, which deals with equilibrium condition, for

explaining these findings. In fact it seems that kinetic parameters, such as atomic mobility, and other features of non-equilibrium solidification, i.e. competitive nucleation and competitive growth, should also be employed to justify these peculiar observations [Allen 1998].

To do so, one should be intimately familiar with different types of binary and ternary intermetallics, their characteristics and solidification conditions under which these phases are usually seen.

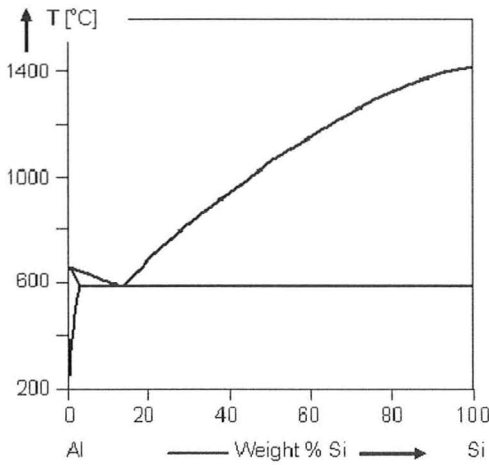


Figure 1-4: Al-Si phase diagram

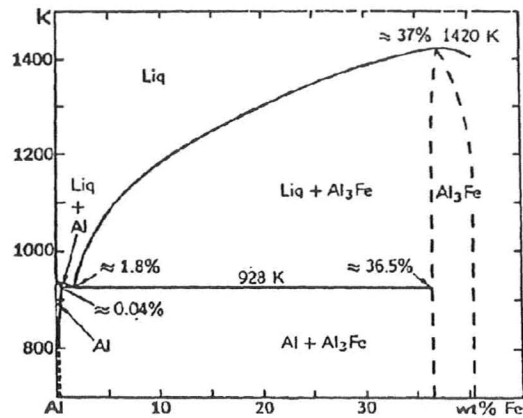


Figure 1-5: Al-rich corner of the equilibrium Al-Fe binary phase diagram [Allen 1998]

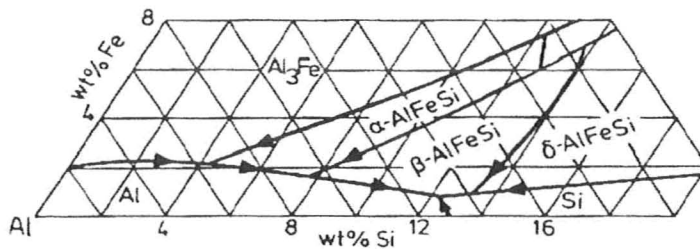
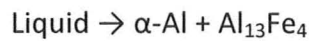


Figure 1-6: Liquidus projection near the Al-corner of the Al-Fe-Si phase diagram [Skejerpe 1987]

$\text{Al}_{13}\text{Fe}_4$

According to the equilibrium phase diagram, this phase with chemical composition of $\text{Al}_{13}\text{Fe}_4$ (also sometimes denoted as Al_3Fe or θ) is the only intermetallic phase anticipated in Al-Fe alloys with less than 36.5 wt% Fe. As seen in Figure 1-5, this phase is formed as a result of a eutectic reaction at around 655.1 °C [Allen 1998, Liang 1992].



This phase is usually present as large needle- [Allen 1998, Skejperpe 1987] or plate-shaped [Skejperpe 1987] precipitates with C-face centered monoclinic structure. It is structurally isomorphous with $\text{Al}_{13}\text{Co}_4$ [Simensen 1977] and contains 100 atoms per unit cell [Allen1998]. A typical extracted $\text{Al}_{13}\text{Fe}_4$ particle, using high purity butanol (some details can be found in [Gupta 1996]), is shown in Figure 1-7. The crystallographic information of this phase is presented in Table 1-2.

Reportedly [Todd 1996, Wang 1998], in solidification of Al-Fe alloys, increasing both the growth rate and cooling rate, transforms the morphology of θ phase from faceted plate-like to non-faceted rod-like particles at triple points and interdendritic spaces. In the presence of Si, the situation is different: platelets of $\text{Al}_{13}\text{Fe}_4$ are seen at all growth rates in which $\text{Al}_{13}\text{Fe}_4$ is stable. In other words, silicon stabilizes the faceted plate-shaped morphology.

The reason for this morphological transformation lies behind the faulted crystals structure of $\text{Al}_{13}\text{Fe}_4$ with different layers of stacking faults and twinning planes ((001) and (100)) [Skejerpe 1987]. Presence of Si in Al-Fe alloys, promotes the formation of 100 twinning system which is rarely seen in the structure of θ phase in pure Al-Fe alloys. Todd *et.al* concluded that as a result of the presence of these faults on the surface of $\text{Al}_{13}\text{Fe}_4$ particles, faceted structure becomes energetically more favorable at high solidification front velocities [Todd 1996].

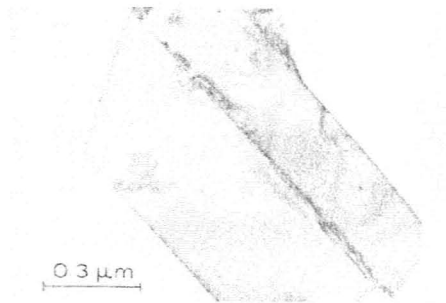


Figure 1-7 Extracted crystal of plate-shaped $\text{Al}_{13}\text{Fe}_4$ by using butanol [Skejerpe 1987]

Al_6Fe

Al_6Fe , with C-face centered orthorhombic structure and 28 atoms per unit cell, is a commonly seen intermetallic in as-cast DC billets. It is well established that usually at low cooling rates or low growth velocities (i.e. small deviation from equilibrium conditions*) Al_6Fe displaces $\text{Al}_{13}\text{Fe}_4$ via a eutectic decomposition (3.0 wt% Fe). Different

* Condition which leads to the formation of equilibrium phases predicted by the binary equilibrium phase diagram

researchers have reported different temperatures, ranging from 652.9°C [Liang 1992] to 640°C [Khalifa 2003], as the eutectic temperature.

Al₆Fe is structurally isomorphous with Al₆Mn and as a result is highly promoted in the systems containing Mn [Allen 1998]. The crystallographic information of this phase is presented in Table 1-2.

The influence of Si, which has a very low solubility in its lattice (maximum 0.5 wt% Si) [Allen 1998], on the precipitation of this phase is an important but not completely clear question. It is believed that the effect of Si content is very significant in the formation of this phase. For example, Tibbals says "... it is the Si content that determines whether the slowly nucleating Al₆(Mn,Fe) or the more rapidly forming α-phase nucleates from the liquid or from the solid solution" [Tibbals 1990]. It is usually mentioned in the literature that because of the low solid solubility of Si in the structure of Al₆Fe, the formation of this phase is limited in ternary systems containing silicon [Allen 1998].

Reportedly, rod-like non-faceted morphology, which is the common form of Al₆Fe particles in DC cast alloys (Figure 1-8), can be changed both by variation in composition and change in solidification conditions. For example, an inclination toward the formation of plate-like faceted structures in the presence of Mg in the alloy [Hughes 1977]. In another case, the tendency of Al₆Fe fibers toward the formation of

the plate-like structures by decreasing the growth rates or increasing the iron content of the alloy has been reported by some researchers [Hughes 1977].

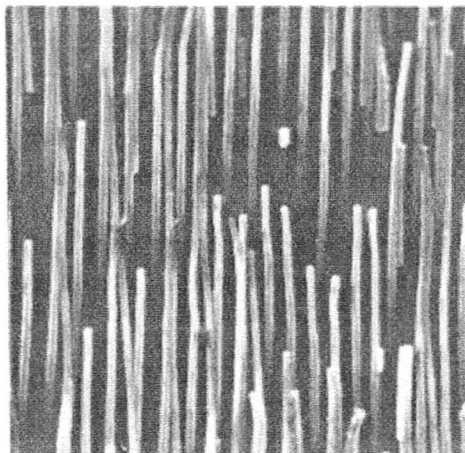


Figure 1-8 SEM image of Al_6Fe fibers in deep etched sample, Al-3.0 wt % Fe, solidified at 1.24 mm sec^{-1}

[Hughes *et al.*1977]

Al_xFe

In general, this phase has a complex morphology with dendrite-like growth [Todd 1996]. It rarely appears in the binary Al-Fe alloys, but usually seen in systems containing other alloying elements as either alloying elements or impurities [Griger 1990]. Two types of Al_xFe have been identified by different groups of researchers: one with $X=5.6-5.8$ [Khalifa 2003, Skejperpe 1987, Skejperpe *et al.*1987, Westengen 1982] and one with $X=4.5-5.0$ [Young 1981, Allen 1998].

In the first group ($X=5.6-5.8$), the crystal structure is not completely clear; but, despite irregular diffraction patterns obtained from TEM investigations, Skejperpe [1987] suggested a C-centered orthorhombic structure (similar to Al_6Fe) which contains

complex stacking faults resulting from the presence of Si. The similarity between identified cell parameters of Al_xFe and Al_6Fe and close Fe contents in these two phases, suggest a structural relation between Al_xFe and Al_6Fe [Skejerpe, Gjonnes 1987].

In the second group ($X=4.5-5.0$), Young *et al.* [1981] and Wang *et al.* [1998] suggested the monoclinic structure for Al_xFe crystals. The reported crystallographic information is presented in Table 1-2. Wang [1998] showed that the stability of Al_xFe is strongly affected by the presence of small amounts of such alloying elements as vanadium. Also, he showed that the morphology of Al_xFe was a strong function of growth conditions and would be changed from plate-like to lamellar and rod-like structure and eventually from rod-like to cellular structure by increasing the growth rate. This variation of morphology has been shown in Figure 1-9 for Al-2.8Fe-0.12V alloy in different growth rates [Wang 1998].

In general, complex conditions of the formation of Al_xFe , has turned this phase to a rather mysterious intermetallic. It is seen that by increasing cooling rate or growth velocity, Al_xFe will appear either before or after the formation of Al_6Fe [Young 1981, Todd 1996]. These discrepancies between observations can be contributed to the various alloying systems with different purity levels used by different researchers [Khalifa 2003].

Transition from Al_6Fe to Al_xFe by increasing the growth velocity can be justified by considering the Si content of these intermetallics. Todd and Jones [1996] explained

that at high solidification front velocities, less opportunity for Si atoms to diffuse across Al_6Fe boundaries (with low Si solubility) into the liquid makes Al_xFe with higher Si solubility, more favorable than the supersaturated Al_6Fe structure.

The opposite transformation (Al_xFe to Al_6Fe) reported in some systems however, is still unclear. In some publications [Todd 1996], it is attributed to the effect of other alloying elements (e.g. Mg) and their contributions in reducing the available Si content of the system via the formation of other intermetallics (e.g. Mg_2Si). As a result, this can favor the formation of such phases as Al_6Fe which has low Si content.

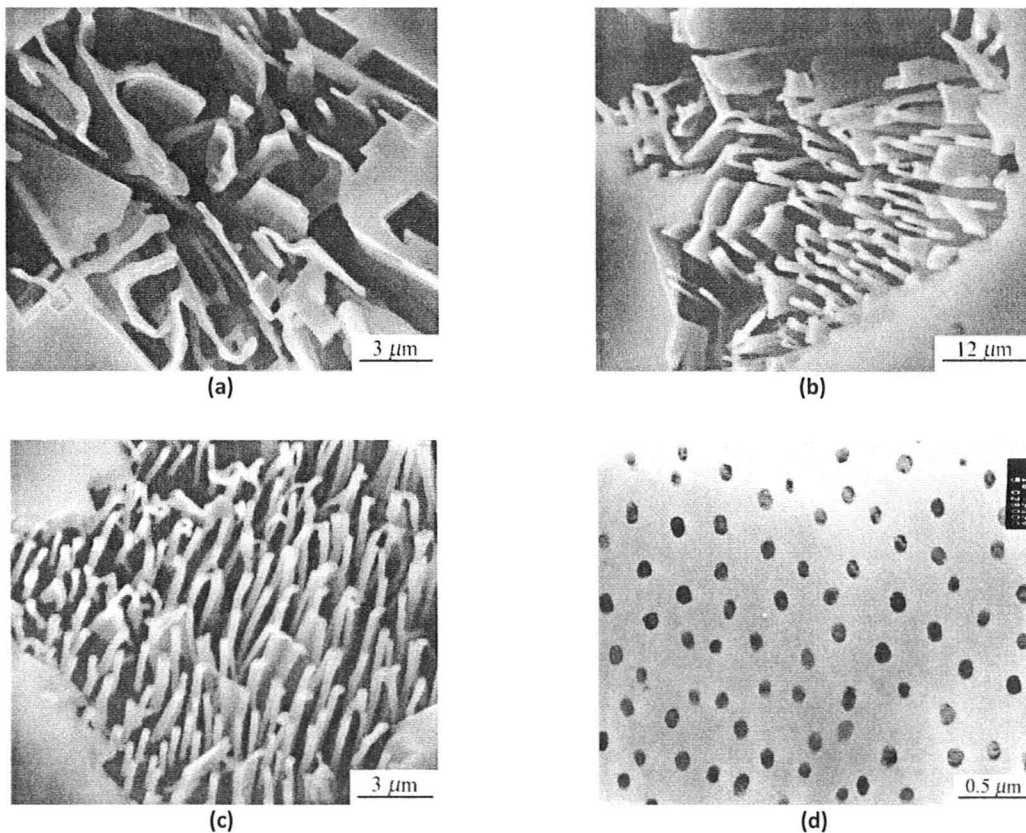


Figure 1-9 SEM image of Al_xFe grown at
a) $200 \mu\text{m/s}$, b) $340 \mu\text{m/s}$, c) $510 \mu\text{m/s}$, d) TEM image at $810 \mu\text{m/s}$ [Wang 1998]

Al_mFe

Body centered tetragonal Al_mFe is another common metastable intermetallic in Al-Fe as-cast products. It is usually seen in outer parts of ingots where cooling rate is higher (more than 10^3 K/s) compared to interior parts [Skejerpe 1988, Westengen 1982, Khalifa 2003]. It is reported that Al_mFe generally has a faulted structure in which by increasing the cooling rate, i.e. getting closer to the ingot surface, the defect density increases [Skejerpe1988].

Considering the dendrite-like morphology of Al_mFe , many researchers suggest a metastable eutectic decomposition with a temperature ranging from $649.5^\circ C$ [Allen, O'Reilly 1998] to $610^\circ C$ [Khalifa 2003] for the formation of this phase.

In EDX investigations It is seen that in the presence of Si, the structure of this phase with $m=4.0-4.4$ (20-22 Fe atoms out of 110 to 120 atoms in total [Skejerpe1988]), can usually accommodate more than 1 wt% Si [Westengen 1982, Langsrud 1990]. Reported lattice parameters of this phase can be found in Table 1-2.

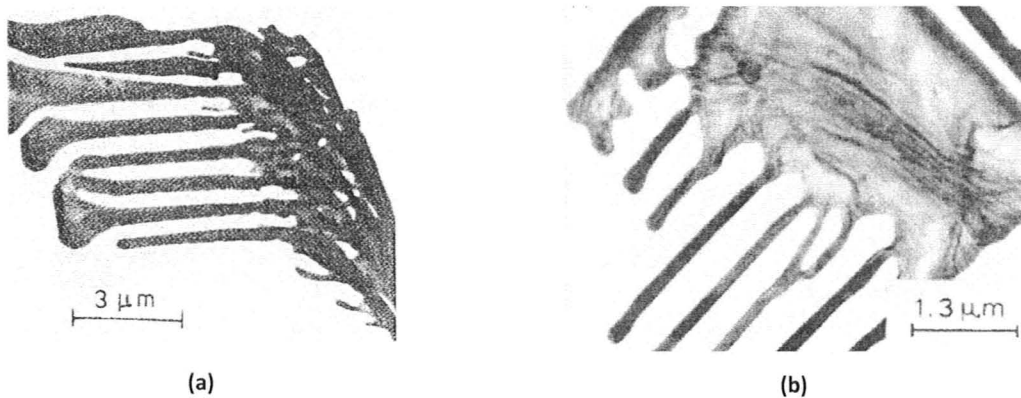


Figure 1-10 Extracted dendrite-like particles of Al_mFe by using butanol (a) [Skejerpe1988] (b) [Skejerpe 1987]

Al_9Fe_2

Al_9Fe_2 is not a very common metastable intermetallic in aluminum alloys and is not reported in many publications. Similar to Al_xFe , it is usually present in the Al-Fe alloys containing either impurities or other alloying elements [Griger1990].

It was first identified by Simensen *et al.* [1977] with monoclinic crystal structure and 80 wt% Al, 20 wt% Fe and usually less than 1 wt% Si. Though common morphology (Figure 1-11) of this phase suggests a eutectic transformation [Simensen 1977]; solidification conditions resulting in the formation of this phase are still unclear [Allen 1998].

It was found that Al_9Fe_2 could be promoted in strip cast materials in the presence of Co. This may be related to the strikingly isomorphous structure of this phase with Al_9Co_2 [Simensen 1977].

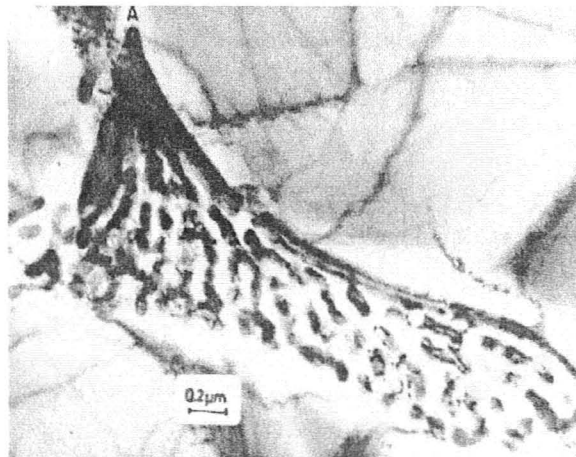


Figure 1-11 A group of Al_9Fe_2 particles in strip casting sample in Al-0.55 Wt%Fe-0.16 Wt%Si alloy [Simensen 1977]

Table 1-2 Crystallographic information of binary intermetallics in Al-Fe alloys, [Allen1998]

Phase	Bravais lattice	Lattice parameter
$\text{Al}_{13}\text{Fe}_4$	c-Centered monoclinic	$a = 15.49 \text{ \AA}$ $b = 8.08 \text{ \AA}$ $c = 12.48 \text{ \AA}$ $\theta = 107.75^\circ$
Al_6Fe	c-Centered orthorhombic	$a = 6.49 \text{ \AA}$ $b = 7.44 \text{ \AA}$ $c = 8.79 \text{ \AA}$
Al_xFe	c-Centered orthorhombic	$a \approx 6 \text{ \AA}$ $b \approx 7 \text{ \AA}$ $c \approx 4.7 \text{ \AA}$
Al_xFe	?	?
Al_mFe	Body centered tetragonal	$a = 8.90 \text{ \AA}$ $b = c = 31.6 \text{ \AA}$
Al_9Fe_2	Monoclinic	$a = 8.90 \text{ \AA}$ $b = 6.35 \text{ \AA}$ $c = 6.32 \text{ \AA}$ $\theta = 93.4^\circ$
Al_pFe^*	Body centered cubic	$a = b = c = 10.3 \text{ \AA}$

α -AlFeSi

Base on the equilibrium Al-Fe-Si phase diagram (Figure 1-6), depending on the chemical composition of the alloy, one may expect the formation of equilibrium intermetallics such as $\text{Al}_{13}\text{Fe}_4$ (θ phase), α -AlFeSi and β -AlFeSi via peritectic (θ and α -AlFeSi) or eutectic (β -AlFeSi) reactions (in the aluminum corner of the phase diagram).

* FeAl_p with a body centered cubic structure and $p=4.5$, is a very rarely seen phase. There is not much information available about this phase.

There is a good agreement among different researchers [Kral 2005, Warmuzek 1999, Simensen 1977, Turmezey 1990, Liu 1990] that usually under non-equilibrium solidification conditions and in the presence of other alloying elements (e.g. Mn and other transition elements) and impurities, the ternary stable intermetallics (α and β) choose another solidification path which leads to the formation of metastable forms of α -AlFeSi and β -AlFeSi with different compositions.

Kral [2005] has summarized different types of α -AlFeSi reported in literature (Table 1-3). He concludes that most of these α -AlFeSi intermetallics (with chinese script morphology) in aluminum alloys have cubic structure with $Al_{19}(FeMn)_5Si_2$ chemical formula.

Table 1-3 Characteristics of common types of phases named α -AlFeSi in literature [Kral 2005]

Phase	Structure	a (nm)	b	c	Notes
$Al_{19}Fe_4MnSi$	Cubic	1.256			dendritic
$Al_{12}Mn_3Si$	Cubic	1.2625			Dendritic, Chinese script
$Al_{12}Fe_3Si$	Cubic	1.2523			Chinese script
α -Al(Fe,Mn)Si	Cubic	1.266			
α -AlFeSi	Cubic	1.256			Metastable, stabilized by Mn
$Al_{15}(Fe,Mn)_3Si_2$	Cubic	1.25			
Al_8Fe_2Si	Hexagonal	1.23		2.63	

In dilute Al-Fe-Si alloys there are some rarely seen types of α -AlFeSi with monoclinic (α_v , q_1) and C-centered monoclinic (q_2) crystal structures which form non-equilibrium solidification conditions [Liu 1990]. Crystallographic information of these phases is shown in Table 1-4.

Liu [1990] reported that q_1 would transform to q_2 at 873K. TEM micrographs of these two intermetallics are shown in Figure 1-12.

Table 1-4 Rarely seen types of α -AlFeSi phase [Allen 1998, Liu 1990]

Phase	Structure	a (nm)	b (nm)	c (nm)	β	Notes
q_1 -AlFeSi	C-centered monoclinic	1.27	3.62	1.27		
q_2 -AlFeSi	Monoclinic	1.25	1.23	1.93	109 °	
α_v -AlFeSi	Monoclinic	0.89	0.635	0.632	93.4 °	high Si modified version of Al_9Fe_2 with 4.5-10.5 wt% of Si [Allen 1998]

It seems that other types of α -AlFeSi phases (such as α_T -AlFeSi and α'' -AlFeSi), which are sometimes reported in literature, should not be considered as distinct phases i.e. in fact they are structurally modified versions of other common types of α -AlFeSi intermetallics. For example, α'' -AlFeSi is an intermediate structure between Al_mFe and other common α -AlFeSi phases in terms of silicon content [Todd 1996] ; or, in another case, α_T -AlFeSi is a modified structure of cubic α which shows some super reflections in its TEM diffraction patterns [Allen 1998].

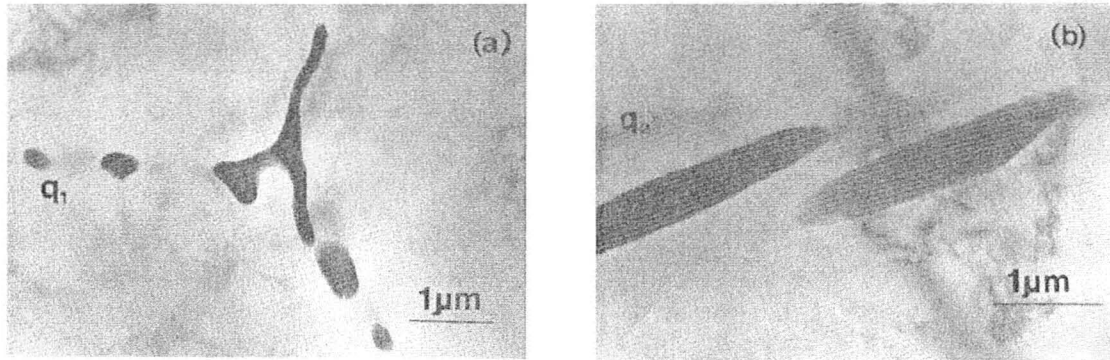


Figure 1-12 TEM pictures of a) q_1 and b) q_2 in Al-0.28 wt%Fe-0.13 wt%Si alloy [Liu 1990]

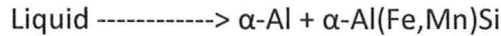
In general, in Al-Fe-Si alloys, depending on the composition in general, and the Fe/Si ratio in particular, and in the absence of impurities, stable α -AlFeSi with the hexagonal crystal is formed under very low solidification rates. It usually contains around 45 atoms of Fe, 24 atoms of Si and 168 atoms of Al per unit cell and is designated as Al_8Fe_2Si [Turmezey 1990]. Turmezey *et.al* reported that by increasing the initial amount of silicon in the alloy, the concentration of Si in Al_8Fe_2Si can vary from 7 % to 9.5 wt% [Turmezey 1990].

Under non-equilibrium solidification conditions such as high cooling rates (usually more than $10^\circ K/s$), hexagonal Al_8Fe_2Si is replaced with metastable forms of that with cubic or monoclinic structures some of which are listed in Table 1-3 and Table 1-4 [Kral 2005, Simensen 1977, Turmezey 1990].

As mentioned, among all different reported structures for α -AlFeSi, the cubic structure is probably the most common form of α -AlFeSi in commercially as-cast products which can adopt a range of different compositions and morphologies.

Warmuzek and Gazda [1999] reported two solidification paths through which metastable α -AlFeSi ($\text{Al}_{12}(\text{Fe,Mn})_3\text{Si}$ and $\text{Al}_{19}(\text{Fe,Mn})_5\text{Si}_2$) can be formed under non-equilibrium conditions:

In the first path, α -AlFeSi precipitates directly from the melt via a eutectic decomposition which results in $\text{Al}_{12}(\text{Fe,Mn})_3\text{Si}$ with branch-like morphology.



In the second path, precipitation starts on the surface of Al_6Fe intermetallics via a peritectic reaction.



The outcome of this reaction is metastable $\text{Al}_{19}(\text{Fe,Mn})_5\text{Si}_2$ (α -AlFeSi) with Chinese script morphology and a higher amount of Si than in the branch-like one.

SEM micrographs of these two morphologies are shown in Figure 1-13.

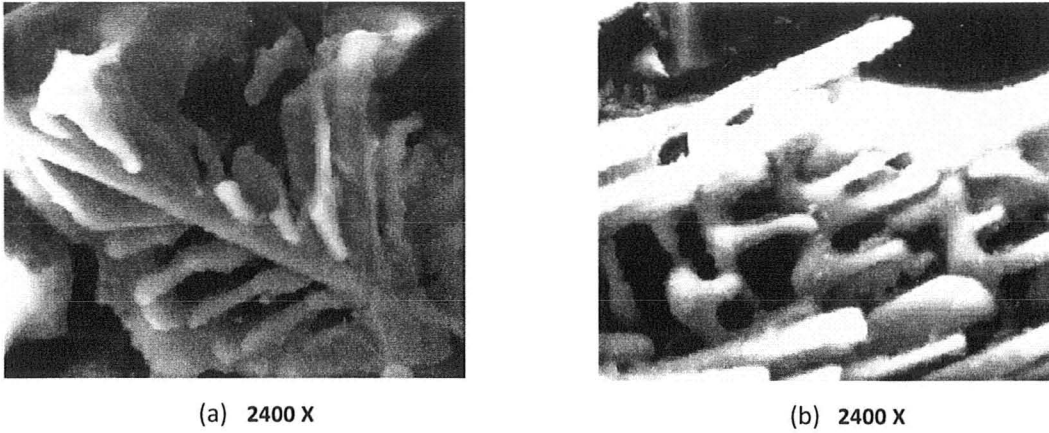


Figure 1-13 Morphology of α -AlFeSi in deep etched samples of Al-Mn-Mg0.5-Fe0.2-Si alloy, (type of the etchant is not specified in the paper)
 a) branch-like b) Chinese script [Warmuzek 1999]

Sha et.al [2006] reported both faceted and non-faceted morphologies for α -AlFeSi phase and stated that in 6xxx series aluminum alloys, “...various morphologies of cubic α_c -AlFeSi are likely to result from flexibility in its growth mechanisms”. Also, in terms of the crystal structure of α -AlFeSi, they reported that in the 6xxx series, “...cubic α -AlFeSi with a simple cubic structure can gradually evolve into bcc α_c -AlFeSi with increasing growth velocity above ~ 80 mm/min”. TEM images of some observed α -AlFeSi particles are shown in Figure 1-14.

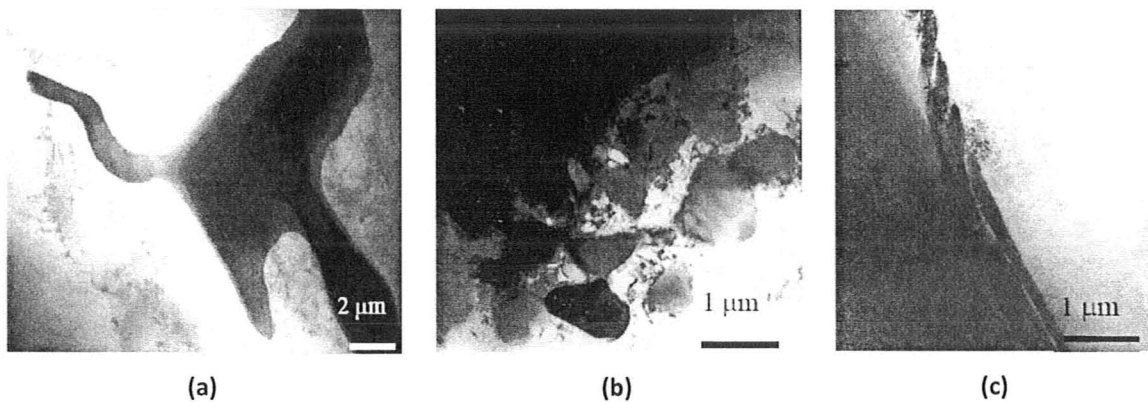


Figure 1-14 Different morphologies of α_c -AlFeSi in 6xxx Al series a) script particle formed at 5 mm/min b) cluster of blocky particles formed at 30 mm/min and c) elongated particles formed at 80 mm/min [Sha 2006]

β -AlFeSi

β -AlFeSi phase with plate-like morphology has the most harmful effect on the mechanical properties of aluminum alloys. As a result, in industrial alloys (e.g. 6xxx series) it is always attempted to promote the formation of other less detrimental intermetallics such as α -AlFeSi by adding other elements such as Mn, Co, Sr or by reducing the solidification rate in production lines [Kral 2006].

Considering only the morphology of particles, in some publications plate-like phases are referred as β -AlFeSi with monoclinic structure and Al_5FeSi stoichiometric composition [Kral 2005, Kral 2006]. It is worth mentioning that there are three major groups of plate-like β -AlFeSi intermetallics with three different crystal structures (orthorhombic, tetragonal and monoclinic) reported in literature. Crystallographic information of these phases, summarized by Kral [2005], has been presented in Table 1-5.

Zheng *et.al.* [2000] investigations show that β -AlFeSi particles are in fact a dual structure of orthorhombic and quasi-tetragonal crystals. This composite nature could be one of the reasons for having different crystal structures reported by different authors.

Also, Kral *et.al.* [Kral 2006] observed that in aluminum alloys with high silicon content (e.g. 11 wt% Si) , usually a blade-shaped tetragonal phase Al_3FeSi_2 (sometimes termed δ - Al_3FeSi_2) was the dominant plate-like structure which should not be mistaken

with other types of β -AlFeSi phase. Kral *et.al.* [Kral 2006] reported, “an approximately 1:1 (Fe):Si ratio for β phase and approximately 1:2 (Fe):Si ratio for δ phase”.

Table 1-5 Characteristics of common types of phases named β -AlFeSi in literature [Kral 2005]

Phase	Structure	a (nm)	b	c	Notes
Al_3FeSi_2	tetragonal	0.607		0.95	Plate-shaped
Al_4FeSi_2	tetragonal	0.612		0.948	
Al_4FeSi_2	tetragonal	0.611		0.946	t-AlFeSi thick tetragonal blades
$\text{Al}_9\text{Fe}_2\text{Si}_2$	monoclinic	0.611		4.14	m-AlFeSi, tetragonal blades, $\alpha_2=91^\circ$
$\beta\text{-Al}_{15}\text{FeSi}$	monoclinic	0.5792	1.2273	4.313	$\beta=98.93^\circ$
$\text{Al}_{15}\text{FeSi}$	monoclinic	0.612		4.15	thin plates
$\beta\text{-Al}_{4.5}\text{FeSi}$	monoclinic	0.6161	0.6175	2.081	square plates, $\beta=91^\circ$
$\beta\text{-Al}_5\text{FeSi}$	orthorhombic	0.618	0.620	2.08	in conjunction with a tetragonal phase
Fe_2SiAl_5	orthorhombic	0.6184	0.625	2.069	

Microscopic images from $\beta\text{-Al}_9\text{Fe}_2\text{Si}_2$ and $\delta\text{-Al}_3\text{FeSi}_2$ have been shown in Figure 1-15.

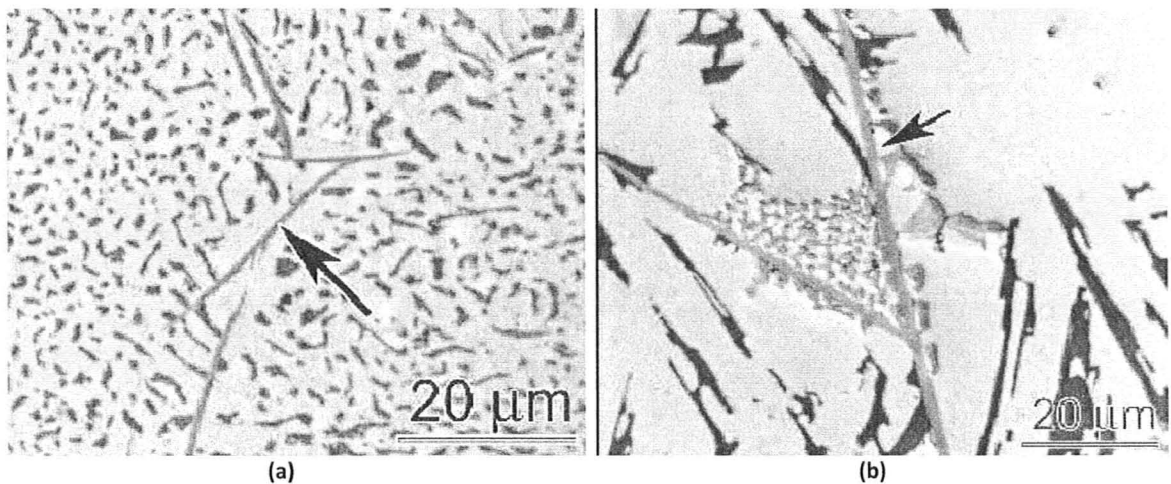


Figure 1-15 Optical microscope images of a) $\delta\text{-Al}_3\text{FeSi}_2$ and b) $\beta\text{-Al}_9\text{Fe}_2\text{Si}_2$ intermetallics [Kral 2006]

Three different Chemical composition diagrams for common intermetallics obtained from EDAX investigation are shown in Figure 1-16.

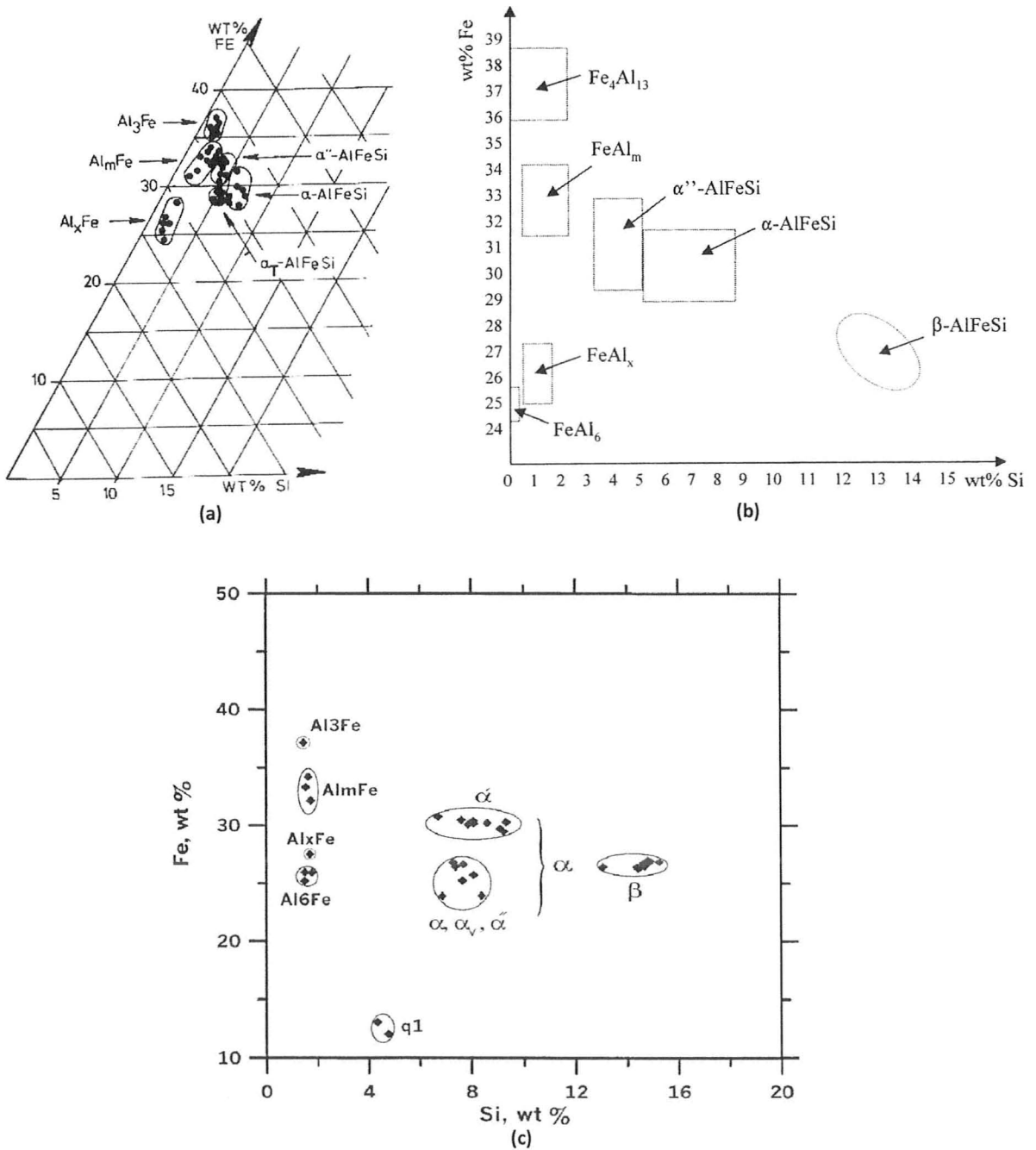


Figure 1-16 Three different chemical composition diagrams reported by different researchers (a) By Skejerpe [1987] (c) By Langsrud [1990] (d) By khalifa *et.al* [2003]

1.3 Theories explaining the formation of Fe-rich and Si-rich intermetallics in as-cast alloys

As mentioned in section 1.2, more than two dozen stable and metastable binary and ternary intermetallic phases have been identified so far in hypoeutectic aluminum alloys. Despite all efforts in this area, mechanism of the formation of these intermetallics is still a puzzle i.e. there is no comprehensive model elucidating a sequential or simultaneous formation of these intermetallic phases under different solidification conditions.

In general, approaches can be divided into different branches in terms of non-equilibrium features of solidification as governing factors. It seems that among all parameters, cooling rate is the main determining factors attracting researchers' attention. It is worthwhile to notice that the cooling rate can be linked to the supercooling and therefore to the competitive nucleation.

Also, there are other groups of researchers [Todd 1996, Hughes 1977, Wang 1998, Stone 1997] whose focuses are on the solidification front velocity as the principal parameter. The solidification front velocity can be linked to competitive growth between phases.

A schematic representation of the role of competitive nucleation and competitive growth in phase selection is shown in Figure 1-17 [Perepezko 1995]. It can be seen that depending on solidification conditions, above a certain level of

undercooling or growth velocity, metastable β forms as the dominant phase in the microstructure.

For example, at high solidification front velocities, growth of the equilibrium phase with faceted interface may be limited as a result of difficulty in atomic attachment [Perepezko 1995] i.e. the required amount of undercooling for growth increases by increasing the growth rate (Figure 1-17 - c).

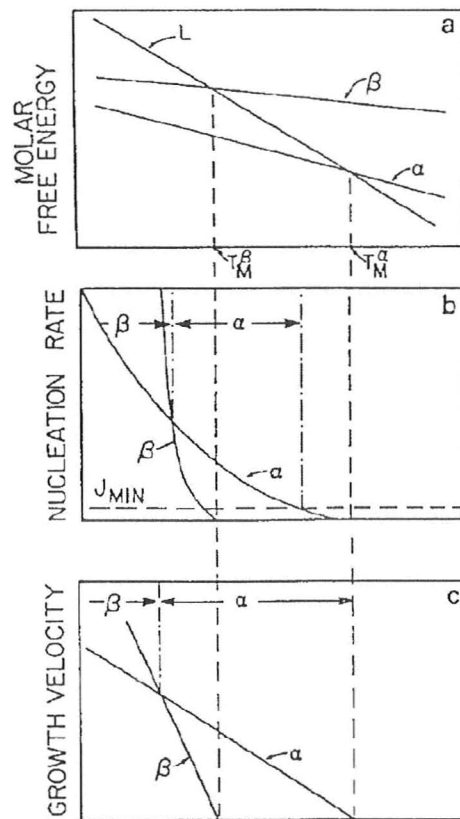


Figure 1-17 Schematic representation of competitive nucleation and competitive growth between α and β

[Perepezko 1995]

The influence of growth rate on required interface undercooling is schematically shown in Figure 1-18. At high solidification front velocities, considering the morphology

and growth kinetic of phases, intermetallics with faceted crystal structure (e.g. $\text{Al}_{13}\text{Fe}_4$ or $\beta\text{-AlFeSi}$) can be replaced by metastable intermetallics with non-faceted structures (e.g. Al_6Fe or $\alpha\text{-AlFeSi}$) [Allen 1998].

Todd and Jones [1996] used the same kinetics reason for explaining observed transitions in the morphology of $\text{Al}_{13}\text{Fe}_4$ from faceted lath-like to non-faceted rod-like particles by increasing the solidification front velocity.

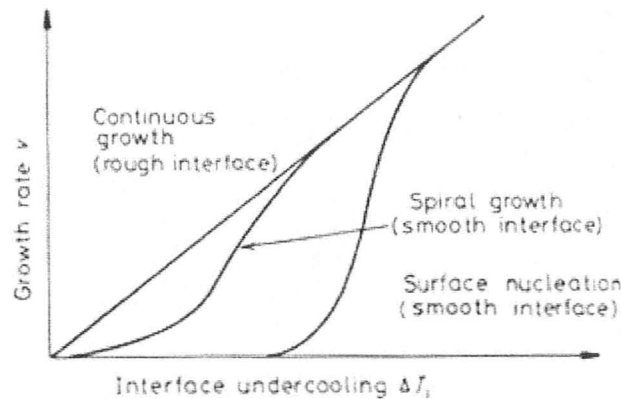


Figure 1-18 The influence of growth rate on required interface undercooling for rough and smooth surfaces [Porter 2001]

Beside these arguments about the role of the growth velocity on the phase formation in aluminum alloys, it is worth mentioning that in most of the literature related to DC cast products, the formation of different intermetallics across the width of DC cast billets (i.e. “fir-tree” or “Altenpohl” zones^{*}) is attributed to the variation of the cooling rate (i.e. competitive nucleation) across the ingots (Figure 1-19).

^{*} Different responses to the etchant caused by the variation of intermetallic type across the DC ingots results in the formation of different zones over the cross section of these ingots. These zones are called “fir-tree” or “Altenpohl” zones.

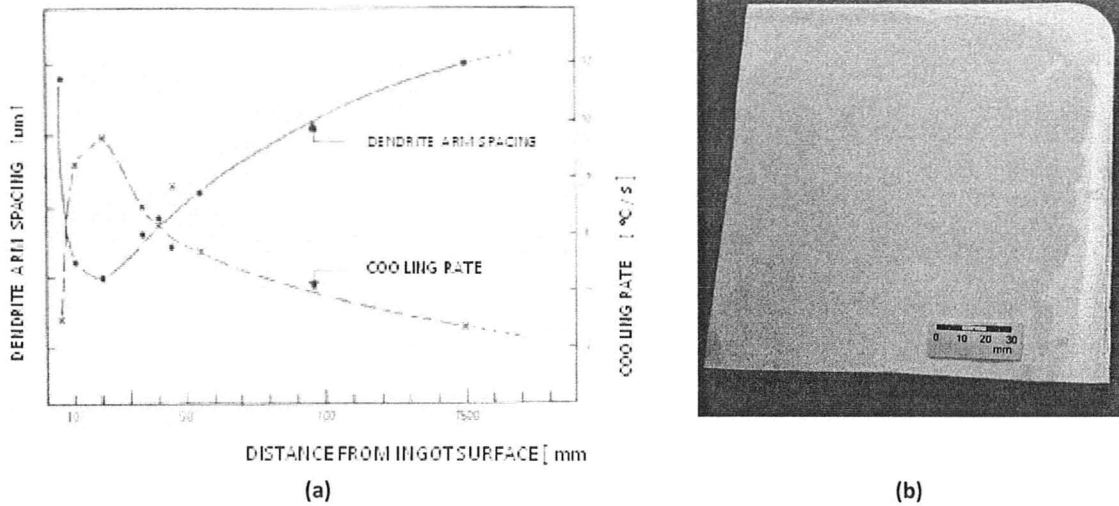


Figure 1-19 (a) Variation of cooling rate across the width of DC cast billets [Westengen 1982] (b) Fir-tree zone in DC cast AA1200 sheet ingot, NaOH is used as the etchant [Pettersen 2007]

In general, the nucleation rate I can be described by the following equations

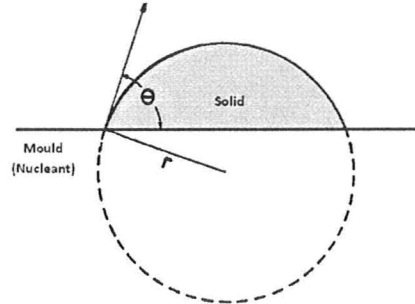
[Feuerbacher 1989, Porter 2001]:

$$I = f_0 C_0 \exp \left[\frac{-\Delta G^*}{k_B T} f(\theta) \right] \quad \left\{ \begin{array}{l} k_B = \text{Boltzmann constant} \\ \Delta G^* = \text{Activation energy} \\ C_0 = \text{Number of atoms per unit volume} \\ \theta = \text{Wetting angle} \end{array} \right.$$

f_0 is a complex function that depends on the vibration frequency of the atoms, the activation energy for diffusion in the liquid, and the surface area of the critical nuclei. It is worth noticing that f_0 strongly depends on temperature and diminishes with decreasing temperature e.g. at high degrees of supercooling, when temperature is around glass-transition temperature, T_g , this function, and as a result the nucleation rate, will be very small and amorphous alloy can be produced.

$f(\theta)$ is a function describing the reduction of activation energy for heterogeneous nucleation on the surface of a nucleant:

$$f(\theta) = (2 + \cos \theta)(1 - \cos \theta)^2 / 4$$



In competition between phases for nucleation, it seems that activation energy (ΔG^*), which is composed of interface (ΔG_i) and volume (ΔG_v) terms, has a more pronounced influence than pre-exponential term on choosing the dominant phase [Purdy 2004].

(1)	$\Delta G^* = (\Delta G_v + \Delta G_i)$	{	$n =$ Number of moles
(2)	$\Delta G^* = n\Delta G^{Liquid \rightarrow \alpha} + \sigma A$		$\Delta G^{Liquid \rightarrow \alpha} =$ Chemical driving force for nucleation
			$A =$ Surface area of the nucleus
			$\sigma =$ Surface energy

In aluminum alloys, despite all efforts done for prediction of intermetallics at different cooling rates, still lack (or absence) of information about thermodynamics and kinetics parameters governing the nucleation process of metastable intermetallics, is felt quite noticeably. In other words, most of authors focus only on the experimental observations at different compositions and solidification conditions and consequently,

the theoretical aspects, which can be used to explain these observations, are remarkably rare in comparison to the experimental results.

In this regard, it seems that the nucleation based arguments are mainly limited to the substitution of $\text{Al}_{13}\text{Fe}_4$ with Al_6Fe .

Also, it is worth mentioning that reviewing the literature shows that the orientation relationship between FCC matrix and $\text{Al}_{13}\text{Fe}_4$ is an open debate among researchers. For example, in some cases researchers report an orientation relationship between Al and $\text{Al}_{13}\text{Fe}_4$ which can facilitate its nucleation process at low undercoolings. On the other hand, in the absence of impurities high levels of undercooling ($\sim 10\text{-}15\text{ K}$) have been reported for the formation of $\text{Al}_{13}\text{Fe}_4$. This amount of undercooling is related to the low potency of aluminum matrix for nucleation of $\text{Al}_{13}\text{Fe}_4$ [Allen 1998].

Allen *et.al* [1998] summarized the reported cooling rates and growth velocity ranges at which phase transitions for common intermetallics occur. These values are presented in Table 1-6 and Table 1-7.

One of the difficulties arises in line with these types of investigations is that there is no unique cooling rate or growth rate for these transformations [Allen1998] i.e. there is a range of cooling rates in which a particular phase transition may occur. Another difficulty is the inconsistency of observations i.e. different authors report different intermetallic phases for the same alloy solidified at the same conditions

(cooling rate and growth front velocity). As a result, a clear picture of the situation has not been emerged yet [Todd 1996].

Table 1-6 Summary of the different reported solidification front velocities at which phase transition occur, [Allen1998]

Transition	Alloy	Solidification velocity range of transition
$\text{Al}_{13}\text{Fe}_4 \rightarrow \text{Al}_6\text{Fe}$	Hypoeutectic Al-Fe, Hypereutectic Al-Fe	$\sim 0.1\text{-}0.2 \text{ mm s}^{-1}$
$\text{Al}_{13}\text{Fe}_4 \rightarrow \text{Al}_x\text{Fe}$	Hypoeutectic Al-Fe,	$\sim 0.15\text{-}0.2 \text{ mm s}^{-1}$
$\text{Al}_{13}\text{Fe}_4 \rightarrow \text{Al}_m\text{Fe}$	Hypoeutectic Al-Fe +0.1 wt% Si + Al-Ti-B	$> 1.33 \text{ mm s}^{-1}$
$\text{Al}_{13}\text{Fe}_4 \rightarrow \alpha\text{-AlFeSi}$	Hypoeutectic Al-Fe +0.2 wt% Si	$\sim 1\text{-}2 \text{ mm s}^{-1}$

Table 1-7 Summary of the different reported cooling rate ranges for the formation of common intermetallics in hypoeutectic Al-Fe alloys, Allen *et al.* [Allen1998]

Phase	Cooling rate range, K s^{-1}
$\text{Al}_{13}\text{Fe}_4$	0.1-3
Al_xFe	0.4-5
Al_9Fe_2	1-6
Al_6Fe	2-11
Al_mFe	> 11

Despite the difficulties mentioned above, there is an overall agreement among researchers that the binary Al-Fe intermetallics form at low cooling rates and low concentrations of Si [Khalifa2003]. By increasing the cooling rate or the growth front velocity, dominant intermetallics in the system shift from binary $\text{Al}_{13}\text{Fe}_4$ and $\text{Al}_6\text{Fe}/\text{Al}_x\text{Fe}$ to Al_mFe and finally to the ternary AlFeSi intermetallics [Skejerpe 1987].

However, one should be aware that this trend is not always true. In many experiments when Si is present in the composition of alloy, existence of α -AlFeSi particles is reported at very low cooling rates. For example, during solidification in the centre of DC cast sheet ingots, with cooling rates less than 1 K/s, low concentrations of α -AlFeSi is reported [Pettersen 2007].

1.3.1 Scheil- Gulliver Formalism and metastable intermetallics

One common way for determining solidification path under non-equilibrium conditions is using Scheil-Gilliver formalism, which calculates solid and liquid compositions during solidification. In original Scheil-Gulliver method no diffusion in the solidified phase and uniform composition throughout the liquid are assumed for the system i.e. back diffusion of the solute atoms into the solid is neglected. Details of the Scheil-Gulliver formalism are presented in appendix 4.

By advancing the solidification front, rejection of solute atoms into the liquid phase (when $K < 1$) continually changes the liquid composition. This will introduce changes in the composition of the solidified phase at solid/liquid interface. Continuation of this process introduces a concentration gradient in the solid, which is in fact made from different layers of solid phases with different compositions. This effect seems to be more pronounced at the final stages of solidification in which solute concentration in the interdendritic regions increases rapidly [Langsrud 1990]. Considering this gradient, some researchers believe that back-diffusion concept should be taken into account and

as a result, in modified version of Scheil-Gulliver, some flux back into the solid is considered by introducing back diffusion parameters.

Using these models for aluminum alloys, it is seen that neither the original Scheil-Gulliver model nor the modified version of that are able to predict the observed solidification paths in aluminum alloys [Langsrud 1990, Khalifa 2003].

In line with investigations for finding the reason/reasons of a deviation of Scheil-Gulliver model from actual solidification paths, Langsrud [1990] proposed changes in the equilibrium Al-Fe-Si phase diagrams. He suggested that by increasing the cooling rate, phase boundaries should be shifted to higher Fe and lower Si concentrations to produce satisfactory results. He recommended new Al-Fe-Si metastable phase diagrams by which he was able to predict the main features of his experimental observations for different cooling rates. The experimental results and the suggested phase diagrams are shown in Table 1-8 and Figure 1-20 respectively.

For example for an alloy with composition A (shown in Figure 1-20) at high cooling rates (10 K/s), calculated solidification path by Scheil-Gulliver model crosses the α, α'^* region. It means that α and α' phases are the first intermetallic phases to precipitate and consequently, are the dominant phases in the microstructure. However if solidification time is enough, according to these metastable phase diagrams, in later stages α and α' may transform to β phase via a peritectic reaction.

* Metastable forms of α with lower silicon content (4-6 wt %)

Table 1-8 Intermetallic phases in DC-cast commercial purity AlFeSi alloys, Langsrud [1990]

Alloy Composition (wt%)	Cooling rate °Cs ⁻¹	wt% Al ₆ Fe/Al _x Fe	wt% Al _m Fe	wt% Al ₃ Fe	wt% α-types	wt% β	wt% Si
0.27 Fe 0.09 Si	10	0.58	0.18	0.10	Trace	-	-
	3	-	0.28	0.40	-	-	-
	1	Not measured					
0.25 Fe 0.13 Si	10	-	0.25	-	0.45	-	-
	3	0.12	0.19	0.33	0.02	-	-
	1	Not measured					
0.24 Fe 0.24 Si	10	-	-	-	0.69	-	Trace
	3	-	-	0.22	0.43	-	Trace
	1	Not measured					
0.24 Fe 0.48 Si	10	-	-	-	-	0.77	0.01
	3	-	-	-	-	0.77	0.01
	1	Not measured					
0.54 Fe 0.15 Si	7	1.38	-	0.39	-	-	-
	2	0.20	-	1.21	-	-	-
	~1	0.37	-	1.11	-	-	-
0.74 Fe 0.76 Si	7	-	-	-	0.37	2.13	0.05
	2	-	-	-	1.86	0.44	0.05
	~1	-	-	0.72	0.73	0.73	0.05

Table 1-9 Intermetallics formed in high purity Al-Fe-Si system, [Khalifa 2003]

Cooling rate	Alloy (wt%)	Si = 0.35 Fe= 0.23	Si = 0.49 Fe= 0.23	Si = 0.62 Fe= 0.55	Si = 0.90 Fe= 0.56	Si = 0.62 Fe= 1.03	Si = 6.45 Fe= 0.52
	0.16 – 0.21 °Cs ⁻¹	Al _m Fe, Al ₆ Fe, Al _x Fe	α	α, Si-rich particles	β, α*	Al ₃ Fe Al _m Fe, Al ₆ Fe, α	β
10 – 15 °Cs ⁻¹	δ, β	δ, β, q ₁	α, δ	δ	α, q ₁	δ	

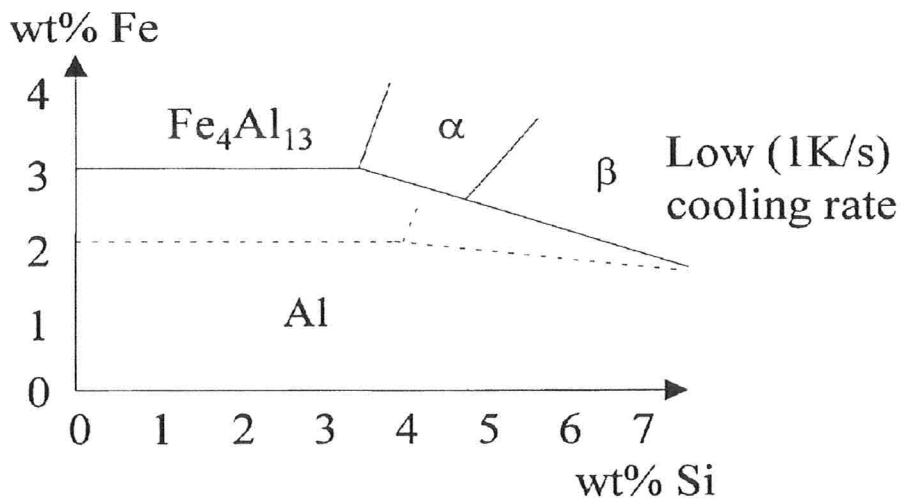
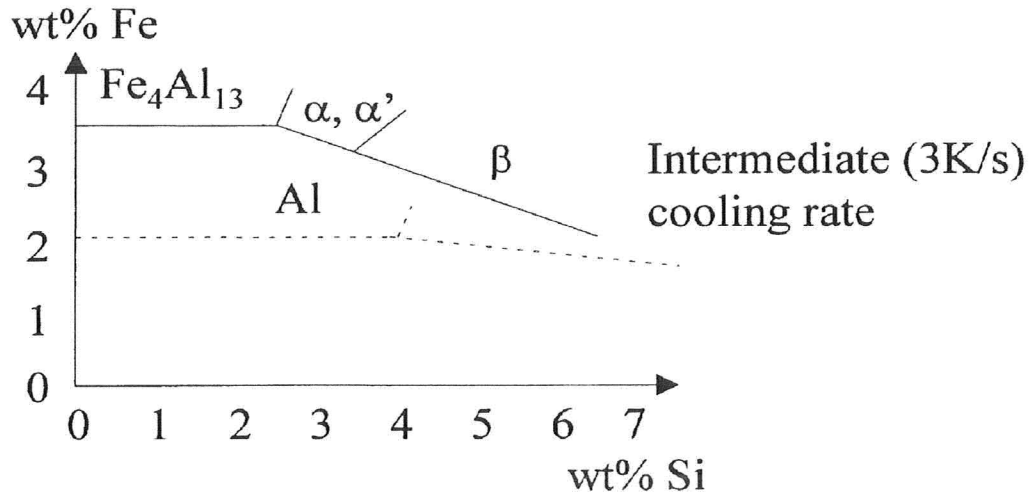
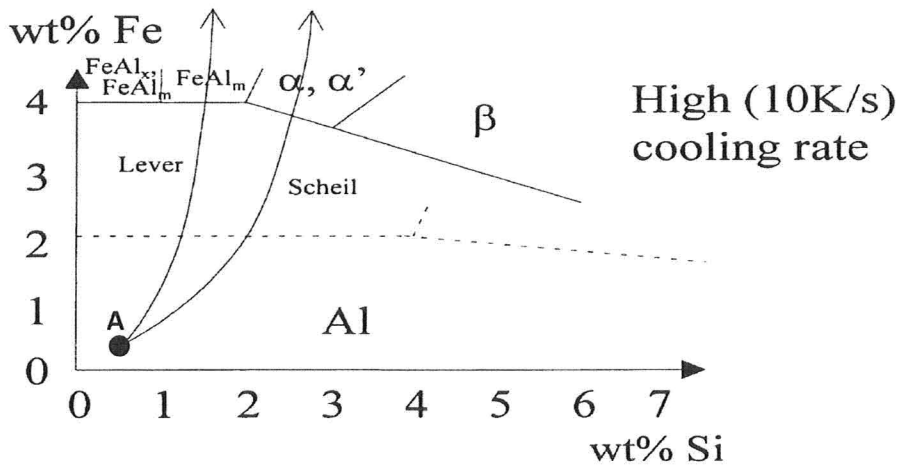


Figure 1-20 Suggested metastable AlFeSi liquidus surfaces by Langsrud [1990]

In another attempt, Khalifa *et.al* stated that modified versions of Scheil-Gulliver, “...give less weight to the effect of solid-state back-diffusion than they should” [Khalifa2003] and that’s why the deviations from actual solidification paths were seen. Also, interaction between iron and silicon (e.g. effect of silicon on the diffusion rate of Fe atoms in FCC matrix) was mentioned as another possibility for deviation of experimental results from Scheil-Gulliver solidification model.

Intermetallics observed by Khalifa *et.al* [2003] for different compositions and cooling rates are listed in Table 1-9.

1.4 Driving forces for onset of precipitation

Usually, in analysis of nucleation controlled microstructures, $\Delta G^{\text{Liquid} \rightarrow \alpha}$ in equation (2) in section 1.3 is considered to be the driving force for attainment of full equilibrium (Figure 1-21-a). This value for stable phases is always smaller than that for metastable ones. As a result, in most of the publications, the formation of metastable phases at high cooling rates is related to either the surface energy of phases or potency of the active catalytic sites in the melt [Feuerbacher 1989, Perepezko 1995, Purdy 2004]. One should realize that in majority of cases, due to lack of available information about nucleation potency and surface energy of phases, this conclusion is limited to just a general statement.

On the other hand, instead of this common approach and focusing on the interface energy contribution (ΔG_i), one can consider “driving forces for onset of

precipitation" (nucleation potential of a phase). This concept was first originated by Miroshnichenko, and later elaborated by Cahn and Hillert [Hillert 1999]. In 2004 Purdy *et.al* [Purdy 2004] developed this theory to a more comprehensive level for explaining nucleation step and microstructural development in different alloying systems (appendix 5).

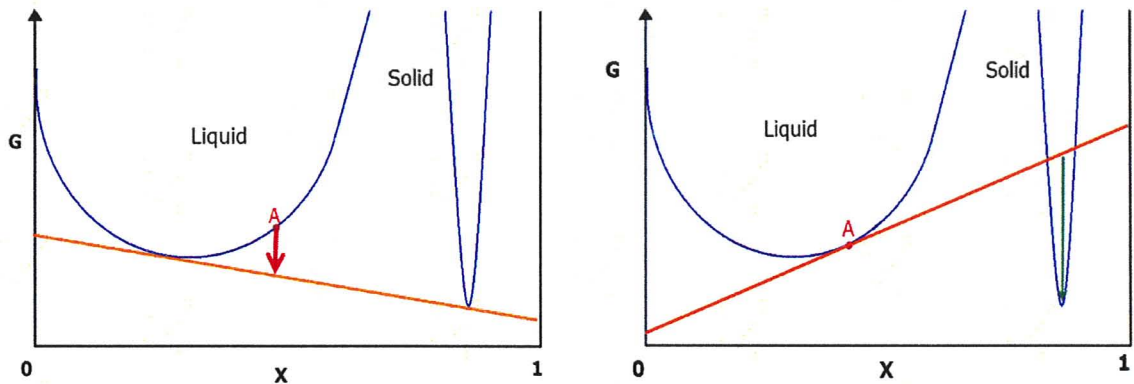


Figure 1-21 Driving forces for attainment of full equilibrium (a) and for onset of precipitation (b) [Purdy 2004]

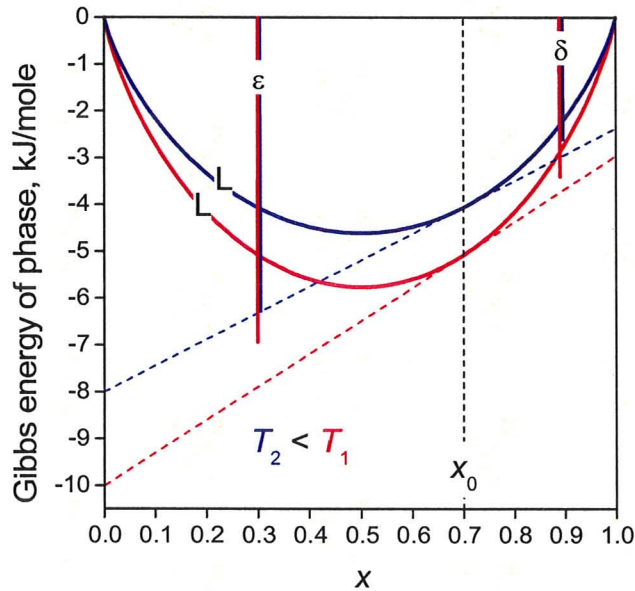


Figure 1-22 Schematic of effect of supercooling on the Gibbs energy and driving forces of nucleation

These driving forces for onset of nucleation and attainment of full equilibrium are schematically presented in Figure 1-21. As mentioned before in section 1.3, cooling rate can be related to the supercooling and consequently to the competitive nucleation between phases. In other word, at high cooling rates due to the created supercoolings in the system, some of the phases, which energetically are not promoted in equilibrium conditions, may attain a positive driving force for start of nucleation. This condition is schematically presented in Figure 1-22. It can be seen that for an alloy with composition X_0 at $T=T_1$, both ϵ and δ have a negative driving force to nucleate from liquid; while, by decreasing the temperature ($T=T_2$) these driving forces may become zero (such as ϵ in this case) or positive i.e. thermodynamically they attain the minimum conditions for nucleation.

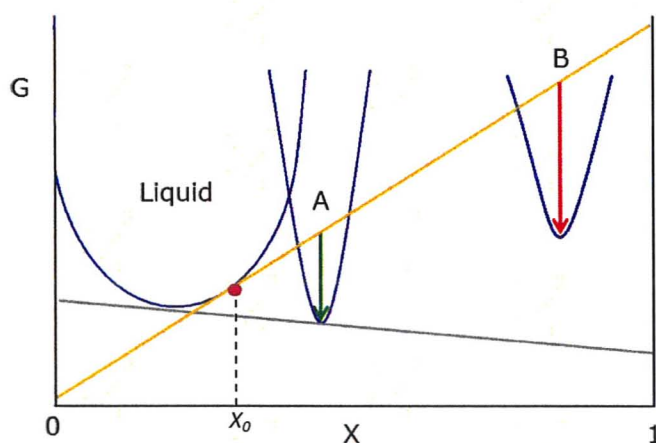


Figure 1-23 Driving forces for onset of precipitation stable and metastable phases [Purdy 2004]

As can be seen from Figure 1-23 in some cases at high supercoolings the driving force for onset of precipitation of metastable phases (B) can get bigger than that of

stable ones (A) i.e. metastable phases become thermodynamically more favorable to nucleate.

Hillert [1999] showed that for low supercoolings the driving force for the onset of precipitation is directly proportional to the difference in composition between the supersaturated (e.g. liquid in solidification process) and forming phases. Based on this, he concluded that, "...the nucleation new stable phase can be very difficult because its composition is very close to the parent phase, but a new metastable phase with a very different composition can nucleate and it may latter assist in nucleating the stable phase."

1.5 Effect of impurities in nucleation of metastable intermetallics

As already mentioned, one of the difficulties in characterizing the solidification paths is inconsistency in the results reported by different researchers. This discrepancies result in a blurry picture of what is actually happening in the melt during solidification.

Usually, in the literature the presence of impurities in the melt is introduced as the main parameter for such inconsistency in the experimental results. For example, Todd and Jones [1996] mentioned that, "...It has also been suggested that discrepancies often found when comparing the result of previous work in both the binary Al-Fe and ternary Al-Fe-Si alloys, are attributable even to trace levels of impurity in the alloys investigated".

Allen *et.al.* [1998] used differential scanning calorimetry and noticed differences in the peaks obtained for commercial purity alloys and peaks obtained for high purity alloys. They concluded that small amounts of V, Zr and P (500 ppm) can promote nucleation of metastable intermetallics like Al_mFe .

It is worth mentioning that, in general there are a few systematic investigations related to the nucleation mechanism and effect of different impurities on binary and ternary intermetallics during non-equilibrium solidification.

Khalifa *et.al* [2005] investigated effects caused by the presence of $\alpha-Al_2O_3$, $\gamma-Al_2O_3$, MgO, CaO, Al_4C_3 , SiC, TiC and TiB_2 in aluminum alloys. Regardless of the type of the impurity in the melt, they reported an increase in the number of all Fe-rich and Si-rich intermetallics under the same solidification conditions. They observed that by increasing the cooling rate and solute concentration, potency of the nucleating surfaces (impurities) increased, but, after a certain level of solute concentration, due to the poisoning effect of solute on the available nucleating sites, the increasing trend will be reversed.

It seems that neither chemical characteristic of impurities nor orientation relationship at the surface of impurities have a determining effect on the type of observed phases in interdendritic regions [Khalifa 2005]. In line with this, Khalifa *et.al* stated that "... the selective formation of certain phases during solidification (usually referred to as phase selection) on the basis of nucleation does not seem to be largely

affected by the type of nucleant present in the liquid phase. Nucleation control of the second-phase particles such as Fe-intermetallics ... is most likely influenced by chemical factors (*i.e.*, alloy composition and solute segregation characteristics), nucleating temperatures, and cooling conditions rather than type of the nucleating surface” [Khalifa 2005].

2 Chapter 2

2.1 Research objective and experimental approach

As mentioned in Chapter 1, strip-cast alloys are not currently used in vehicle manufacturing. The principal reason for this is that they demonstrate an inferior formability in comparison with conventional DC cast alloys which are subject to much more extensive thermo-mechanical processing (TMP) needed for making thin (2-4 mm) sheets.

An underlying reason for sheet failure is the formation of brittle intermetallic phases, which either crack during deformation (e.g. stamping) or act as sites from which voids may nucleate.

Despite all efforts during the last 30-40 years, particularities of formation the Fe-rich and Si-rich intermetallics in aluminum alloys is still an unraveled mystery.

Developing a solidification model (or models) explaining why a particular microstructural portrait is observed in the as-solidified alloy is of increasing importance as the automotive industry moves from more costly (traditional) sheet manufacturing methods, including conventional Direct Chill casting, homogenization and hot/cold rolling, to near-net shape methods such as strip casting.

Understanding the nature and a sequence of the formation of these intermetallics phases precipitating from a supersaturated melt is in the centre of this

research. In fact, this endeavor was launched to answer the following fundamental question: “What governs the formation of intermetallic phases from a rapidly solidifying aluminum alloys?”

In line with the mentioned objective, different approaches can be employed. Prior to starting this investigation, it was believed that the concept of the driving forces for the beginning of precipitation originated by Miroshnichenko [1966] , and further developed by Cahn [1969] and Hillert [1970] could be used to explain experimental findings. Was that belief justified? Although a definite answer to this question has not been found, there are strong indications that the concept is likely operative.

This concept, initially developed for binary systems and small undercoolings, was generalized by Purdy *et.al.* [2004] to multicomponent cases with arbitrarily undercoolings (some details are presented in Appendix 5). Unfortunately, due to the lack of information on surface energies, at the present stage, this approach still does not take into account the surface energies of intermetallics formed from a supersaturated liquid.

To evaluate applicability of this concept to the formation of Fe-rich and Si-rich intermetallics in aluminum alloys, an array of experimental information related to microstructures of as-cast alloys having different compositions is obtained in this research. Then, the collected experimental results are interpreted using the concept of the driving forces for the beginning of precipitation.

Also, casting temperature was guessed to be an important variable in the course of solidification of aluminum alloys. Information disseminated in publications and private communications provides strong evolving evidence of significance of the melt superheat on the type and morphology of iron-based intermetallic phases forming during casting. It can be speculated that at temperatures slightly exceeding liquidus, the liquid phase is prone to cluster formation due to different affinities among alloying components. These domains having different compositions (and thus behaving differently during casting) can hardly be eliminated by holding the melt at near-liquidus temperatures, but overheating will diminish the tendency to clusterization.

In the present research, by changing the casting temperature (T_c), it was tried to compare microstructural features of samples fabricated with similar cooling rates but originated from liquid phases with drastically different initial temperatures (e.g. 400 °C) and thus separate the effect of superheating.

2.2 Experiments

2.2.1 Making the alloys

It was decided to validate the method by launching a series of solidification experiments on the alloys with carefully controlled compositions. In fact, a systematic investigation (i.e. observation and interpretation) of intermetallic “phase portraits” for dilute Al alloys resulting from different casting conditions (i.e. different cooling rates) is in the center of our approach.

Four different compositions were carefully chosen to examine the effect of Fe and Si additions on the formation of intermetallics at different cooling rates. Compositions of these alloys are presented in Table 2-1.

Table 2-1 Selected aluminum alloy compositions for the experiments

Experiment Composition	Alloy #1	Alloy #2	Alloy #3	Alloy #4
	Low Si Intermediate Fe	Intermediate Si Intermediate Fe	High Si Intermediate Fe	Intermediate Si High Fe
Si wt%	0.05 ± 0.01	0.15 ± 0.01	0.45 ± 0.01	0.20 ± 0.01
Fe wt%	0.30 ± 0.01	0.30 ± 0.01	0.30 ± 0.01	0.50 ± 0.01

Alloys were made using commercial purity aluminum shots (Table 2-2), high purity silicon (99.9999 %) and high purity iron (99.98).

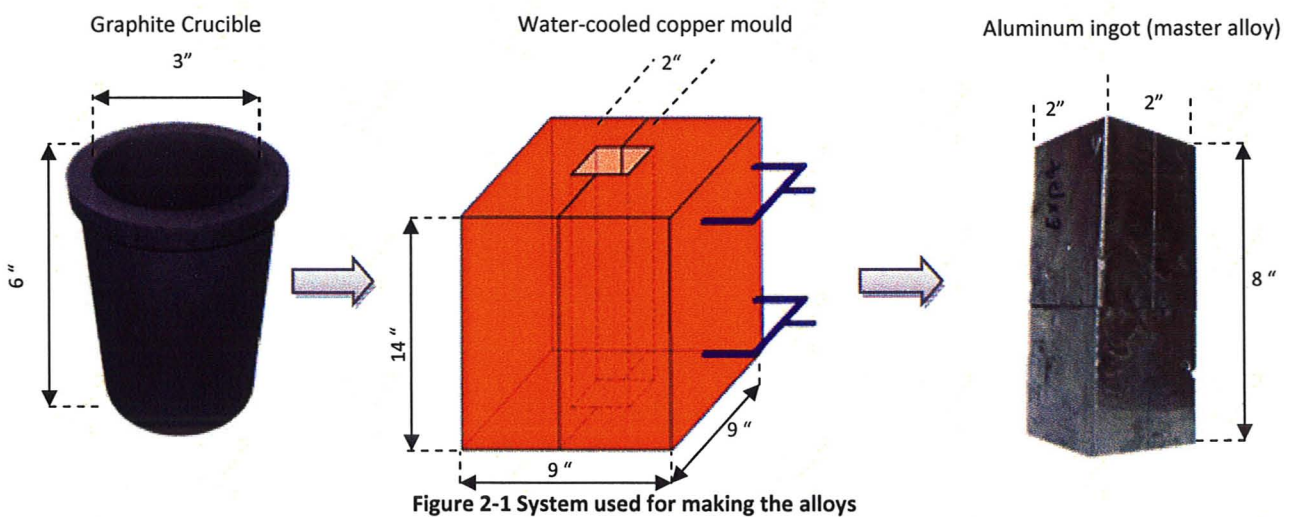
Table 2-2 Composition of the aluminum shots used for making master alloys (provided by Alfa Aesar company)

	Aluminum	Silicon	Iron	Zinc	Vanadium	Gallium
wt %	99.90	0.028	0.055	0.012	0.004	0.005

For the sake of simplicity, from now on the following notation system will be used for different alloys:

- Alloy #1 with 0.3 wt% Fe and 0.05 wt% Si → "A1-Fe.3-Si.05"
- Alloy #2 with 0.3 wt% Fe and 0.15 wt% Si → "A2-Fe.3-Si.15"
- Alloy #3 with 0.3 wt% Fe and 0.45 wt% Si → "A3-Fe.3-Si.45"
- Alloy #4 with 0.5 wt% Fe and 0.20 wt% Si → "A4-Fe.5-Si.2"

To make the master ingot, which is used as the source of material for further investigations, mixtures of alloying elements were melted in a graphite crucible using an induction heating furnace. After melting, the mixtures were stirred for about 45-55 minutes and then poured in a water-cooled copper mould to be solidified. It is worth mentioning that before initiating the casting step, an oxide layer formed on top of the melt was completely removed to prevent it from entering into the ingot. The moulds and ingot dimensions and a sequence of actions are sketched Figure 2-1.



Compositions of solidified ingots were determined by using Induction Coupling Plasma (ICP). Four samples were taken from four different sections of each ingot (two samples from top of the ingots and two samples from bottom of them). After digestion in a 1:1:2 mixture of HCl : HNO₃ : H₂O, the mixtures were put in a microwave for 30 minutes. One should pay attention that Fe is completely digested in the first step, but, if microwave step is not used, due to incomplete digestion of silicon an accurate result will not be obtained.

Obtained results for different sections of the ingots and the average composition of them have been presented in appendix #1. After that, the produced ingots were cut into small pieces to be cast with different cooling rates.

2.2.2 Casting (different cooling rates)

According to the literature, cooling rates in conventional DC cast ingots can vary from 1 °C/s to 10-15 °C/s. In the case of strip cast sheets, this amount can reach approximately to 500 °C/s [Khalifa 2003, Griger 1996]

In our research in order to cover a broad range of cooling rates, six different solidification rates (cooling rates) were chosen including:

1. Solidification in a hot graphite crucible. For this experiment, at the first, small pieces of alloy were melted in a graphite crucible. Then the molten alloy was slowly cooled down by turning the induction heating system off. According to the literature [Khalifa 2003], it is estimated that low cooling rates less than 1 Cs^{-1} are achieved in these samples.
2. Solidification in a copper mould in which intermediate cooling rate such as $10\text{-}20 \text{ Cs}^{-1}$ are expected to be achieved.
3. Solidification on the surface of a water-cooled copper mould in the form a thin plate with approximately one centimeter thickness. In this sample a range of cooling rates which is expected to reach 500 Cs^{-1} in contact with water-cooled

copper mould is generated. A schematic of casting process is presented in Figure

2-2.

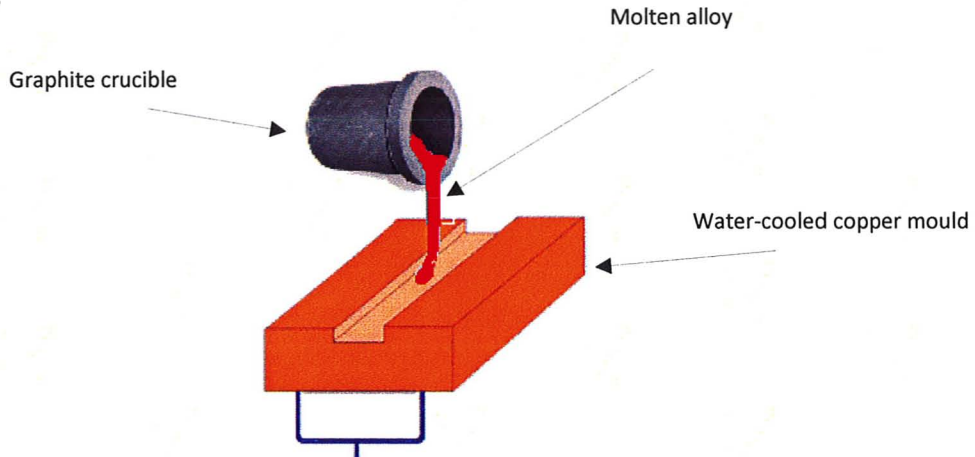


Figure 2-2 Schematic of casting on the surface of the water-cooled copper mould

4. Very high cooling rates (10^3 to 10^5 Cs⁻¹) were achieved by using a melt spinner donated by Novelis.

In this method, which is shown in Figure 2-3, a stream of molten metal is poured on the surface of a rotating copper drum and solidifies in the form of thin ribbons. Depending on the angular velocity of the drum various rates of heat extraction can be achieved.

www.inmat.pw.edu.pl/.../wazniejsze_techniki.htm

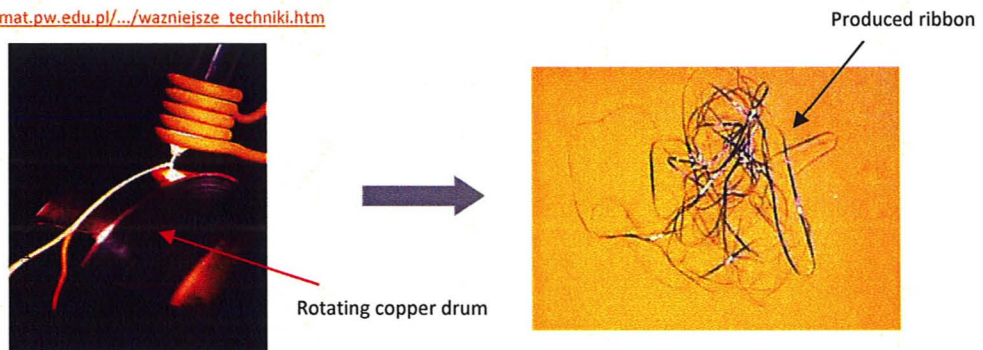


Figure 2-3 Ribbon formation by melt spinner

Different parts of the donated melt spinner are shown in Figure 2-4.

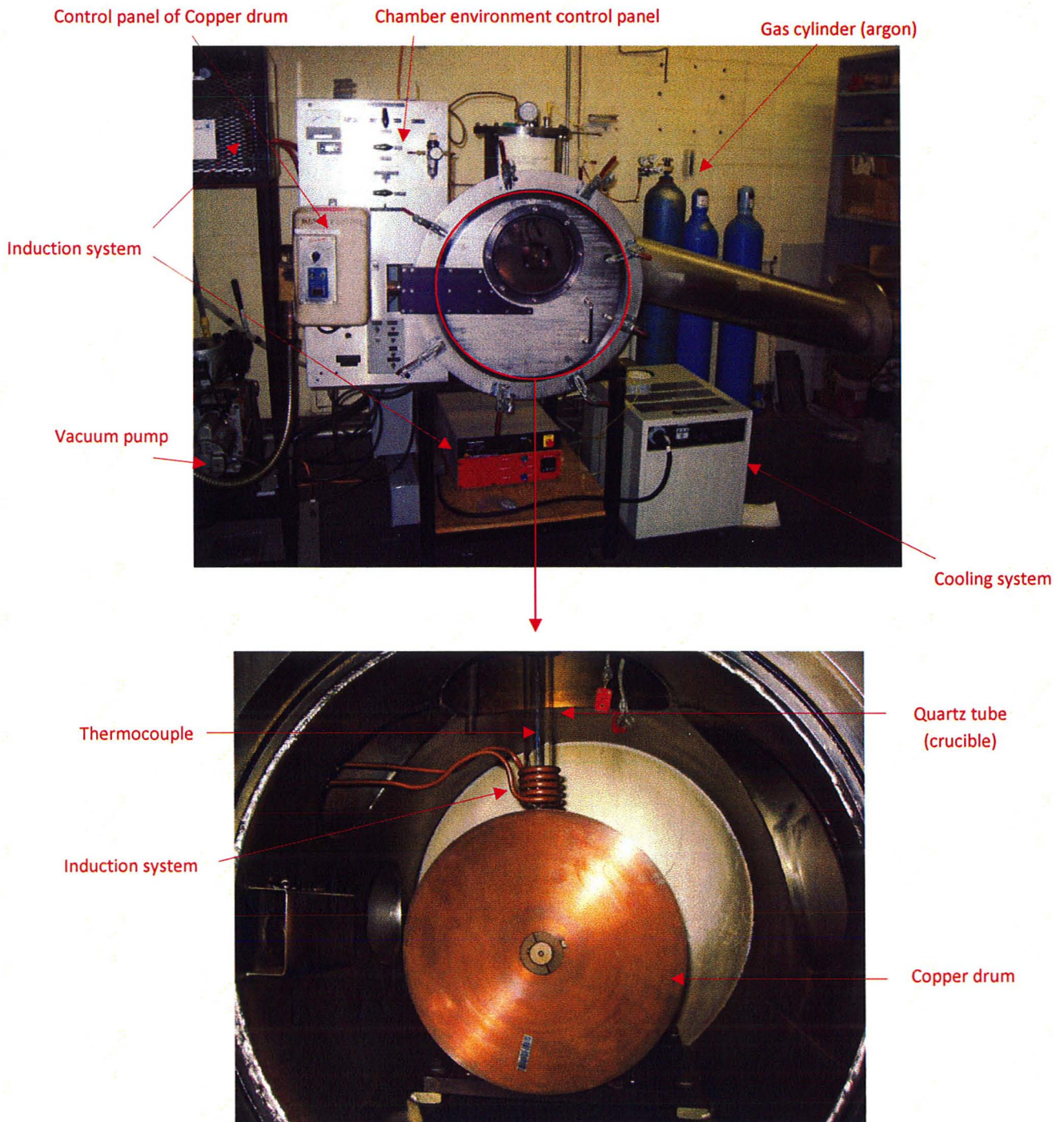


Figure 2-4 Different parts of the melt spinner donated by Novelis to McMaster university

It is worth mentioning that, after receiving the melt spinner from Novelis, due to some difficulties such as:

- Missing manuals
- Non-working cooling system
- Non-conformity with Canadian regulations and necessity of some alterations for approval of Ontario electrical safety agency.
- The operative voltage which was 460 V and required a transformer to convert the available voltage (110 V) to 460 V.
- Damaged temperature recorders
- Inoperative manometers

a considerable time was spent to make this equipment operational.

In order to make samples solidified at very high cooling rates, for each alloy three different velocities including 400 rpm, 930 rpm and 1520 rpm were chosen. In other words, considering the diameter of the copper drum (12 inches), the castings were performed at 0.65 ms^{-1} , 1.5 ms^{-1} and 2.48 ms^{-1} which at the end resulted in the formation of ribbons with average thicknesses of $300 \text{ }\mu\text{m}$, $150 \text{ }\mu\text{m}$ and $70 \text{ }\mu\text{m}$ respectively. Before starting the experiments, melt spinner's chamber was first

vacuumed and then filled with argon gas to reduce the oxidation conditions. Casting temperature for all ribbons was around 770 °C, i.e. approximately 100 °C above liquidus.

Based on literature, in the melt spinner cooling rate can vary from 10^3 °C/s to 10^6 °C/s and in the some cases it can reach to even 10^7 °C/s which can be used for production of amorphous alloys [Griger1996]. In the present research, considering the solidification conditions (argon atmosphere, quality of the surface of the copper drum and not very high copper drum velocities such as 2000 rpm which is achievable in the donated melt spinner) it is not expected to reach to such high cooling rates as 10^6 °C/s and 10^7 °C/s.

A general overview of solidification steps is schematically shown in Figure 2-5.

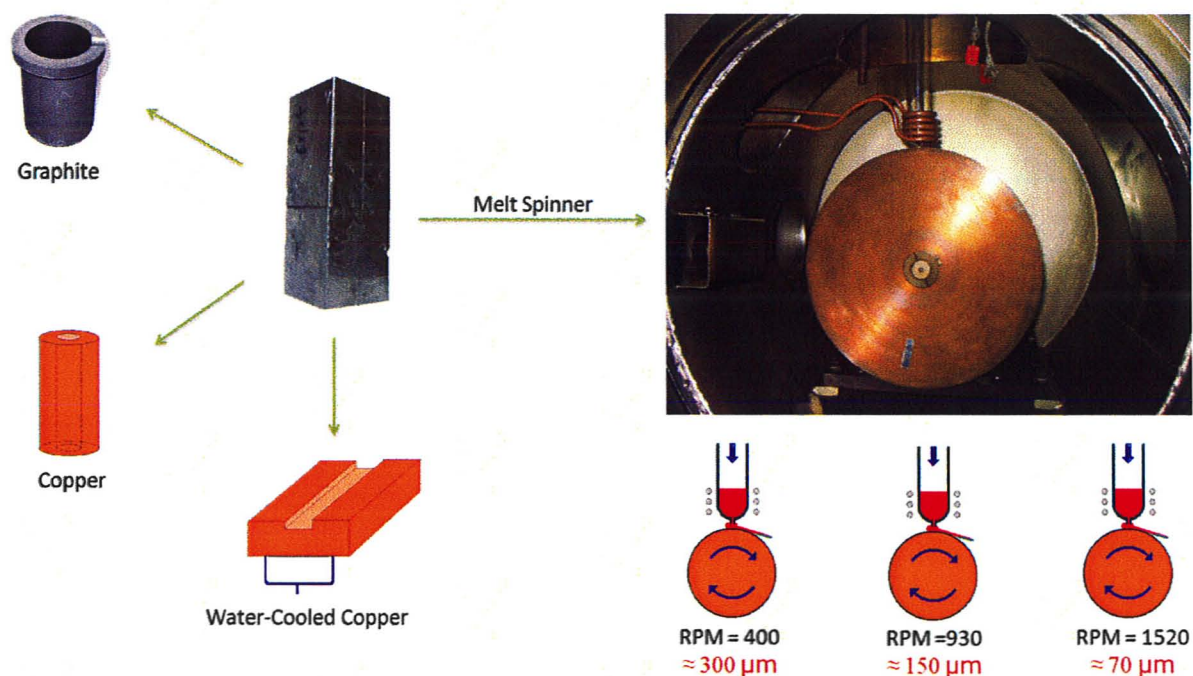


Figure 2-5 Schematic of the casting step (different cooling rates)

To study the effect of the amount of superheating on the intermetallic formation during solidification, one sample of each alloy (i.e. four samples in total) was cast at ≈ 1000 °C by using the melt spinner. The ribbons produced with rpm=930 had an average thickness of 150 μm .

2.2.3 Dissolution step (extraction of intermetallics)

Extraction of intermetallic phases from Al alloys for a subsequent analysis was performed via the dissolution of the FCC matrix in boiling phenol base on a method modified by Pierre Marois at Novelis.

To carry out the dissolutions, approximately three grams of the aluminum alloy were inserted in a flask containing 80-85 ml of boiling phenol. After complete dissolution, the mixture of phenol and extracted particles (aluminum phenolate) was introduced into a three step procedure of rinsing with organic solvents and centrifuging.

In the first step, 100 ml of a solution of 80% benzyl alcohol and 20% toluene was added to the aluminum phenolate and then centrifuged for three hours to separate the extracted particles. In the second step, the collected particle at the bottom of the containers were rinsed with a solution of 60% toluene and 40% benzyl alcohol and then centrifuged for 90 minutes. Finally, in the last step, the same procedure was carried out with an organic solution of 10% benzyl alcohol and 90% toluene and 90 minutes of

2.2.4 Microscopy observations

The morphology (shape) and distribution of intermetallics were studied by using both the optical and scanning electron microscopes (SEM). The obtained results are summarized below.

2.2.4.1 Optical Microscope

Samples preparation for optical microscope was performed using two steps of grinding with 1200 and 4000 series SiC papers followed by a four-stage polishing procedure including polishing with 9 μm , 3 μm and 1 μm diamond powder solution and a final polishing with 0.05 μm silica solution. The microstructure is clearly seen after the last step of polishing with 0.05 μm silica solution. As a result, no etchant was employed for revealing the intermetallic.

a) **A1-Fe.3-Si.05 (alloy #1 with 0.3 wt% Fe and 0.05 wt% Si)**

I. Graphite Crucible (A1.G)

Figure 2-7-(a) and (b), show that most of the intermetallics are distributed in interdendritic regions. A close look at these phases will reveal different morphologies such as Chinese scripts and needle-like. Each needle-like particle can be related to the cross section of a plate or rod-like particle. In general, observation of different morphologies can be attributed to the existence of different types of intermetallics in this sample.

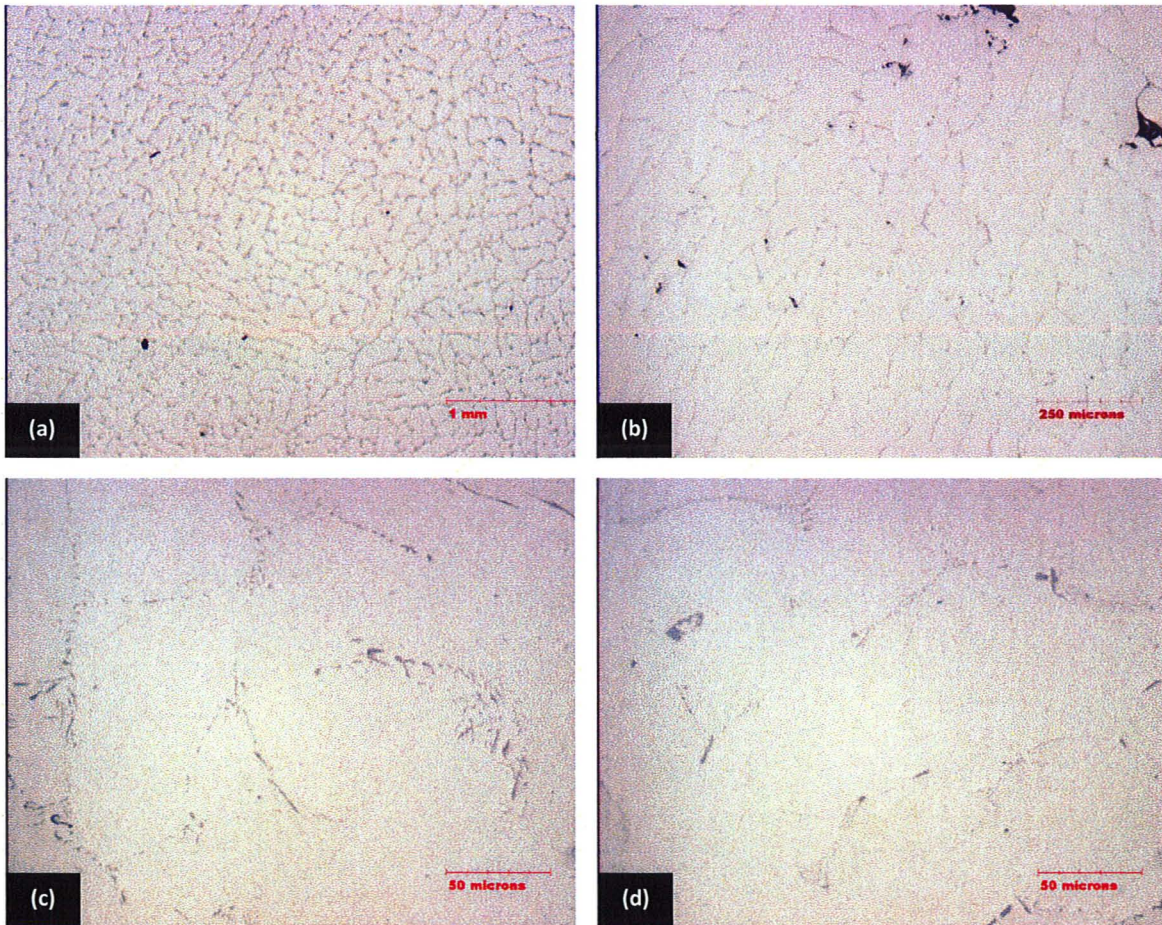


Figure 2-7 Microstructure of A1.G-Fe.3-Si.05 solidified in the graphite crucible at different magnifications - Optical Microscope

II. Copper Mould (A1.C)

In this sample a mixture of interdentritic and intracellular phases distributed all over the sample can be seen. The intracellular phases can morphologically be divided into three major categories: Chinese scripts, loop-shaped and globular phases. Among these phases, Chinese script and loop-shaped particles dominate (Figure 2-8 (b) and (c)). In interdentritic regions, the needle-like particles are distributed evenly in both the inner parts of the sample and areas close to the surface of the sample.

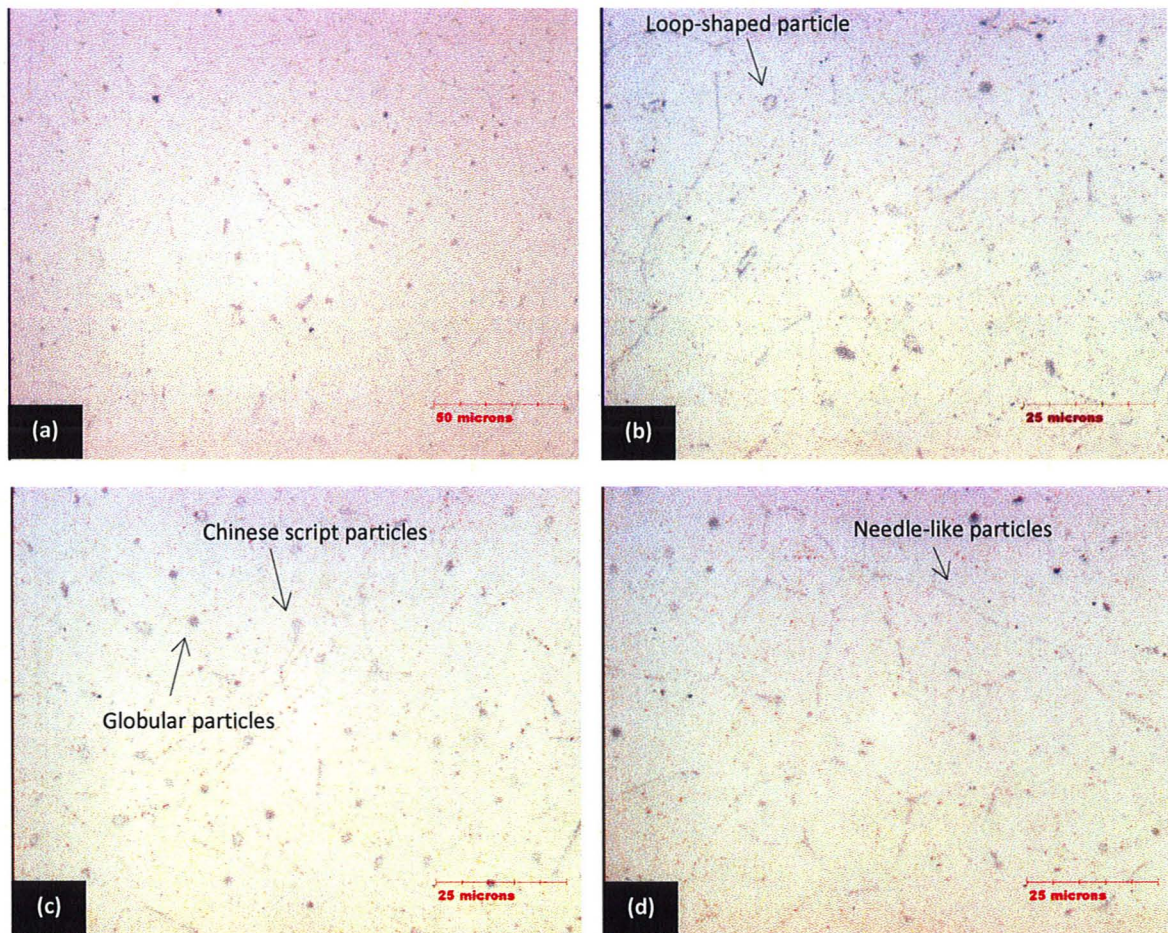


Figure 2-8 Microstructure of A1.C-Fe.3-Si.05 solidified in the copper mould at different magnifications - Optical Microscope

III. *Water-Cooled Copper Mould (A1.W)*

As it is shown in Figure 2-9, two different regions with a fuzzy but identifiable boundary between them can be distinguished in this sample. It is seen that by advancing from contact surface of the sample toward its center, region (I), containing both interdendritic and intracellular phases, transforms to the region (II) containing only interdendritic particles.

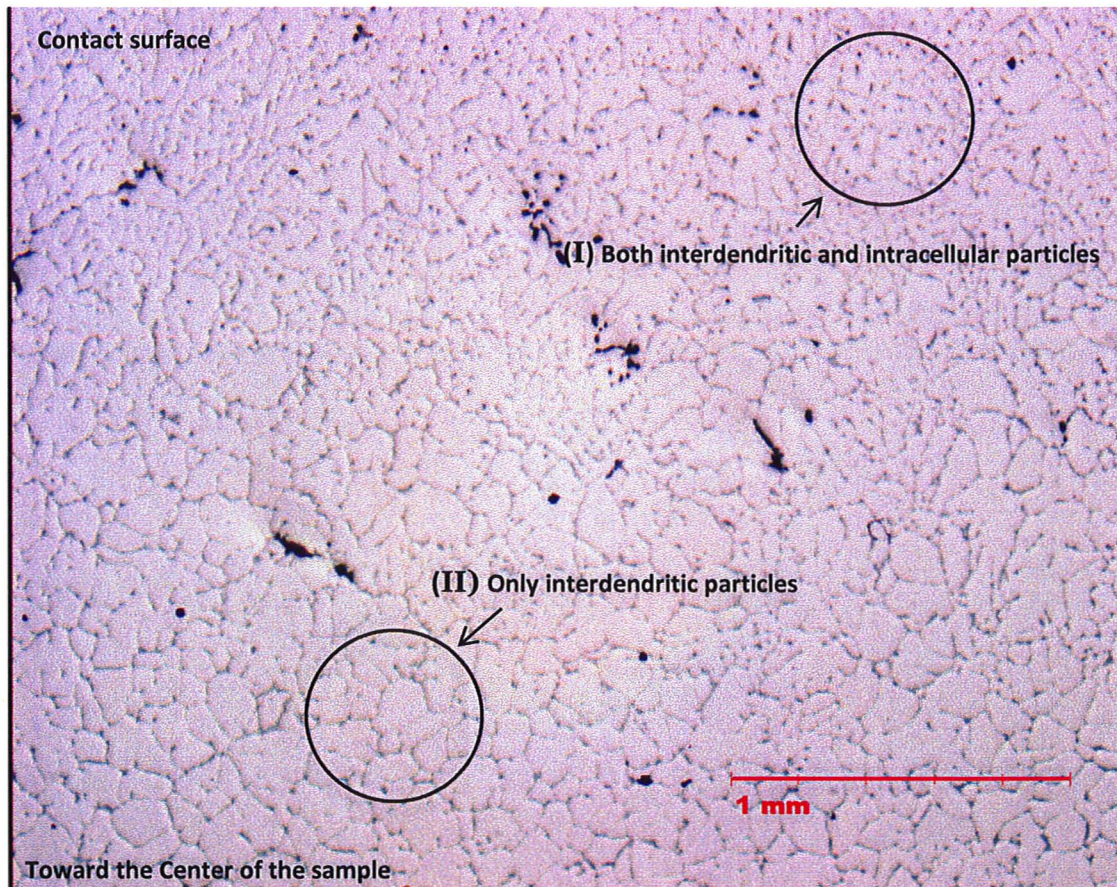


Figure 2-9 Microstructure of A1.W-Fe.3-Si.05 solidified on the water-cooled copper mould - Optical Microscope
Two different areas can be distinguished: I) Close to the surface of the mould II) toward the centre of the sample

These particles at higher magnifications are shown in Figure 2-10. In this figure, (a), (c) and (d) are attributed to the region close to the contact surface and (b), (d) and (f) are related to the inner parts of the sample. We can see that the dominant structures in the region (I) are the globular intracellular and plate-like interdendritic phases while in the region (II) eutectic rod-like phases are the dominant structure.

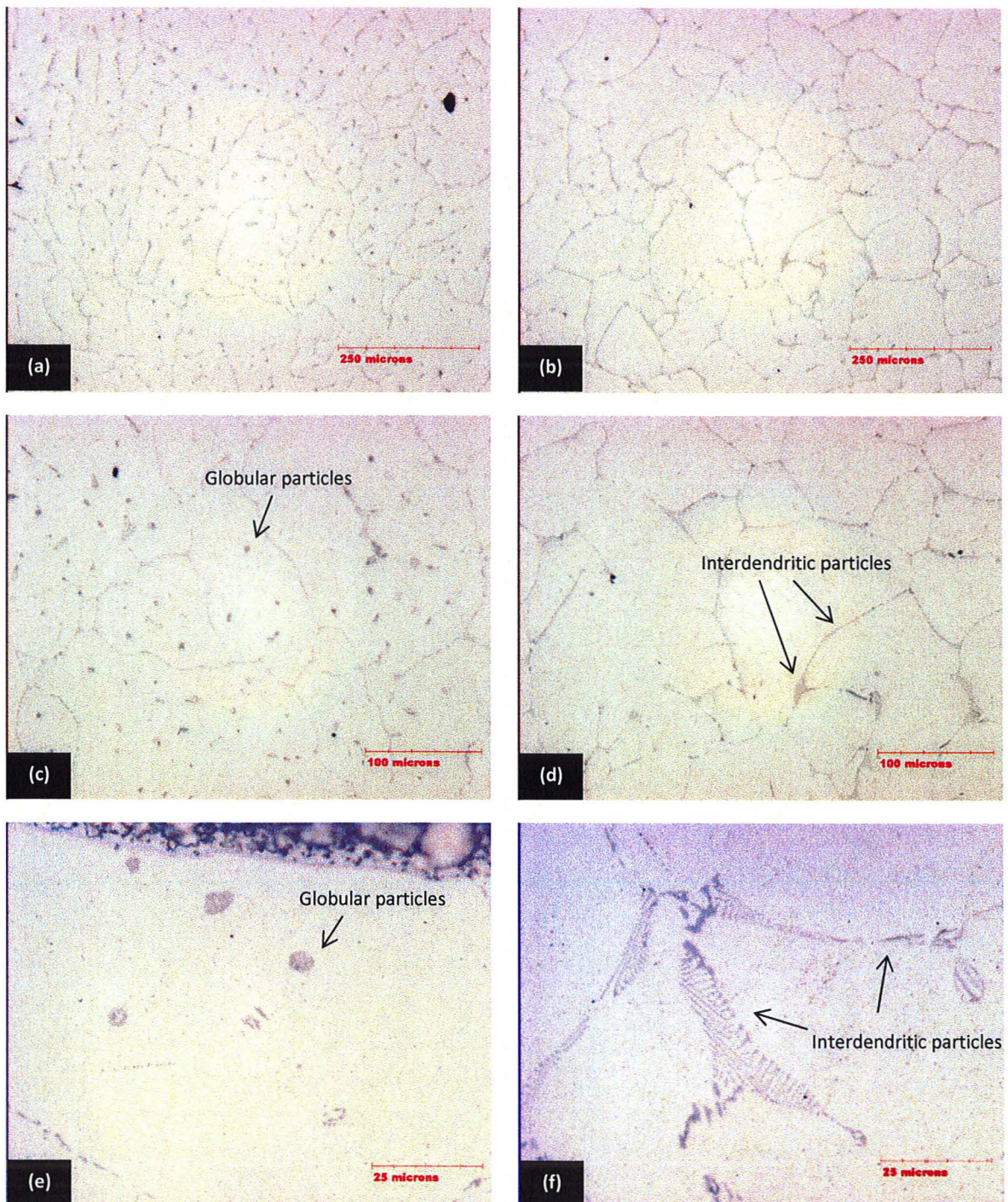


Figure 2-10 Microstructure of A1.W-Fe.3-Si.05 solidified on the water-cooled copper mould - Optical Microscope (a), (c) and (e) close to the contact surface (b), (d) and (f) centre of the sample

b) A2-Fe.3-Si.15 (Alloy #2 with 0.3 wt% Fe and 0.15 wt% Si)

I. Graphite Crucible (A2.G-Fe.3-Si.15)

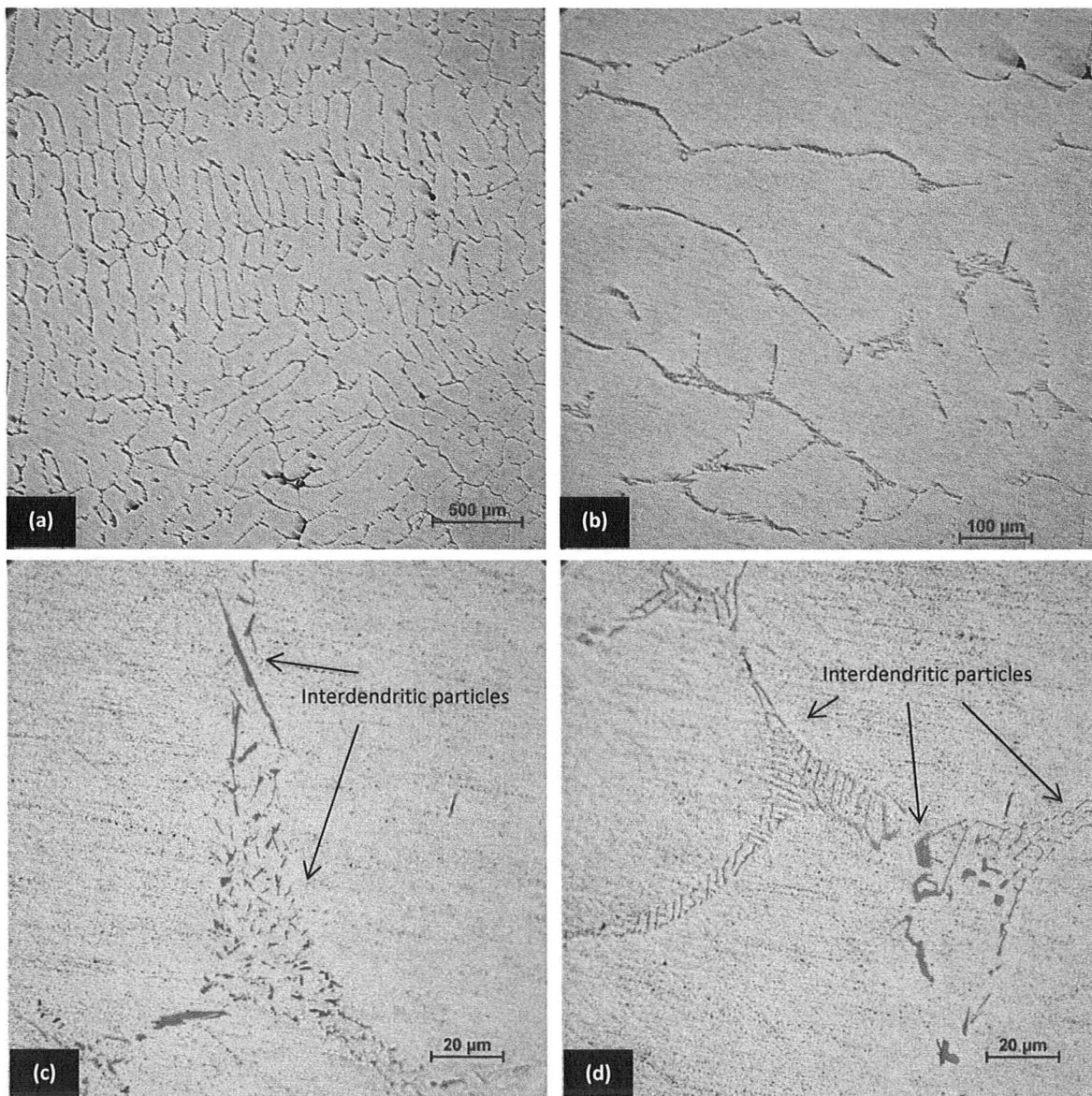


Figure 2-11 Microstructure of A2-Fe.3-Si.15 solidified in the graphite crucible at different magnifications- Optical Microscope

It is seen that similar to the structure obtained in A1.G-Fe.3-Si.05, the dominant microstructure contains different particles distributed in interdendritic regions. These

particles are commonly arranged in groups as if they are formed by a eutectic decomposition.

II. Copper Mould (A2.C-Fe.3-Si.15)

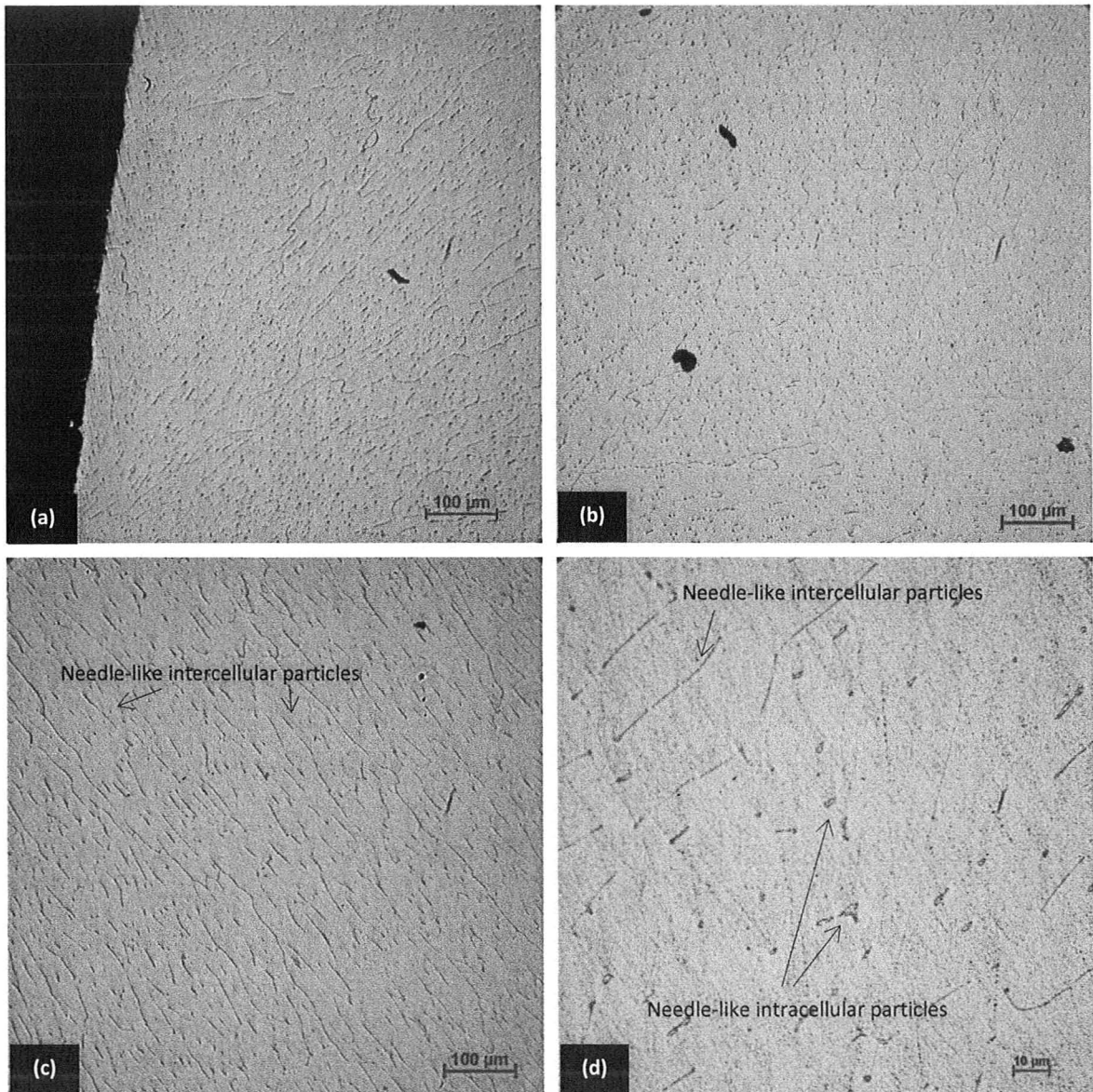


Figure 2-12 Microstructure of A2.C-Fe.3-Si.15 solidified in the copper mould at different magnifications- Optical Microscope

Here in general, a fine distribution of intra and intercellular particles all over the sample is seen. This configuration, in some sections (especially in the inner parts) randomly transform into a regions containing only interdendritic needle-like particles (Figure 2-12-c).

III. Water-Cooled Copper Mould (A2.W-Fe.3-Si.15)

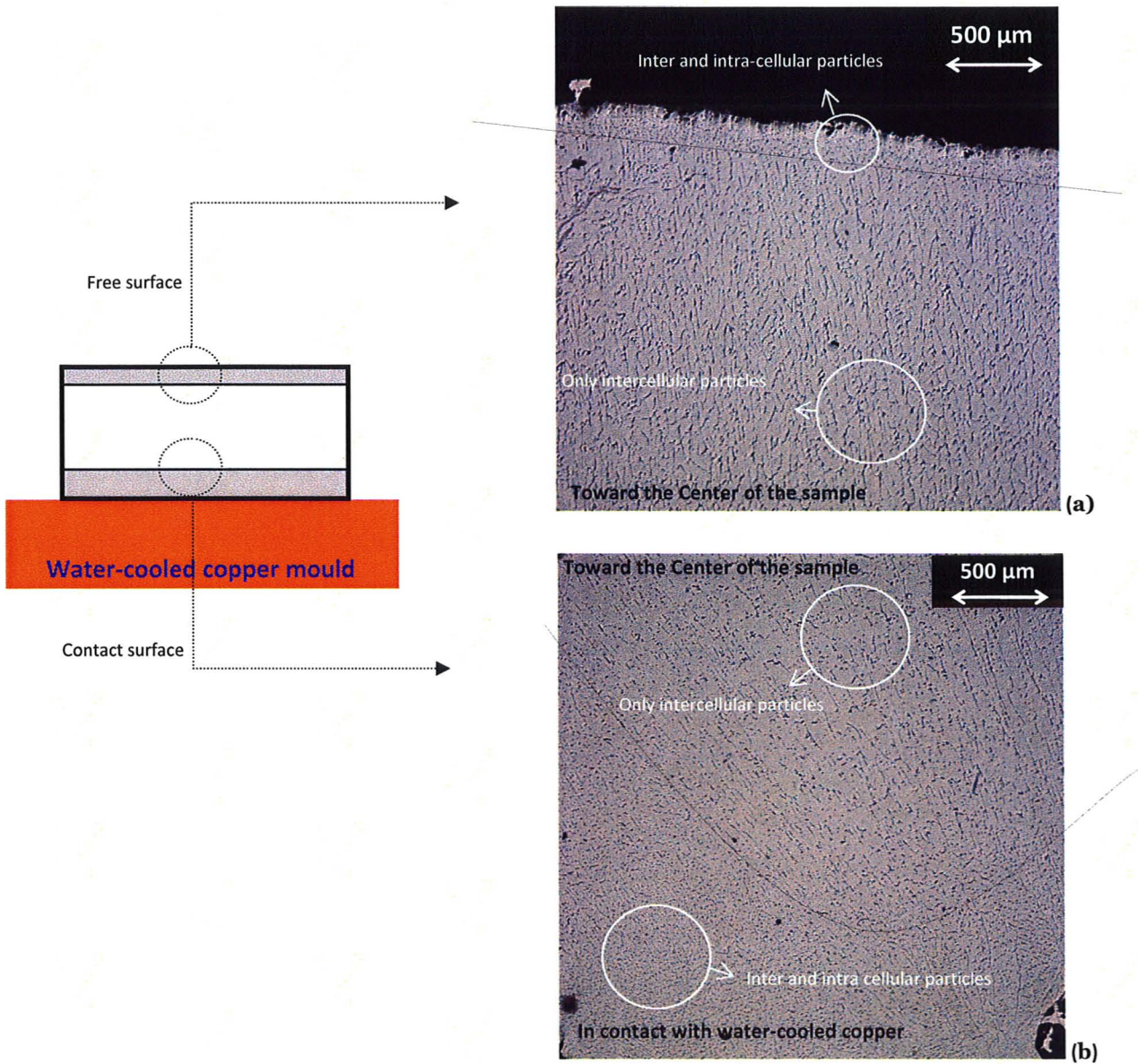


Figure 2-13 Microstructure of A2.W-Fe.3-Si.15 solidified on the water-cooled copper mould- Optical Microscope
 (a) Solidified in contact with air (b) Solidified in contact with surface of the mould

Three different zones with clear but fuzzy boundaries can be distinguished in this sample (Figure 2-13): area close to the contact surface (Figure 2-13-(b)), region solidified in contact with air (Figure 2-13-(a)) and region between free surface and contact surface of the sample.

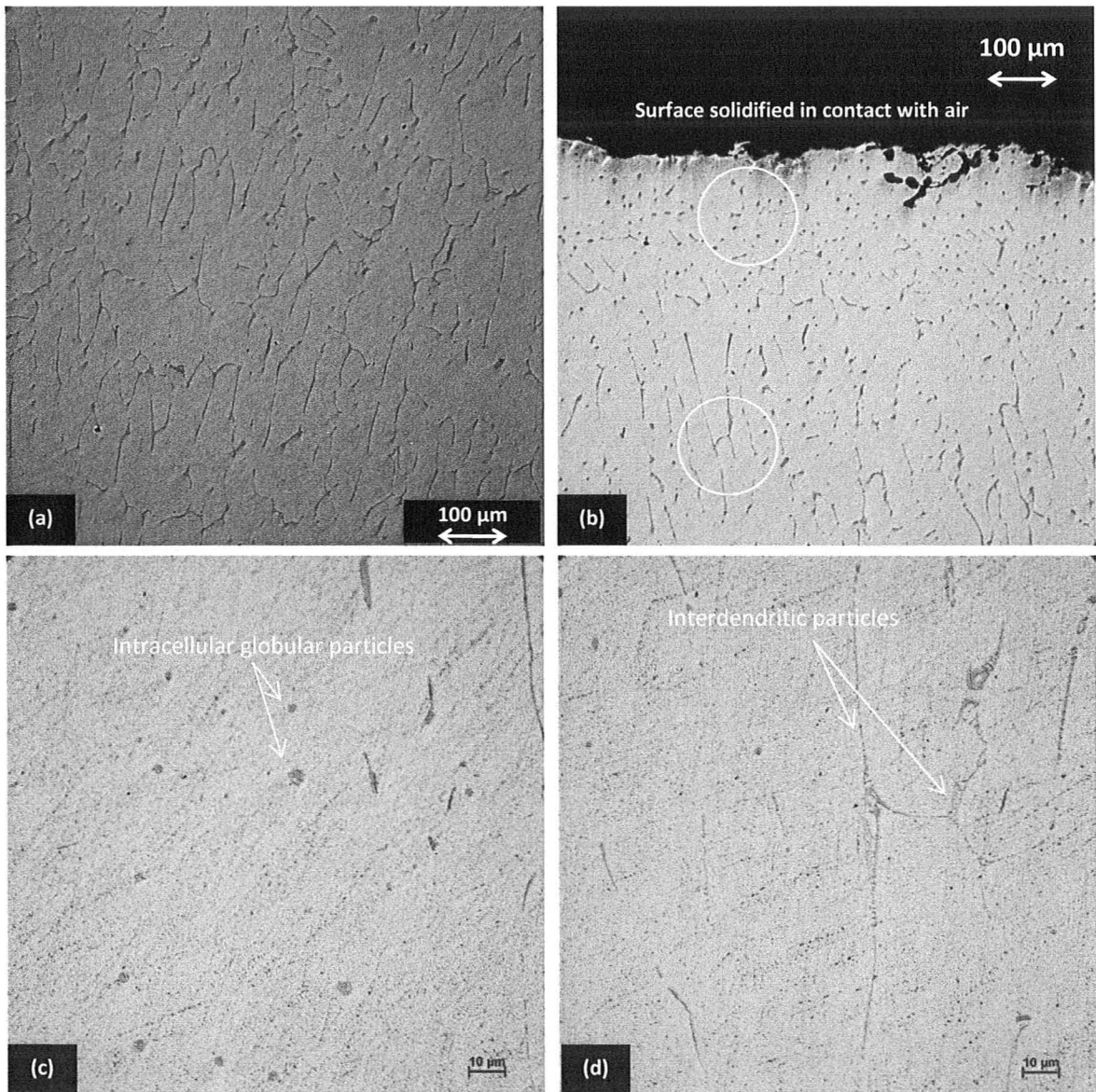


Figure 2-14 Microstructure of A2.W-Fe.3-Si.15 solidified in the water-cooled copper mould- Different magnifications-Optical Microscope

Microstructures of these zones at higher magnifications are shown in Figure 2-14. Again disappearance of the intracellular globular phases in both free surface and contact surface can be seen by advancing toward the center parts of the sample.

c) A3-Fe.3-Si.45 (Alloy #3 with 0.3 wt% Fe and 0.45 wt% Si)

I. Graphite Crucible (A3.G-Fe.3-Si.45)

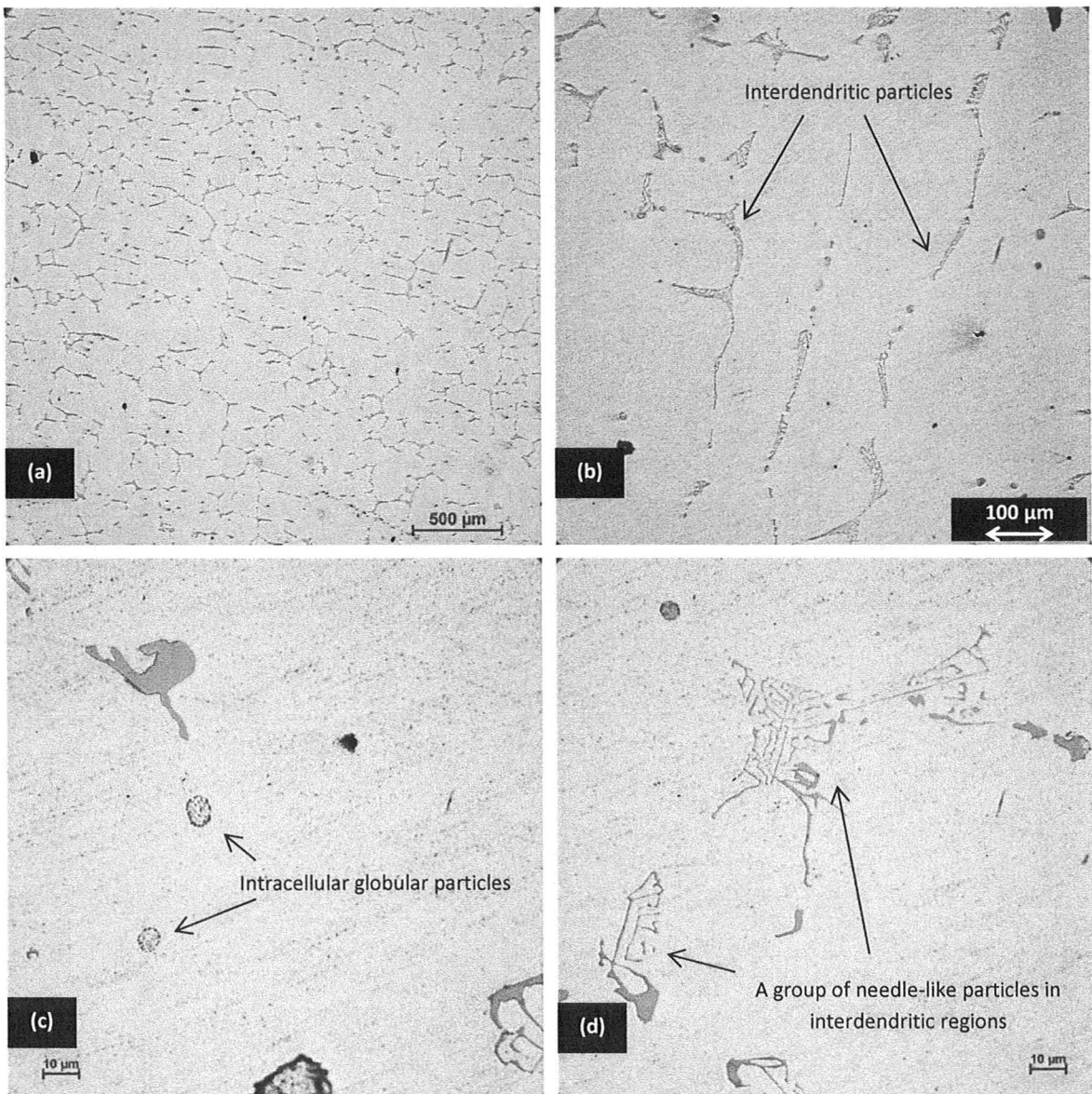


Figure 2-15 Microstructure of A3.G-Fe.3-Si.45 solidified in the graphite crucible- Different magnifications Optical Microscope

Similar to the solidification of previous alloys at low cooling rates, an interdendritic distribution of particles all over the microstructure can be mentioned as the main configuration. A rather discernible difference with A1.G-Fe.3-Si.05 and A2.G-Fe.3-Si.15 is the presence of some globular particles. As seen in Figure 2-15-(c), their existence is very pronounced in this sample.

II. Copper Mould (A3.C-Fe.3-Si.45)

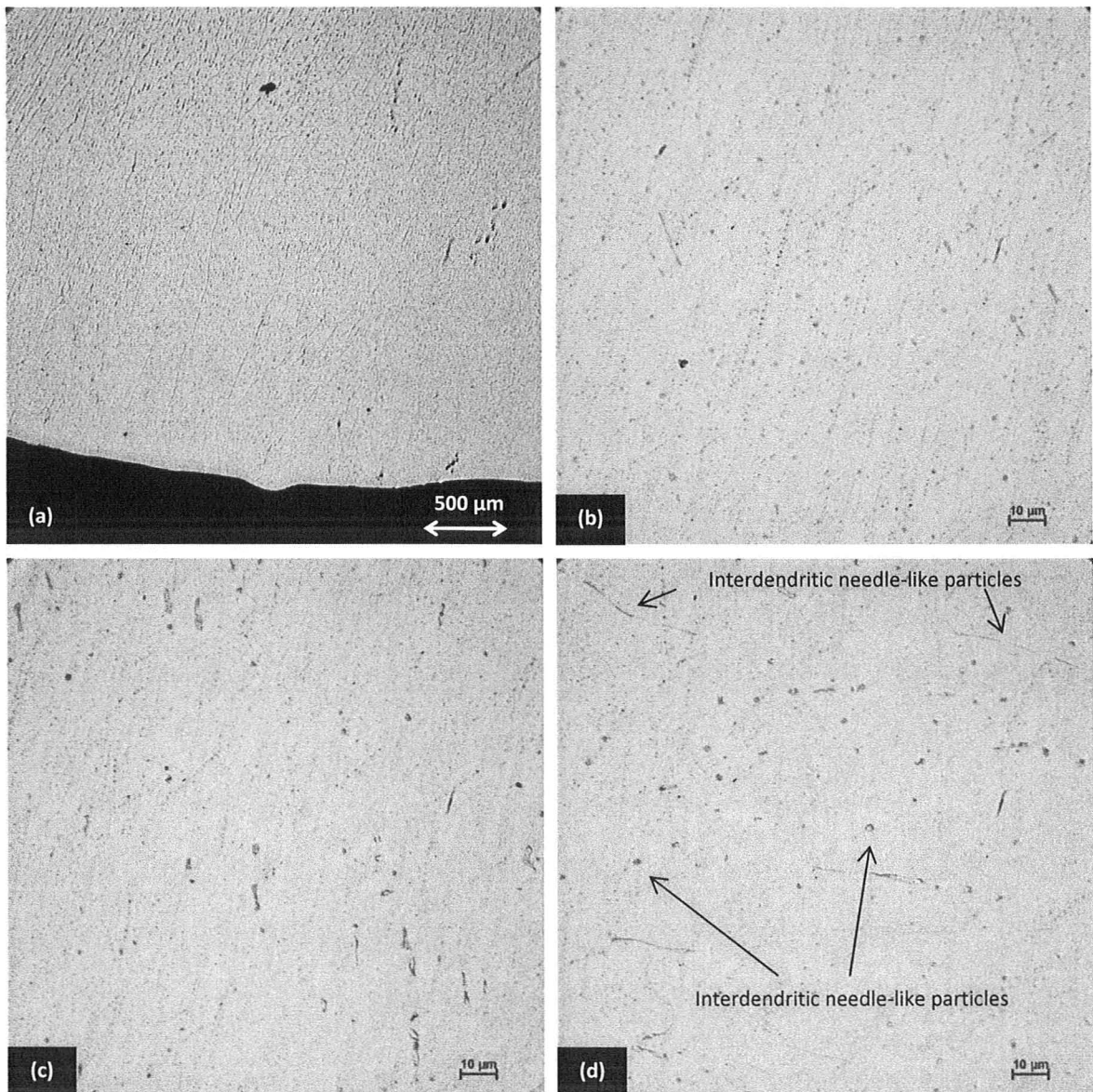


Figure 2-16 Microstructure of A3.C-Fe.3-Si.45 solidified in the copper mould- Optical Microscope

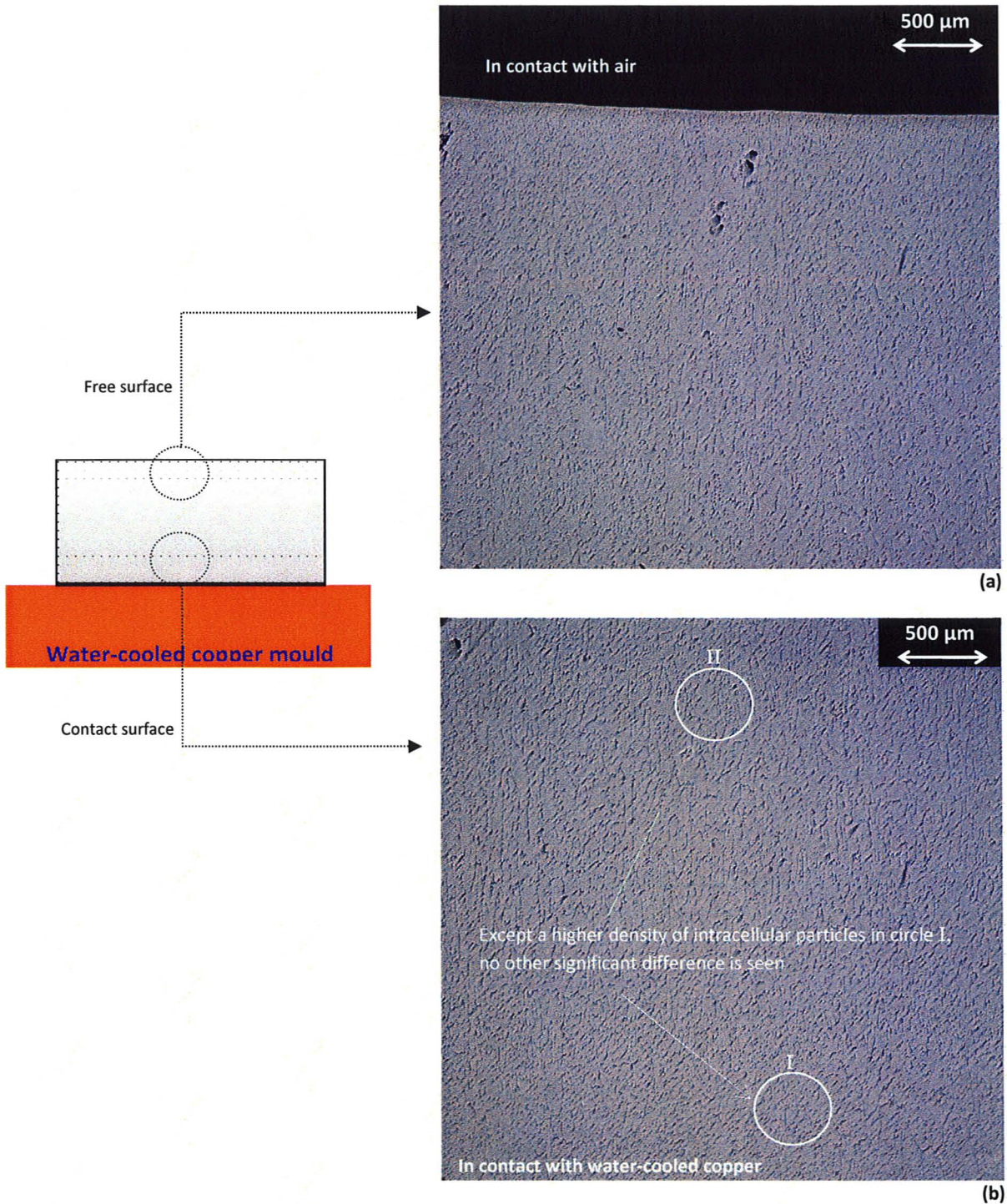


Figure 2-17 Microstructure of A3.W-Fe.3-Si.45 solidified on the surface of the water-cooled copper mould- Optical Microscope (a) Free surface (b) Contact surface

Typical microstructure of this sample, which is a mixture of fine intracellular globular and interdendritic needle-like particles distributed all over the sample, is given in Figure 2-16. It

is worth noticing that, the existence of needle-like interdendritic particles is not as noticeable as that in A1.C-Fe.3-Si.05 and A2.C-Fe.3-Si.15.

III. Water-Cooled Copper Mould (A3.W)

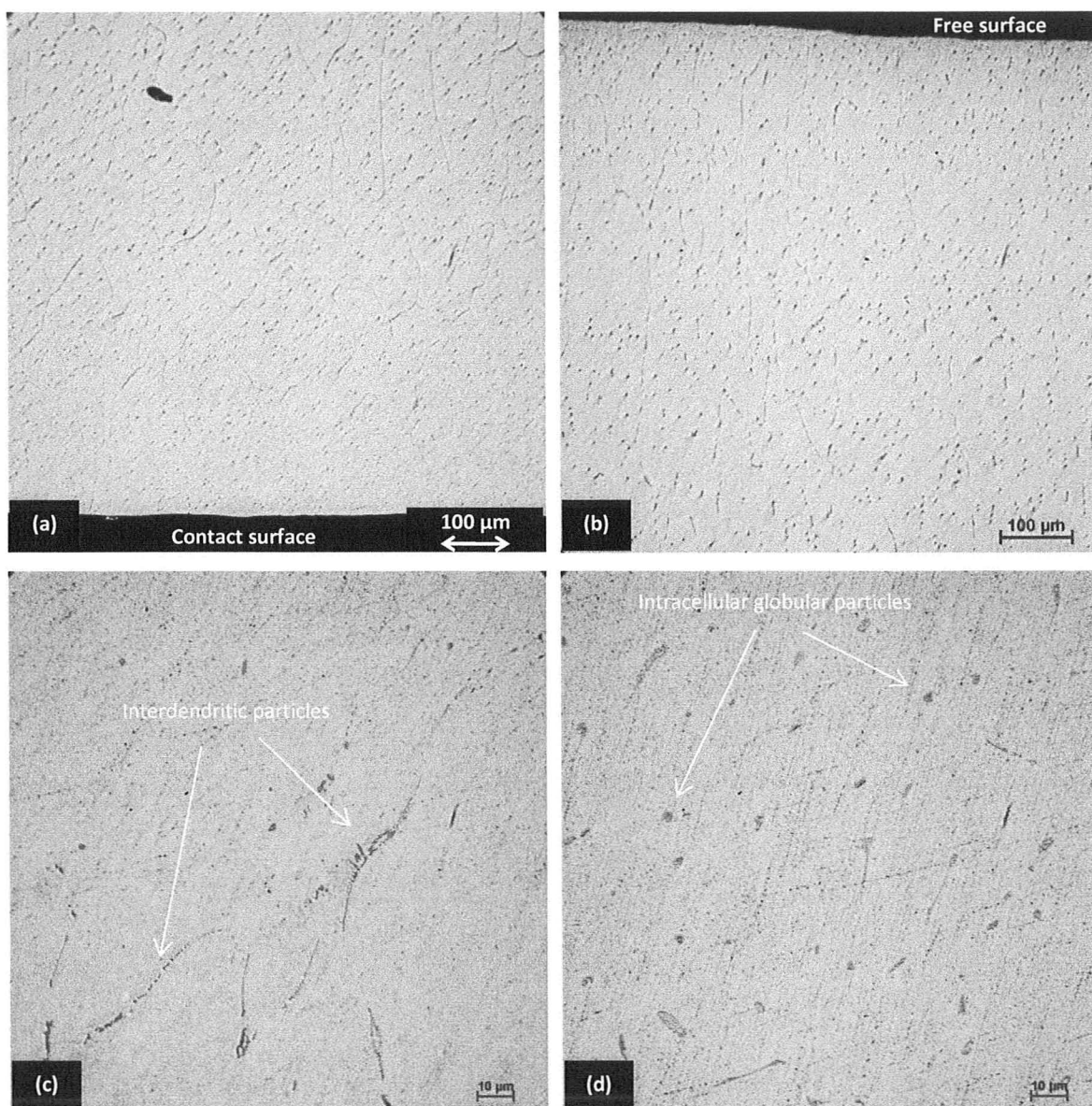


Figure 2-18 Microstructure of A3-Fe.3-Si.45 solidified on the water-cooled copper mould- Different sections and magnifications- Optical Microscope

Overall features of contact surface and free surface of this sample are shown in Figure 2-17. It is worth mentioning that unlike the microstructure of previous alloys,

there are no identifiable zones in contact surface and free surface of this sample. The only discernible difference is the higher density of globular particles in intracellular spaces of areas close to the contact surface.

d) **A4-Fe.5- Si.2 (alloy #4 with 0.5 wt% Fe and 0.2 wt% Si)**

I. **Graphite Crucible (A4.G-Fe.5-Si.2)**

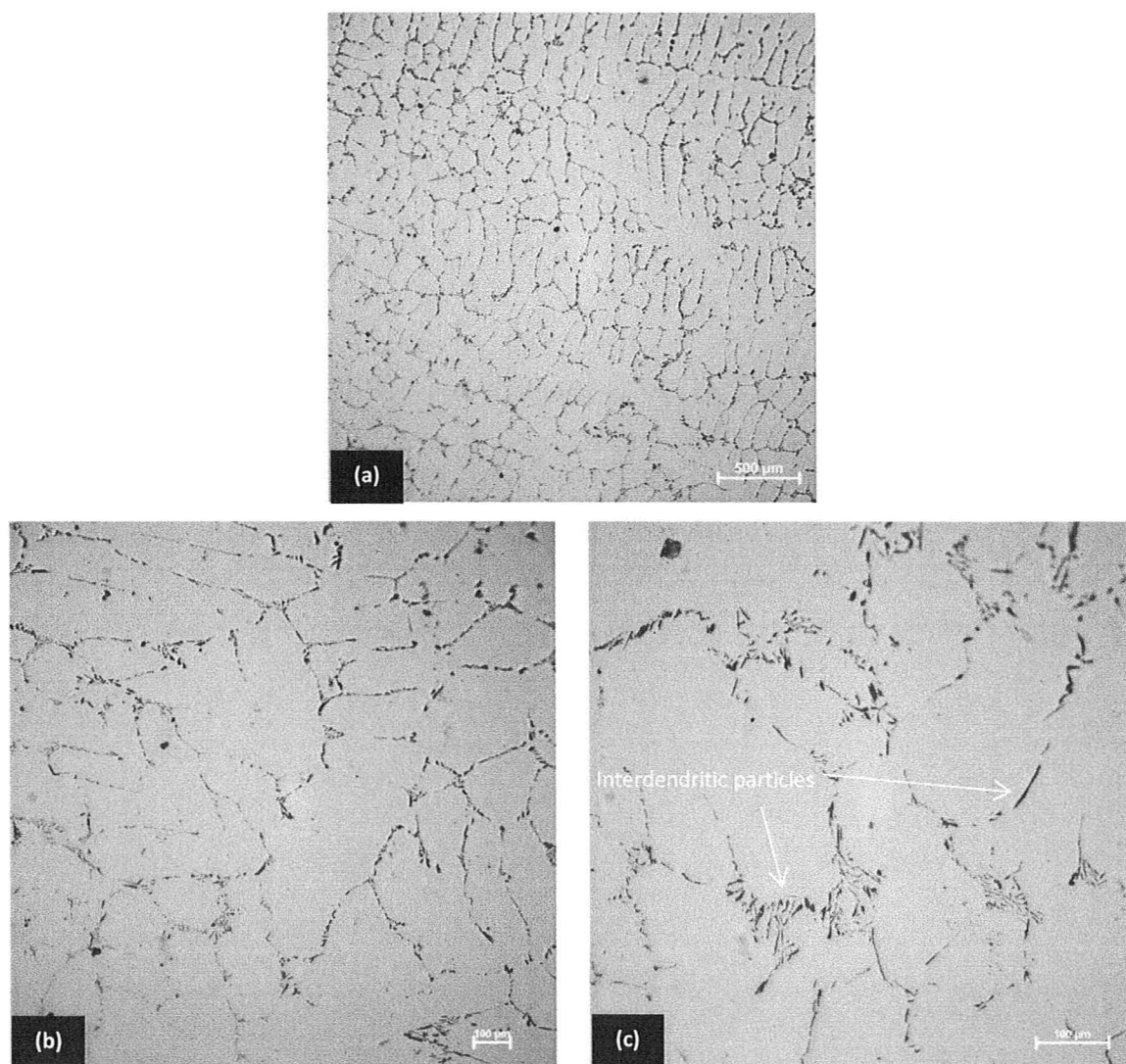


Figure 2-19 Microstructure of A4-Fe.5-Si.2 solidified in the graphite crucible- Different magnifications- Optical microscope

Not surprisingly and similar to the previous samples solidified at low cooling rates, intermetallic phases formed in the interdendritic regions observed all over the microstructure. Particle configuration in interdendritic spaces is either in the form of single needle-shaped particles or in a group of particles typical for eutectic decomposition.

II. *Copper Mould (A4.C-Fe.5-Si.2)*

Two major features observed in this sample are shown in Figure 2-20 (a) and (b). These features are mainly associated with areas close to the contact surface and areas in the middle of the sample respectively.

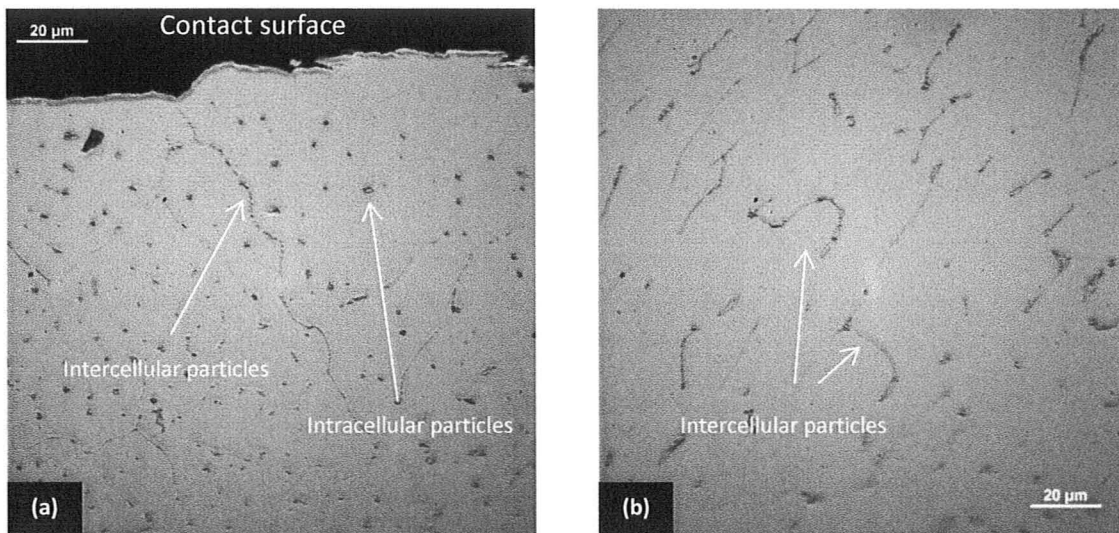


Figure 2-20 Microstructure of A4-Fe.5-Si.2 solidified in the cylindrical copper mould –Optical microscope
a) close to the surface b) middle of the sample

III. *Water-Cooled Copper Mould (A4.W-Fe.5-Si.2)*

Similar to A1-Fe.3-Si.05 and A2-Fe.3-Si.15, two different zones with fuzzy but identifiable boundaries are distinguishable in the free surface and contact surface of this

sample (Figure 2-21). Microstructures of these zones at higher magnifications are given in Figure 2-22.

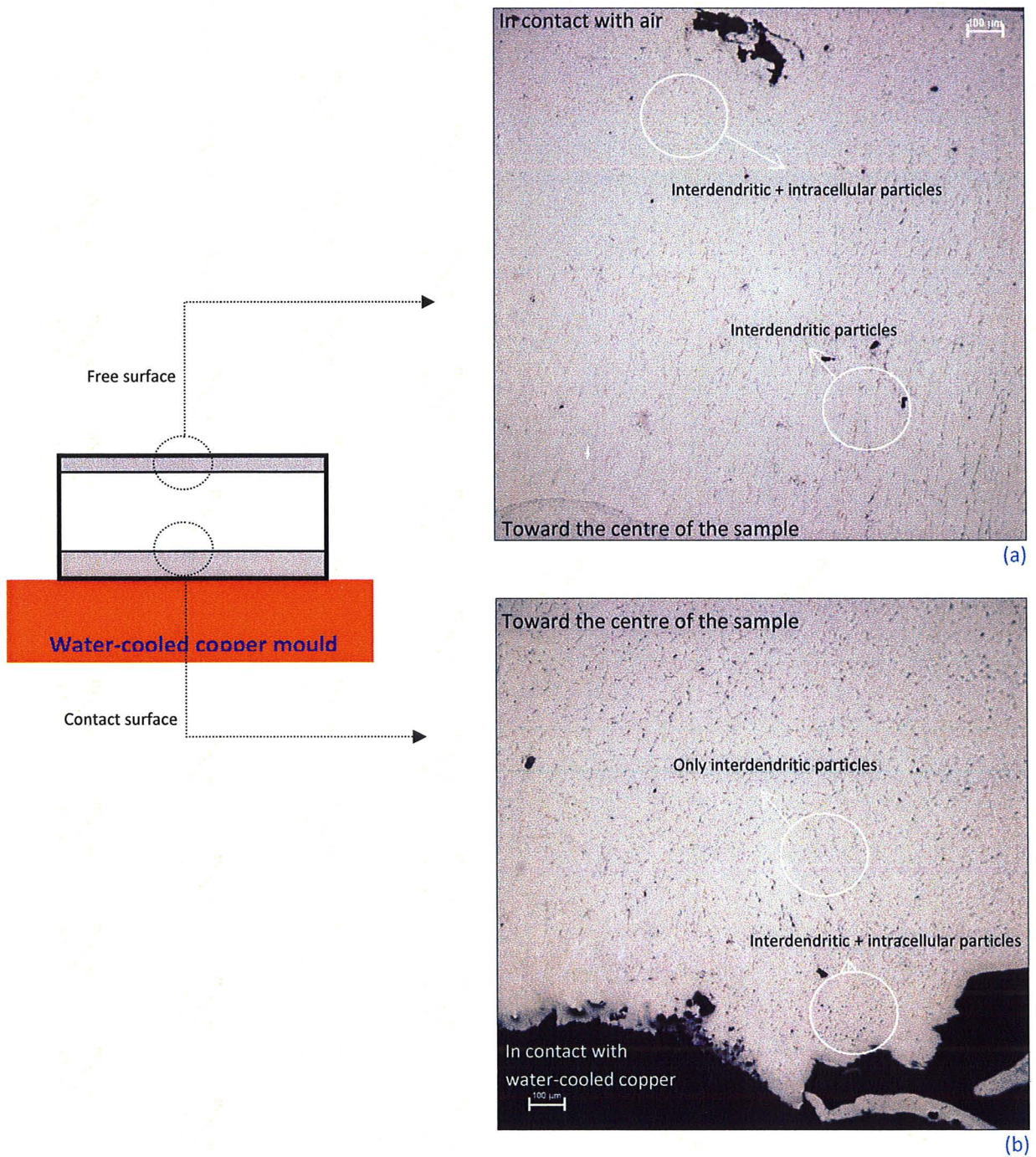


Figure 2-21 Microstructure of the of A4-Fe.5-Si.2 solidified on the water-cooled copper- Optical microscope (a) free surface (b) Contact surface

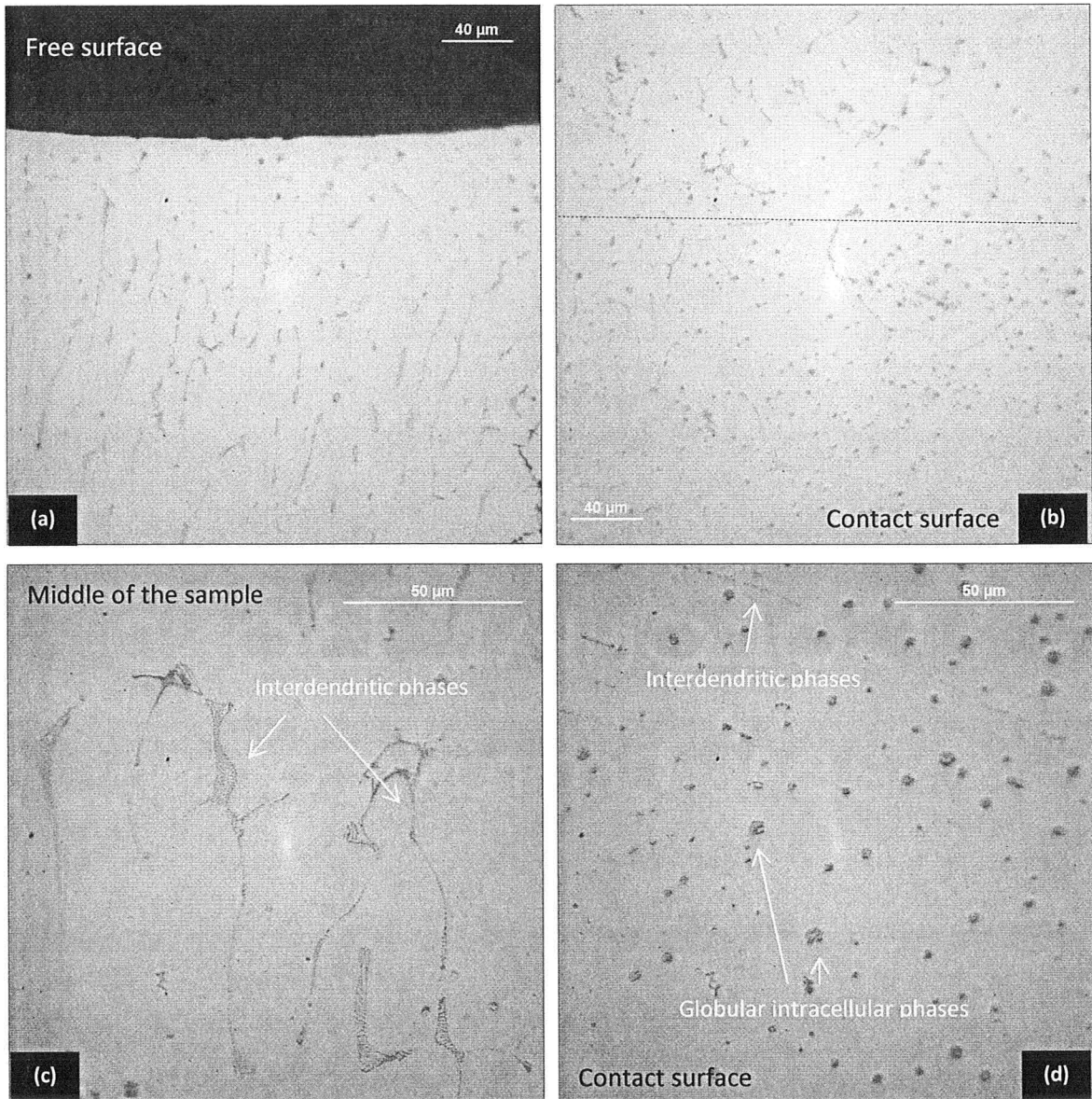


Figure 2-22 Microstructure of A4.Fe.5-Si.2 solidified on the water-cooled copper- different locations and magnifications- Optical microscope

2.2.4.2 Scanning Electron Microscope (SEM)

Some images from microstructure of ribbons produced by using the melt spinner are presented in Figure 2-23. As seen, globular particles are distributed all over the sample and

needle-like interdendritic precipitates and curved-shaped intracellular particles are rarely seen in these samples.

It is worth mentioning that the microstructure of all ribbons, with different compositions, is almost the same and there are no significant differences in terms of configuration of intermetallic particles.

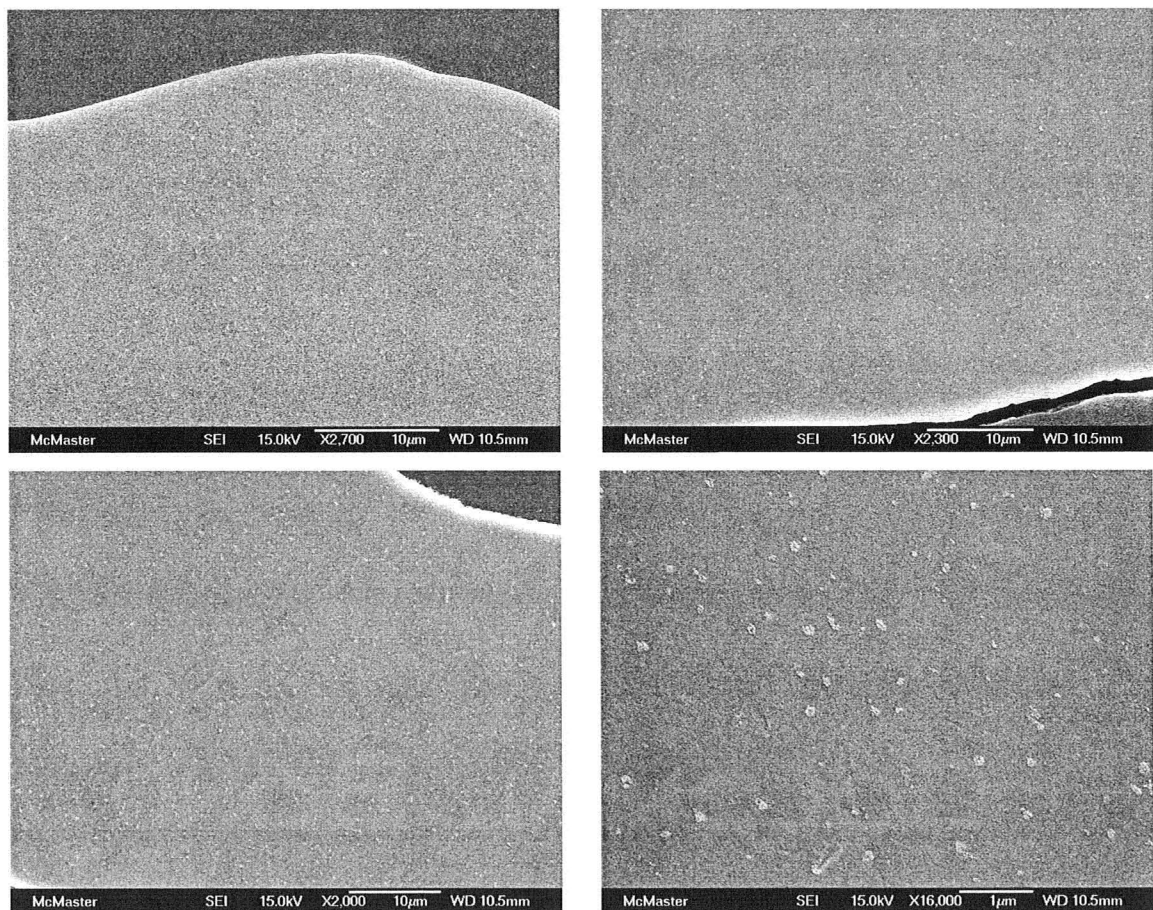


Figure 2-23 SEM images of microstructure of the ribbons produced by melt spinner-A1-Fe.3-Si.05

Deep-etched samples were prepared by immersing them for 4-5 minutes into boiling phenol. The results are presented in Figure 2-24, Figure 2-25 and Figure 2-26.

A vast majority of interdendritic phases in the sample solidified in graphite crucible, has a rod-like morphology which in some cases is seen in a combination with plate-like particles (Figure 2-24 (d) and (e)). Also, low density of globular particles was seen in intracellular regions (Figure 2-24 (f)). Though EDAX (Energy-dispersive X-ray Spectroscopy) examinations of these particles were not successful in determining type of the phases; but, the results showed that these globular phases in general contain higher amount of silicon compare to the other phases.

A majority of particles in the sample solidified in the copper mould (Figure 2-25) are rod-like intermetallics located in the interdendritic regions, but, also a great amount of intracellular particles which have either spiral-like or chest-bone like morphologies (Figure 2-25 (d), (e) and (f)).

A noticeable difference between the rod-like structures in the sample solidified in the graphite crucible and the sample solidified in the copper mould is the tendency of these rods for cross-linking at higher cooling rates (copper mould). As seen in Figure 2-25 (a) and (b), these rods are completely attached together and their arrangement resembles a plate-shaped precipitate.

The sample solidified in the water-cooled copper mould (Figure 2-26) demonstrates a rather complex mixture of particles with four different morphologies: interdendritic plate-like and rod-like phases (Figure 2-26 (a) and (b)), intracellular chest-bone structures (Figure 2-26 (c)) and intracellular globular particles (Figure 2-26 (d), (e)) which in some cases have formed a dumbbell-shaped precipitates through attaching each other (Figure 2-26 (f)).

a) A1.Fe.3-Si.05 (alloy #1 with Fe=0.3 wt% and Si=0.05 wt%) --- Deep Etched Sample

I. Graphite Crucible (A1.G-Fe.3-Si.05)

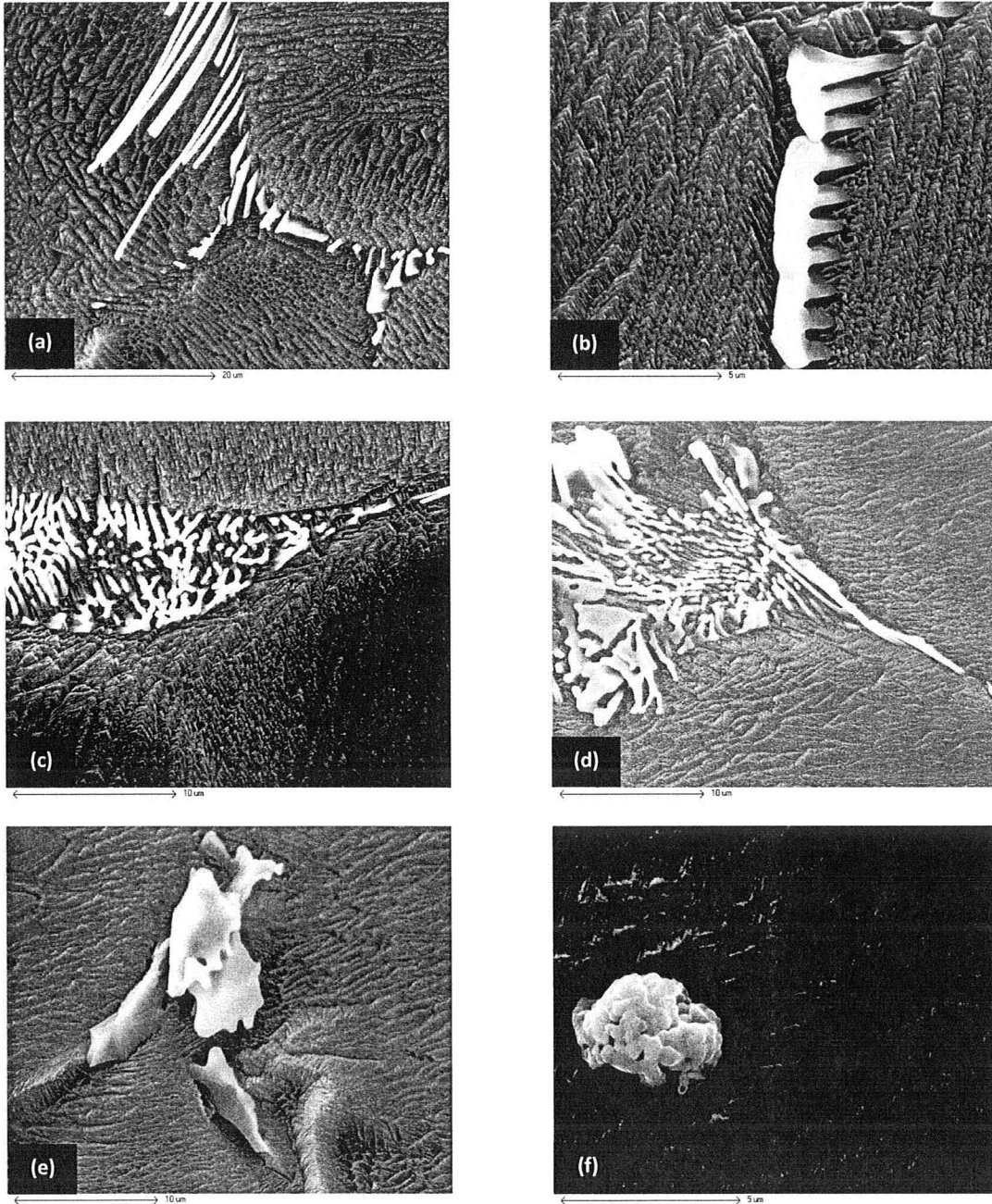


Figure 2-24 SEM images of intermetallics observed in deep-etched sample of A1-Fe.3-Si.05 solidified in the graphite crucible

(a), (b), (c) and (d) rod-like morphology (e) plate-like morphology (f) rarely seen globular particle

I. Copper Mould (A1.C-Fe.3-Si.05)

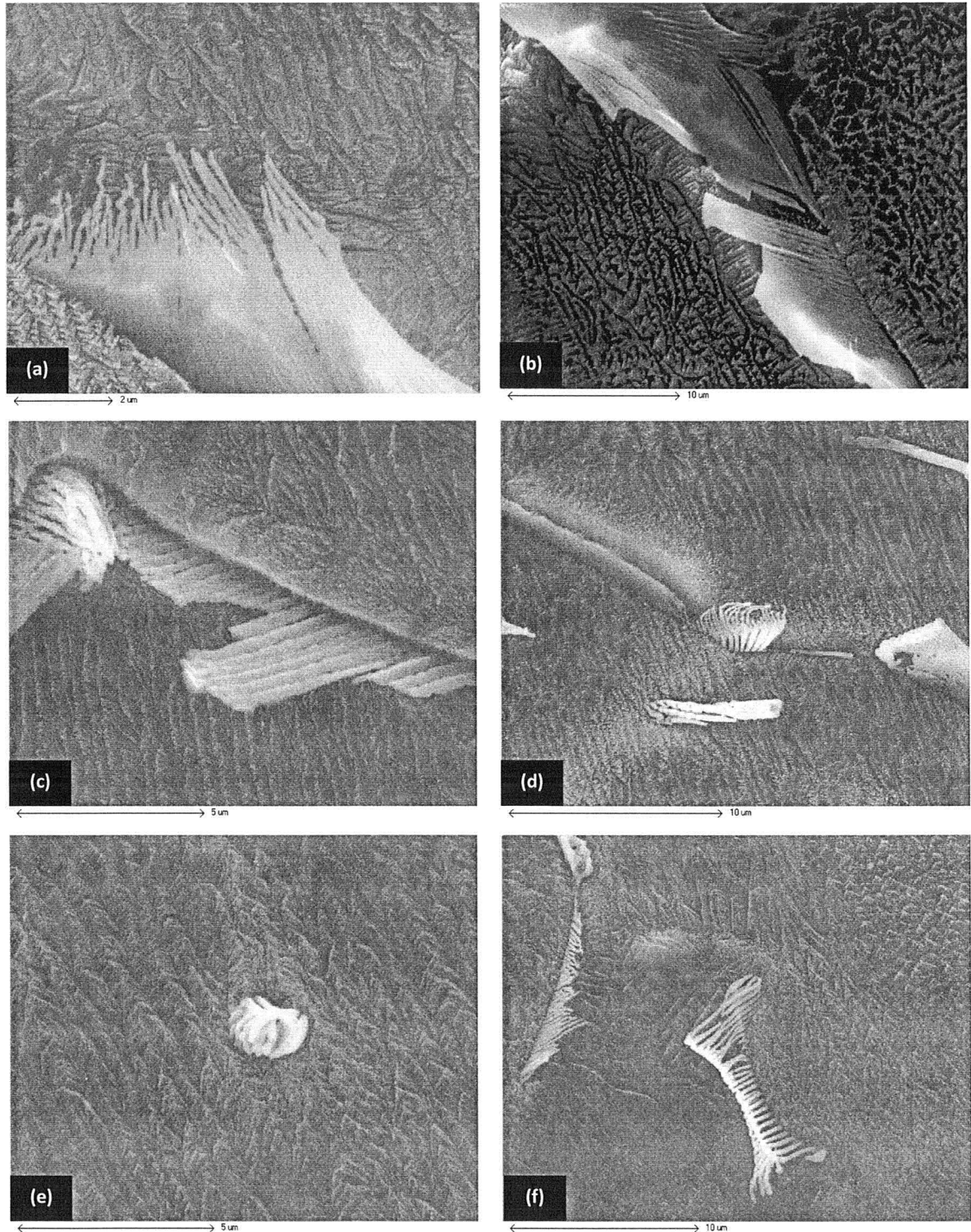


Figure 2-25 SEM images of intermetallics observed in deep-etched sample of A1-Fe.3-Si.05 solidified in the copper mould (a), (b) and (c) cross-linked rods (d) spiral-like particles (e) and (f) chest-bone morphology

II. Water-Cooled Copper Mould (A1.W-Fe.3-Si.05)

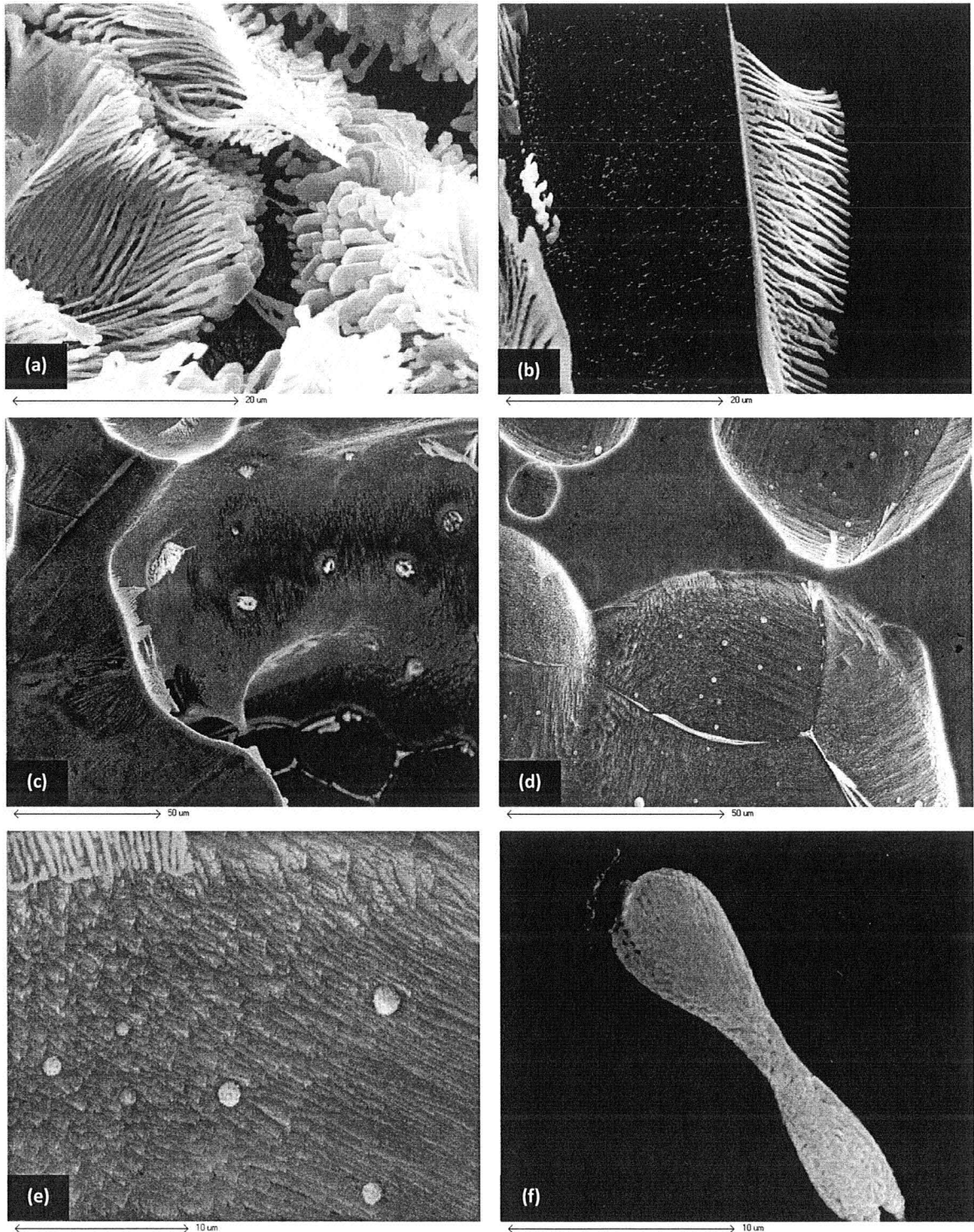


Figure 2-26 SEM images of intermetallics observed in deep-etched sample of A1-Fe.3-Si.05 solidified in the water-cooled copper mould (a) and (b) dense population of rod-like and plate-like structures (c), (d) and (e) globular particles (f) connected globular particles (dumbbell-shaped precipitates)

2.2.5 X-Ray Diffraction analysis

XRD profiles and conditions under which these patterns are obtained are presented in Appendix #3 for all samples. These spectra are analyzed by using computer software called "JADE". It is worth noticing that:

- The chemical formula of phases named " $\text{Al}_{62}\text{Fe}_{32}\text{Si}_6$ " and " $\text{Al}_{96}\text{Mn}_{24}\text{Si}_{18}$ ", are not reported in Table 1-3 in chapter one. Comparing the lattice parameters of these phases (in Table 2-3) with lattice parameters of phases reported by Kral [2005] (Table 1-3), one can see that " $\text{Al}_{62}\text{Fe}_{32}\text{Si}_6$ " and " $\text{Al}_{96}\text{Mn}_{24}\text{Si}_{18}$ " are close to $\alpha\text{-AlFeSi}$ and $\alpha\text{-Al(Fe,Mn)Si}$ respectively.

Table 2-3 Crystallographic information of "Cubic- α + Mn" and "Cubic- α , No Mn" in JADE software

Name of the phase	Chemical formula	Crystal structure	Lattice parameter (nm)		
			a	b	b
Cubic- α	$\text{Al}_{62}\text{Fe}_{32}\text{Si}_6$	Cubic	1.256	1.256	1.256
Cubic- α	$\text{Al}_{96}\text{Mn}_{24}\text{Si}_{18}$	Cubic	1.264	1.264	1.264

- Lattice parameters of the phase named " $\text{Al}_{90}\text{Fe}_{20}$ " with chemical formula $\text{Al}_m\text{Fe}_{94}$ in JADE software, are very close to Al_mFe . In other words, $\text{Al}_{90}\text{Fe}_{20}$ in JADE software is in fact Al_mFe .

A summary of obtained results from extracted particles of samples cast from 100 °C above liquidus and samples cast from 350 °C above liquidus is presented in Table 2-4 and Table 2-5.

Table 2-4 XRD results obtained from extracted particles (Casting Temperature $\approx 760^\circ\text{C}$)

Cs^{-1}		Alloy #1 (Fe=0.3 Si=0.05)	Alloy #2 (Fe=0.3 Si=0.15)	Alloy #3 (Fe=0.3 Si=0.45)	Alloy #4 (Fe=0.5 Si=0.2)
Less than 1	Graphite Crucible	Al_mFe Al_xFe Al_3Fe $\alpha_c\text{-Al}_{96}\text{Mn}_{24}\text{Si}_{18}$	Al_3Fe Al_mFe $\alpha_c\text{-Al}_{96}\text{Mn}_{24}\text{Si}_{18}$	$\alpha_c\text{-Al}_{62}\text{Fe}_{32}\text{Si}_6$ $\alpha_c\text{-Al}_{96}\text{Mn}_{24}\text{Si}_{18}$	Al_3Fe Al_9Fe_2
10 - 20	Copper	Al_mFe Al_xFe	$\alpha_c\text{-Al}_{96}\text{Mn}_{24}\text{Si}_{18}$ $\alpha_c\text{-Al}_{62}\text{Fe}_{32}\text{Si}_6$	$\alpha_c\text{-Al}_{62}\text{Fe}_{32}\text{Si}_6$ $\alpha_c\text{-Al}_{96}\text{Mn}_{24}\text{Si}_{18}$	$\alpha_c\text{-Al}_{96}\text{Mn}_{24}\text{Si}_{18}$ $\alpha_c\text{-Al}_{62}\text{Fe}_{32}\text{Si}_6$
Max 500	Water-cooled copper	Al_mFe Al_xFe Al_6Fe $\alpha_c\text{-Al}_{96}\text{Mn}_{24}\text{Si}_{18}$	$\alpha_c\text{-Al}_{96}\text{Mn}_{24}\text{Si}_{18}$ Al_xFe	$\alpha_c\text{-Al}_{62}\text{Fe}_{32}\text{Si}_6$ $\alpha_c\text{-Al}_{96}\text{Mn}_{24}\text{Si}_{18}$	$\alpha_c\text{-Al}_{62}\text{Fe}_{32}\text{Si}_6$ Hexagonal- α Al_xFe Al_6Fe Al_mFe Al_3Fe
Between 10^3 to 10^5	Ribbon 300 μm	$\alpha_c\text{-Al}_{62}\text{Fe}_{32}\text{Si}_6$ Al_xFe Si	$\alpha_c\text{-Al}_{96}\text{Mn}_{24}\text{Si}_{18}$	$\alpha_c\text{-Al}_{96}\text{Mn}_{24}\text{Si}_{18}$ $\alpha_c\text{-Al}_{62}\text{Fe}_{32}\text{Si}_6$	$\alpha_c\text{-Al}_{96}\text{Mn}_{24}\text{Si}_{18}$ Al_xFe Hexagonal- α Al_mFe
	Ribbon 150 μm	$\alpha_c\text{-Al}_{96}\text{Mn}_{24}\text{Si}_{18}$ Al_xFe Hexagonal- α	Al_xFe $\alpha_c\text{-Al}_{96}\text{Mn}_{24}\text{Si}_{18}$ Hexagonal- α	$\alpha_c\text{-Al}_{62}\text{Fe}_{32}\text{Si}_6$ $\alpha_c\text{-Al}_{96}\text{Mn}_{24}\text{Si}_{18}$	$\alpha_c\text{-Al}_{96}\text{Mn}_{24}\text{Si}_{18}$ $\alpha_c\text{-Al}_{62}\text{Fe}_{32}\text{Si}_6$
	Ribbon 70 μm	$\alpha_c\text{-Al}_{96}\text{Mn}_{24}\text{Si}_{18}$ Al_xFe	-	Al_xFe $\alpha_c\text{-Al}_{96}\text{Mn}_{24}\text{Si}_{18}$	$\alpha_c\text{-Al}_{96}\text{Mn}_{24}\text{Si}_{18}$ $\alpha_c\text{-Al}_{62}\text{Fe}_{32}\text{Si}_6$ Al_xFe Al_mFe

Table 2-5 XRD results from extracted particles from samples with high amounts of super heat
 (Casting Temperature \approx 1000 °C)

	Alloy #1 (Fe=0.3 Si=0.05)	Alloy #2 (Fe=0.3 Si=0.15)	Alloy #3 (Fe=0.3 Si=0.45)	Alloy #4 (Fe=0.5 Si=0.2)
Ribbon 150 μm	Al_mFe $\alpha_c-Al_{96}Mn_{24}Si_{18}$ Al_xFe	$\alpha_c-Al_{96}Mn_{24}Si_{18}$ Al_xFe Al_mFe Hexagonal- α	$\alpha_c-Al_{96}Mn_{24}Si_{18}$ $\alpha_c-Al_{62}Fe_{32}Si_6$	$\alpha_c-Al_{96}Mn_{24}Si_{18}$ $\alpha_c-Al_{62}Fe_{32}Si_6$

3 Chapter 3

3.1 Microstructural investigations

As it can be concluded from the literature review, there is no unique morphology of intermetallics in aluminum alloys. Depending on solidification conditions (such as cooling rate), different morphologies can be achieved for a certain phase.

Consequently a morphological investigation is not a reliable method for identifying the intermetallic phases in as cast aluminum alloys. In fact, these types of investigation are suitable for very general conclusions about distribution of particles in as-solidified microstructure, which can be used to support the results obtained from other methods of investigation such as X-ray diffraction (XRD).

In this research, microstructural characterizations by means of optical and scanning electron microscopy, showed four different combinations of particles at inter- and intracellular spaces. These combinations are presented in Figure 3-1.

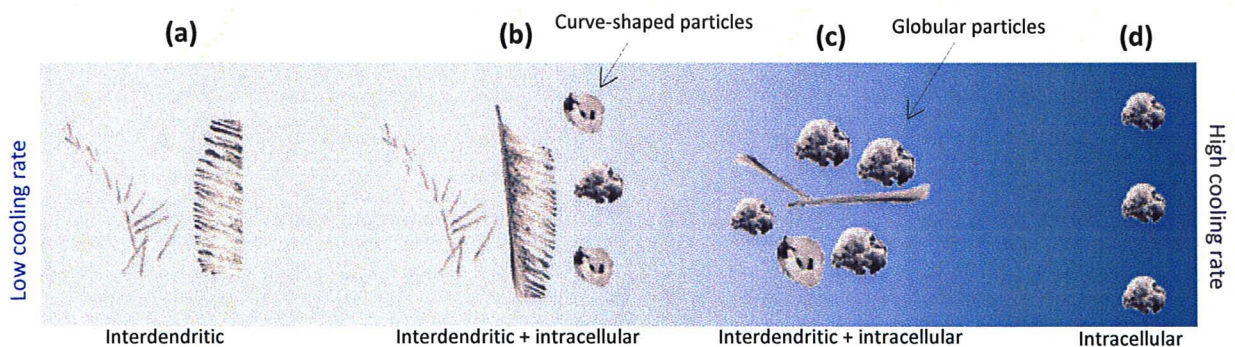


Figure 3-1 Different configurations of particles observed in the microstructures of the samples

Combination (a), which contains needle-like and feather-like precipitates in interdendritic spaces, is only seen at low cooling rates attained for instance during solidification in a graphite crucible.

Combination (b), which in addition to the needle-like and feather-like intergranular particles contains curve-shaped and globular intracellular particles, is the dominant feature in the samples solidified with higher cooling rates attainable during solidification in copper mould.

Among other casting conditions in this research, solidification of the melt on the surface of the water-cooled copper mould (Figure 3-2) produces the most complex microstructure. It is worthwhile noticing that the solidification condition in this sample is very close to the attainable conditions in a wedge-shaped mould in which variation of cooling rate from one end to another end, results in the formation different particle configurations.

In such solidification conditions, in the regions close to the contact surface of the mould (high cooling rates), combination (c), which is composed of globular particles in the intracellular spaces surrounded by interdendritic needle-like particles, is the dominant feature. A similar ensemble is seen in a narrow bound close to the free surface (the area solidified in contact with air) of the samples.

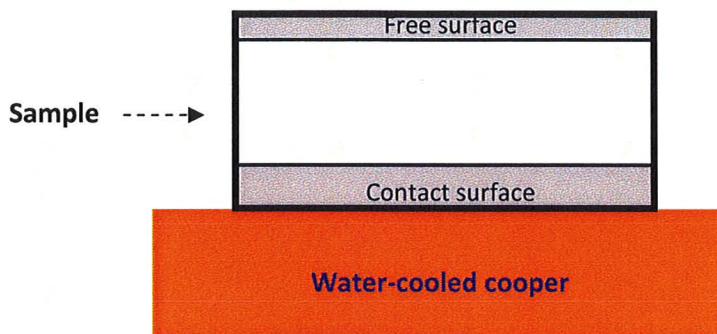


Figure 3-2 schematic of the sample solidified on the surface of the water-cooled copper mould

In the middle sections of the samples, where cooling rates are lower, combination (a) becomes the dominant feature.

It is worth noticing that among all examined compositions in this research, the only exception is composition #3 with 0.3 wt% Fe and 0.45 wt% Si, which has a uniform microstructure all over the sample i.e. the dual microstructure with a fuzzy yet identifiable boundary close to contact surface and free surface of the sample is not formed. The particle configuration in this sample is close to both combination (a) and (c).

This suggests that, unlike other compositions, conditions for the formation of intracellular globular particles are available all over the sample and they can form even at low cooling rates. As the only difference between this alloy (A3-Fe.3-Si.45) and other alloys (A1-Fe.3-Si.05 and A2-Fe.3-Si.15) is the silicon content, then one can conclude that this uniform microstructure is attributed to the higher silicon content of this alloy i.e. Si promotes the formation of globular particles.

Finally, at very high cooling rates corresponding to ribbons produced with the melt spinner, combination (d) mainly containing the globular particles is the dominant feature.

It can be concluded that an increasing cooling rate promotes the formation of globular intracellular particles in the microstructure. Surprisingly, little information is available on the composition and crystal structure of these globular particles. This lack of attention can partly be attributed to the fact that the formation of these particles is promoted at high cooling rates which are not usually encountered in conventional industrial casting processes. In literature, it was reported that these globular particles corresponded to phases with high silicon contents. For example, Khalifa *et.al* [2003] reported Si-rich spheroids in an alloy containing 0.55 wt% Fe and 0.62 wt% Si which was solidified in a graphite crucible [Figure 3-3]. Allen *et.al* [1998] reported a fine dispersion of globular ~0.1-0.2 μm intergranular particles in ribbons of aluminum alloy containing 0.3 wt% Fe and 0.1 wt% Si. Though Allen *et.al* were not able to identify these globular particles by TEM diffraction analysis, but, they reported that these phases would transform to ~0.4 μm faceted equiaxed $\text{Al}_{13}\text{Fe}_4$ particles by heating the as-melt spun ribbons from 625 °C to a temperature range from 653 °C to 658 °C at 2 Kmin^{-1} .

Although an attempt to identify these particles by means of EDAX undertaken in this research was not successful, it was established that they were enriched with Si in comparison with other intermetallics seen in the microstructure.

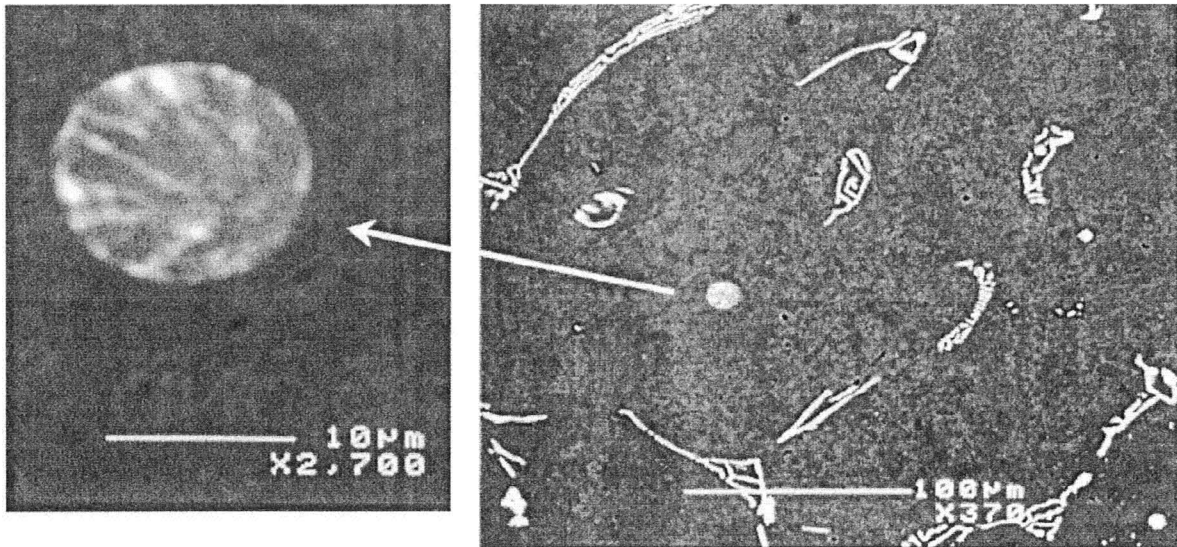


Figure 3-3 Backscattered images from an aluminum alloy (Fe=0.55 wt% Si=0.62 wt%) solidified in a graphite crucible [Khalifa 2003]

The observations, suggest that these globular phases can likely be attributed to initial stages of growth of metastable ternary phases such as α -AlFeSi, which have high silicon content (5-9 wt%). From Figure 2-26-(f) it is suggested that in the later stages of the growth (if enough time is available), these globular phases will probably attach together to make dumbbell-shaped particles.

Since the globular particles are mainly seen in the areas of the samples characterized by high rates of heat extraction during solidification, it can be inferred that high cooling rates promote the formation of ternary metastable phases such as α -AlFeSi over other binary Al-Fe phases in aluminum alloys.

3.2 EDAX examinations

EDAX results were not accurate enough to be used for quantitative phase identification, but, by averaging the silicon content and iron content of randomly analyzed particles, it was established that increasing the cooling rate during solidification, increases both Si and Fe content in the precipitated particles. These investigations were only performed for alloy #1 with 0.3 wt% Fe and 0.05 wt% Si.

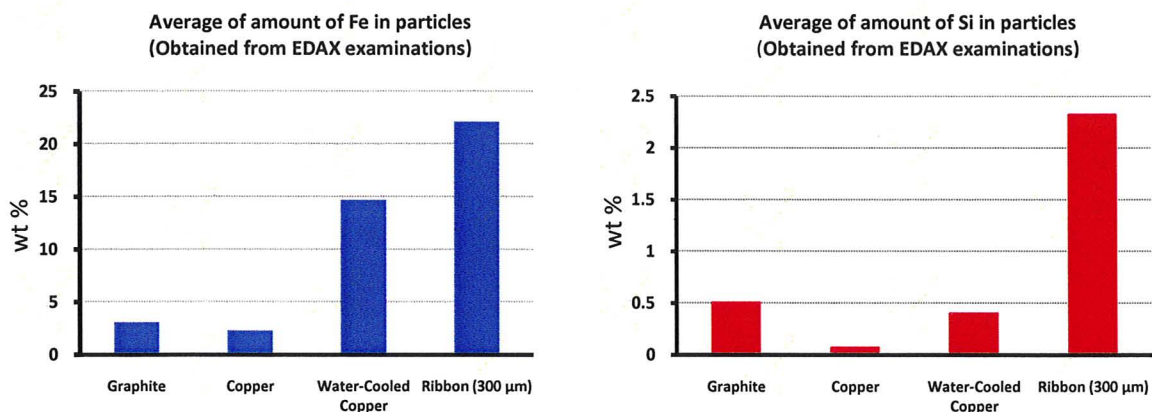


Figure 3-4 Average amount of iron and silicon obtained from EDAX examinations in alloy #1 with 0.3 wt% Fe and 0.05 wt% Si

Comparison of these results with reported values for the range of compositions of different intermetallics in the literature, it can be concluded that by increasing the cooling rate the system moves toward the formation of metastable phases such as α -AlFeSi. Average composition of each intermetallic is presented in Figure 3-5.

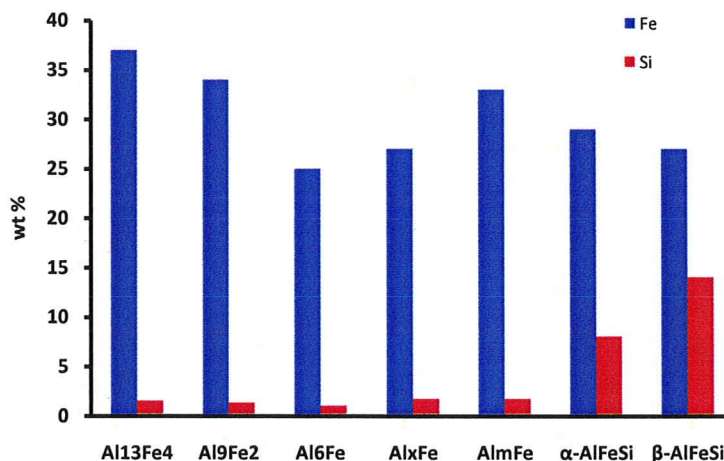


Figure 3-5 Average amount of iron and silicon in different intermetallics based on the reported results in literature

3.3 XRD results

Table 3-1 is a simplified version of Table 2-4 summarizing the obtained XRD results. An analysis of the results yields several interesting tendencies:

1. By increasing both the cooling rate and the amount of silicon in the samples, a transformation from Al-Fe phases toward ternary α -AlFeSi is occurring. In other words, increasing both the cooling rate and the amount of Si can stabilize the α -AlFeSi phase in the microstructure.
2. Among these alloys, alloy #3, with 0.3 wt% Fe and 0.45 wt% Si, is a very special case in which only ternary intermetallics (α -AlFeSi) form at all cooling rates. This specialty can be related to the high Si content of this alloy.
3. From the samples with high iron content (A4-Fe.5-Si.2) it can be concluded that opposite to the effect of silicon, iron stabilizes the binary phases such as Al₃Fe. It can be seen that even at very high cooling rates Al₉Fe₂ forms next to the α -AlFeSi and Al_xFe.

Table 3-1 XRD results from extracted particles of the samples cast from $760\text{ }^{\circ}\text{C}$, $T_c^* \approx 100\text{ }^{\circ}\text{C}$ above liquidus (simplified version)

Cs^{-1}		Alloy #1 (Fe=0.3 Si=0.05)	Alloy #2 (Fe=0.3 Si=0.15)	Alloy #3 (Fe=0.3 Si=0.45)	Alloy #4 (Fe=0.5 Si=0.2)
Less than 1	Graphite Crucible	Al_mFe Al_xFe $\text{Al}_{13}\text{Fe}_4$ α	$\text{Al}_{13}\text{Fe}_4$ Al_mFe α	α	$\text{Al}_{13}\text{Fe}_4$ Al_9Fe_2
10 - 20	Copper	Al_mFe Al_xFe	α	α	α
Max 500	Water-cooled copper	Al_mFe Al_xFe Al_6Fe α	α Al_xFe	α	α Al_xFe Al_6Fe Al_mFe $\text{Al}_{13}\text{Fe}_4$
Between 10^3 to 10^5	Ribbon 300 μm	α Al_xFe	α	α	α Al_xFe Al_mFe
	Ribbon 150 μm	α Al_xFe	α Al_xFe	α	α
	Ribbon 70 μm	α Al_xFe	-	α Al_xFe	α Al_xFe Al_mFe
<ul style="list-style-type: none"> Ternary phases such as "$\alpha_c\text{-Al}_{62}\text{Fe}_{32}\text{Si}_6$", "$\alpha_c\text{-Al}_{96}\text{Mn}_{24}\text{Si}_{18}$" and "Hexagonal-$\alpha$", which represent different types of $\alpha\text{-AlFeSi}$ phase, can be categorized under a same roof. Here, for the sake of simplicity all these phases are denoted by "α". Relating the intensity of the peak of a phase to the fraction of that phase, the dominant phase in each sample can be identified. In This table the dominant phase in each sample is shown with bigger and bolded fonts. 					

* Casting Temperature

4. According to the equilibrium phase diagram $Al_{13}Fe_4$ is the only stable phase expected to be seen in the alloys used in the present research. Except one case, $Al_{13}Fe_4$ forms only in the samples solidified in the graphite crucible. In other words, one should expect to see this phase at very low cooling rates.
5. Al_9Fe_2 is only seen in A4-Fe.5-Si.2 solidified in the graphite crucible. It yields that high Fe content (more than 0.3 wt %) and low cooling rates (less than $1\text{ }^\circ\text{C s}^{-1}$) are minimum required solidification conditions for the formation of Al_9Fe_2 .
6. Another noticeable occurrence is the formation of Al_6Fe , which has happened only in two samples solidified on the surface of water-cooled copper mould. These samples belong to A1-Fe.3-Si.05 and A4-Fe.5-Si.2 which have higher Fe/Si ration compare to other alloys.

Let us recall that in Al-Fe alloys, Al_6Fe is the most common intermetallic in the microstructure. In fact, in these binary systems there is a general agreement that by increasing the cooling rate (or solidification front velocity), the dominant intermetallic will transform from $Al_{13}Fe_4$ to Al_6Fe and Al_xFe . At high cooling rates Al_mFe can form as the dominant metastable intermetallic.

Unlike these trends, it seems that presence of Si ceases the formation of Al_6Fe and promotes Al_xFe in interdendritic spaces. It is worth noticing that the amount of Si in the structure of Al_6Fe is very low (close to zero) and as a result, the amount of Si has no contribution in the destabilization of the structure of this phase. So, one can concluded

that in the presence of Si, such phases as Al_xFe , with higher Si solubility, form prior to the formation of such phases as Al_6Fe , which can accommodate very low amount of Si in their microstructures. Then in latter stages at which most of the silicon is consumed, if solidification time is enough, Al_6Fe may form in interdendritic regions.

7. In general, the variety of intermetallics in the samples solidified on the surface of the water-cooled copper moulds is higher than other samples. This can probably be attributed to the variety of cooling rates achieved in these samples.
8. A comparison of the XRD spectra of the samples with $T_c^* = 760$ °C (ribbon 150 μ m in the Table 3-1) with the samples with $T_c \approx 1000$ °C (in the Table 3-2) shows that superheating stabilized the Al_mFe in the samples with low (A1-Fe.3-Si.05) and intermediate (A2-Fe.3-Si.15) amounts of silicon, whereas this level of superheating does not effect the formation of intermetallics in the samples with high Si content and high Fe content (A3-Fe.3-Si.45 and A4-Fe.5-Si.2 respectively). The effect of superheating is more pronounced in the low Si content specimen (A1-Fe.3-Si.05) in which Al_mFe not only forms but also is the dominant intermetallic in the microstructure i.e. amount of Al_mFe in the microstructure is higher than α .

Superheating can affect both the morphology and nature of the phases in the as-cast microstructure by reducing the number of nuclei available for growth, amount of undercooling achieved during the casting or in some cases (such as lost foam casting and sand casting) by changing the cooling rate [Venkataramani 1995, Bian 2000] (these

* Casting temperature

changes, which are not applicable in the melt spinner, are related to the utilization of heat for rising temperature of the moulds i.e. this effect is attributed to the heat diffusivity and heat capacity of the molds).

Table 3-2 XRD results from extracted particles of the samples with $T_c \approx 1000^\circ\text{C}$, 350°C above liquidus (simplified version)

	Alloy #1 (Fe=0.3 Si=0.05)	Alloy #2 (Fe=0.3 Si=0.15)	Alloy #3 (Fe=0.3 Si=0.45)	Alloy #4 (Fe=0.5 Si=0.2)
Ribbon 150 μm	Al_mFe α Al_xFe	α Al_xFe Al_mFe	α	α

Among these, it seems that existence of short and medium-range orders in the melt and even survival of pre-existing intermetallic phases (such as $\text{Al}_{13}\text{Fe}_4$) at low or intermediate (100 degree) superheating for long times (up to 2-3 hours) can be the main reasons for such observations in this research. For example, Bian [2000] by using X-ray diffraction showed the existence of medium-range order of composition $\text{Al}_{13}\text{Fe}_4$ in Al-1wt% Fe alloy at 700°C . This medium-range order disappears by increasing the temperature to 1400°C and as a result Bian *et.al* observed two different morphologies (flake-like and dendrite-like) of $\text{Al}_{13}\text{Fe}_4$ by changing the amount of superheat from 700°C to 1400°C .

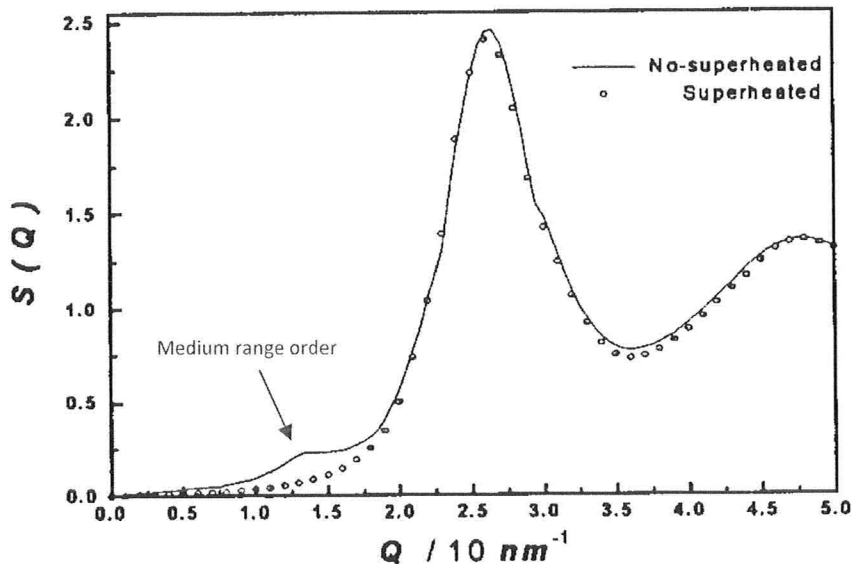


Figure 3-6 Structure factor $S(Q)$ of non-superheated and superheated an aluminum alloy with 1 wt% Fe showing the medium range order of composition $Al_{13}Fe_4$ in non-superheated sample. $Q=4\pi \sin \theta/\lambda$ (λ =wavelength of diffraction beam, 2θ =scattering angle) [Bian 2000]

3.4 The theory of driving forces for onset of nucleation

It is a general agreement that by increasing the cooling rate a greater supercooling (supersaturation) can be achieved in the melt [Purdy 2004] and as a result, changes in the solidification paths may occur. In other words, different cooling rates can impose different states from which solidification commences.

The variation of temperature during casting in a mould is schematically shown in Figure 3-7.

Amount of the undercooling (ΔT) can be affected by different factors such as:

1. Efficiency of a cooler (heat transfer coefficient)
2. Concentration and potency of sites for heterogeneous nucleation in the volume of the melt

3. Surface density and strength of sites for heterogeneous nucleation at the cooler/melt contact

4. Nature of precipitating phase

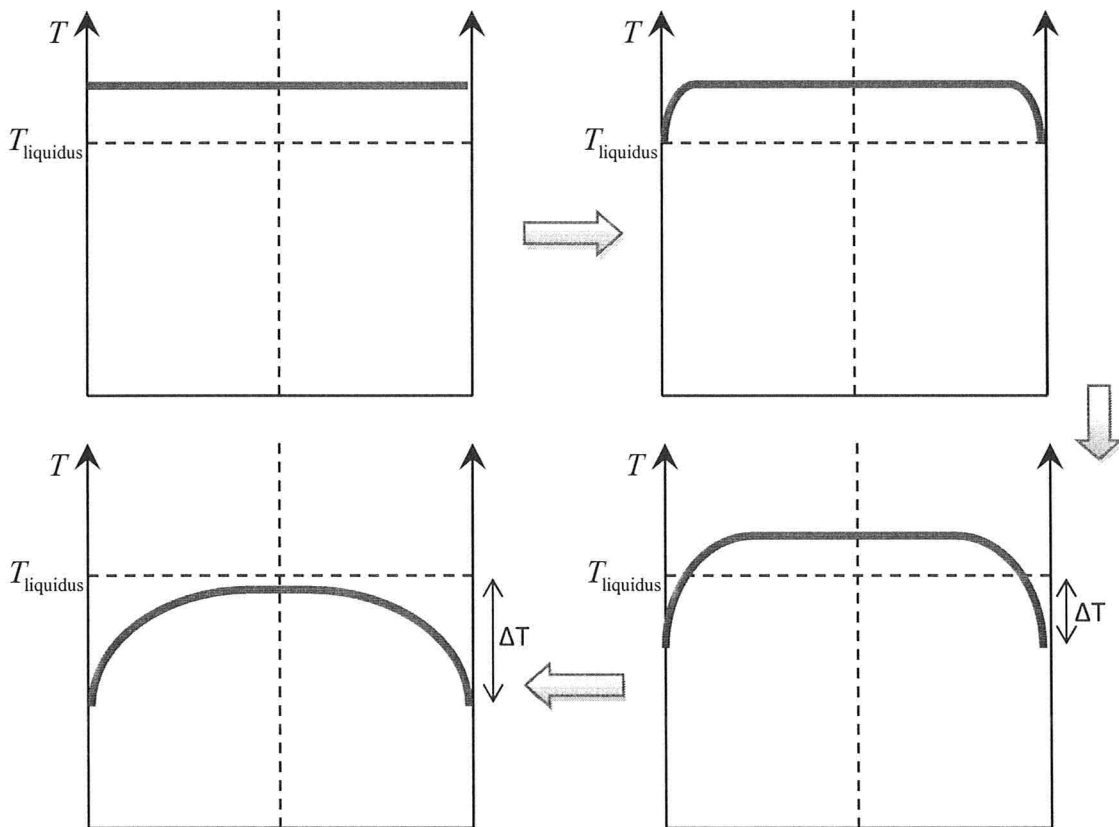


Figure 3-7 Schematic of temperature profile development in a melt during casting

Among all these parameters, heterogeneous nucleation and existence of different nucleation sites (e.g. impurities) inside the melt are recognized as the most influential factors preventing the melt from achieving to a high degree (e.g. 50 °C) of undercoolings (e.g. with respect to melting temperature of FCC phase in aluminum alloys).

In the case of aluminum alloys the situation is rather unclear. Though in some simulations [Clyne 1984] and experimental [Takeshita 1986] results it is shown that very high degrees of undercooling are attainable in aluminum alloys, among different scientific communities dealing with aluminum alloys, it is believed that due to special properties of the α -Al (FCC), which will be explained latter in this chapter, amount of undercooling never exceeds more than 3-4 °C.

For example in one case, a simulation of temperature profiles in the melt-spun aluminum alloys by Clyne [1984] showed that in rapid solidification methods such as melt-spinner, high degrees of undercooling (more than 100 °C), in respect with liquidus line, are achievable. In another case, Takeshita *et.al* [1986] experimentally showed that the undercoolings attainable by the rapid quenching of Al-Cu eutectic alloy (Al-17.3 at% Cu) under different cooling conditions can even reach 170 °K which is in great contrast with the general believe in the scientific communities about aluminum alloys.

Considering the above circumstances regarding the attainable degree of the undercooling (ΔT) in aluminum alloys, two different approaches can be assumed for the person who is dealing with solidification of aluminum alloys.

1. In the first approach, one can assume that high degrees of supercooling (e.g. 100 °C) are achievable before onset of nucleation

2. In the second approach, nucleation of solid phases starts immediately below liquidus line, and as a result amount of supercooling is negligible.

Accordingly, in line with one of the project objectives for investigating the applicability of concept of driving forces for onset of nucleation for predicting the as cast microstructure in aluminum alloys, two scenarios are investigated:

3.4.1 Scenario number one: FCC phase is not allowed to precipitate (Global Undercooling)

In the first approach, one can assume that in the early stages of the rapid solidification and depending on the casting conditions (amount of superheat, rate of heat extraction, size of the melt and etc.), a temperature profile with a significant degree of supercooling in the whole or portion of the melt can be generated. In other word, a substantial “pre-nucleation supercooling” occurs in the melt. Let us emphasize that this condition is not attainable unless no nucleation occurs in the melt.

In this situation, one may try to apply the concept of the driving forces for the onset of precipitation for explaining the experimental observations. It can be done by calculating driving forces for all solid phases for a given supercooling.

In fact, depending upon the alloy composition and the degree of supercooling, different phases will have different driving forces for onset of precipitation. Considering the phase with highest value of this property as a winner in the nucleation competition, one can try to predict the experimental results.

Figure 3-8 shows the results of such calculation for A1-Fe.3-Si.05, A2-Fe.3-Si.15, A3-Fe.3-Si.45 and A4-Fe.5-Si.2 carried out by using version "S" of Thermo-Calc software. The calculation of driving forces were performed by using "COST-507" database and preventing of all phases (except liquid) from participating in the equilibrium reactions i.e. no solid phase was allowed to precipitate. The computational aspects are elaborated in the paper by Purdy *et.al* [2004]. It is worth emphasizing that thermodynamic properties of many metastable phases such as Al_9Fe_2 , Al_mFe , Al_xFe , q_1 , q_2 , different types of α -AlFeSi and β -AlFeSi, either are not included or are not available to be included in this database. Newer and more complete versions of aluminum databases such as "COST2" or "TTAL6 V6.1" are available, but, even in these new databases thermodynamic properties of all phases are not included. This lack of information is crucially important and can introduce a great deficit for clarity and generality of computations.

Results of these calculations show that for initiation of precipitation of intermetallic phases, a great degree of supercooling is required. For example, temperature should be at least around 500-550°C for precipitations of $Al_{13}Fe_4$ and Al_6Fe . This value decreases to around 400-450 °C for β -AlFeSi.

Even if it is assumed that such amounts of supercoolings are achievable in these alloying system, $Al_{13}Fe_4$ is always the phase which is most likely to precipitate from i.e. other intermetallics never find a chance to precipitate.

This great incongruity with the experimental results makes one to conclude that this kind of calculations probably can not be used for the prediction of phase portrait in as cast aluminum alloys.

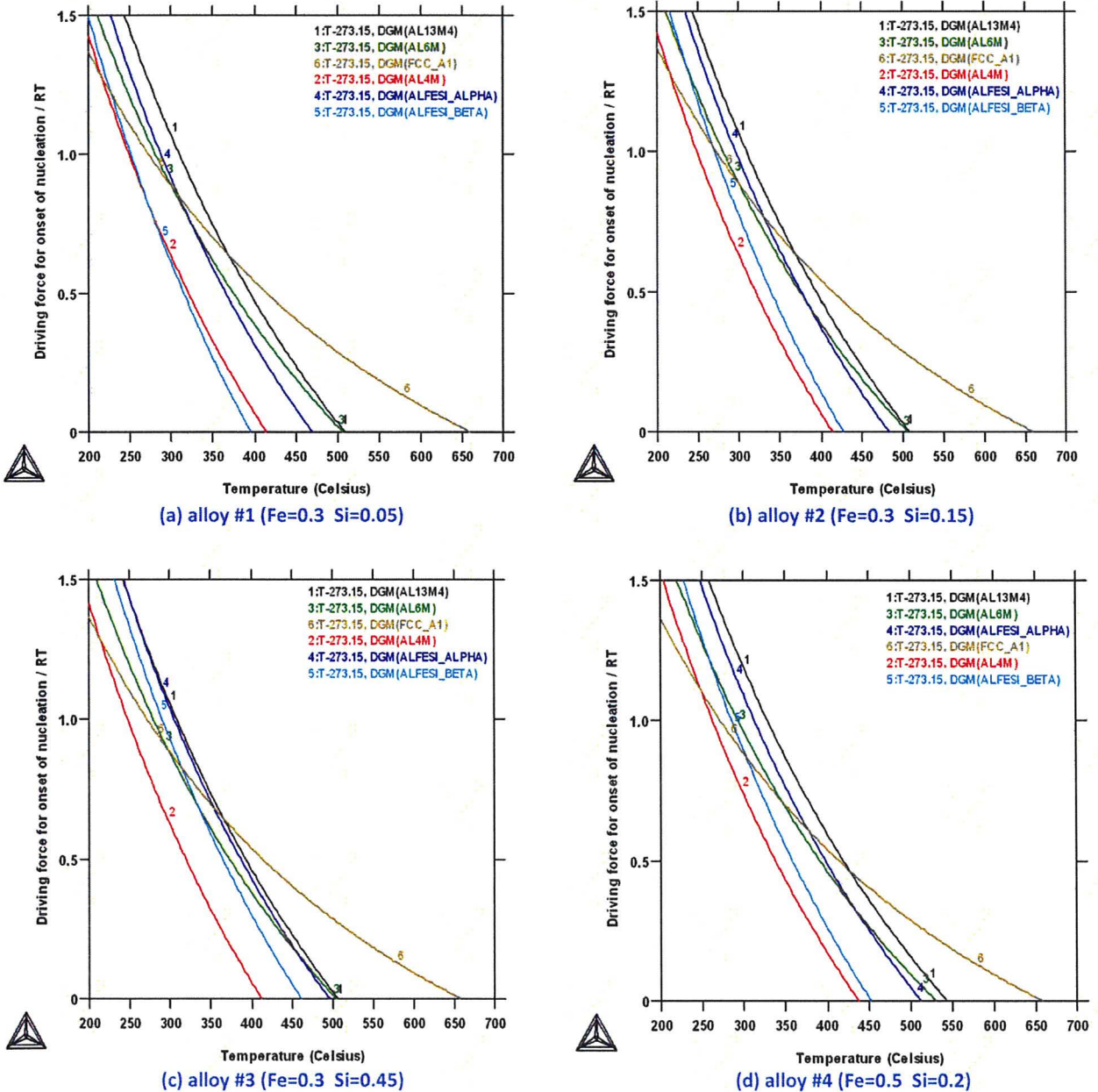


Figure 3-8 Driving forces for onset of precipitation when none of the phases (except liquid) are participating in the equilibrium

Also, it is worth mentioning that in the case of a severe supercooling of the melt (hundreds of degrees), the predictions from the driving force concept are questionable, because a long-range diffusion rather than the thermodynamic stabilities of various intermetallics may become (and likely becomes) a decisive factor. In other words, even if all thermodynamics conditions for the formation of these intermetallic phases are satisfied, in dilute aluminum alloys (e.g. Al-Fe.3-Fe.05) the formation of Fe-rich and Si-rich intermetallics still requires long range diffusion of alloying elements (Fe and Si) from different parts of the melt. Satisfaction of this condition at high degrees of supercooling can be a great obstacle which limits the formation of these intermetallics.

3.4.2 Scenario number two: FCC phase is allowed to precipitate

It is firmly established experimentally that if a composition of alloy corresponds to the primary FCC field (the case of wrought Al alloys), the amount of supercooling never exceeds a few degrees whatever the cooling rate is. This can be attributed to the following unique properties of Al-FCC phase distinguishing it from all other solid phases in the system of interest:

1. Its composition is not dramatically different from the composition of liquid which does not necessitate a long-range diffusion for its formation.
2. High thermal conductivity

3. Non-faceted solid/liquid interface makes it to grow faster in comparison with faceted phases.

As a result, one can conclude that within the primary FCC field, this phase will be always the first one to form, and that it will form at very low supercoolings.

It is proven that an analysis of slowly proceeding solidification processes can be handled within the framework of Gulliver-Scheil formalism, which assumes no diffusion in a solidified substance, no concentration gradients in a remaining liquid and a local equilibrium at the solid/liquid interface. Result of such analysis for an aluminum alloy with 0.3 wt% Fe and 0.05 wt% Si (alloy #1) is presented in Figure 3-9.

However one should be aware that this method cannot be employed for analyzing processes accompanying strip/continuous casting (CC). The reason is that in the course of CC (implemented, for instance, in twin-belt casters), an enormous rate of heat extraction leads to a deeply undercooled melt and high solidification rates.

In the second scenario, these experimentally proven facts are taken into account by allowing the primary FCC phase to solidify in the Gulliver-Scheil model. Then the driving forces for the beginning of formation of intermetallics from a remaining solute-rich liquid are computed. The result of such calculations for Scheil-Gulliver model is shown in Figure 3-10.

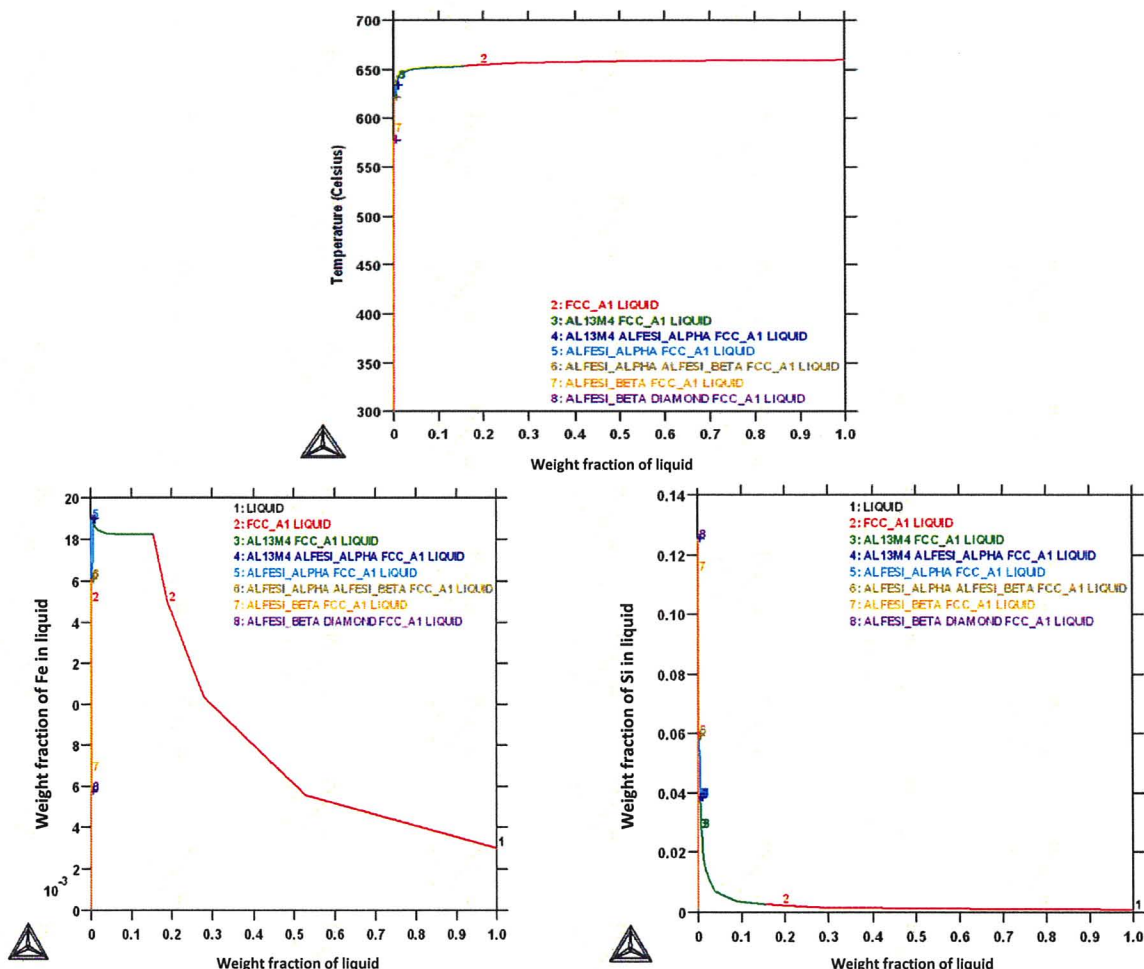


Figure 3-9 Scheil in the case when all phases are participating in the equilibrium for alloy #1 with Fe=0.3 wt% Si=0.05 wt%

Decreasing the amount of the liquid in the system is accompanied by rejection of alloying elements into interdendritic regions and as a result, as is seen Figure 3-10, the remaining liquid becomes more and more enriched with respect to Si and Fe.

In such system, computing the driving forces for onset of precipitation at different temperatures, the following graphs, shown in the Figure 3-11 to Figure 3-14, will be achieved. It is seen that the outcomes have a better conformity with experimental results as:

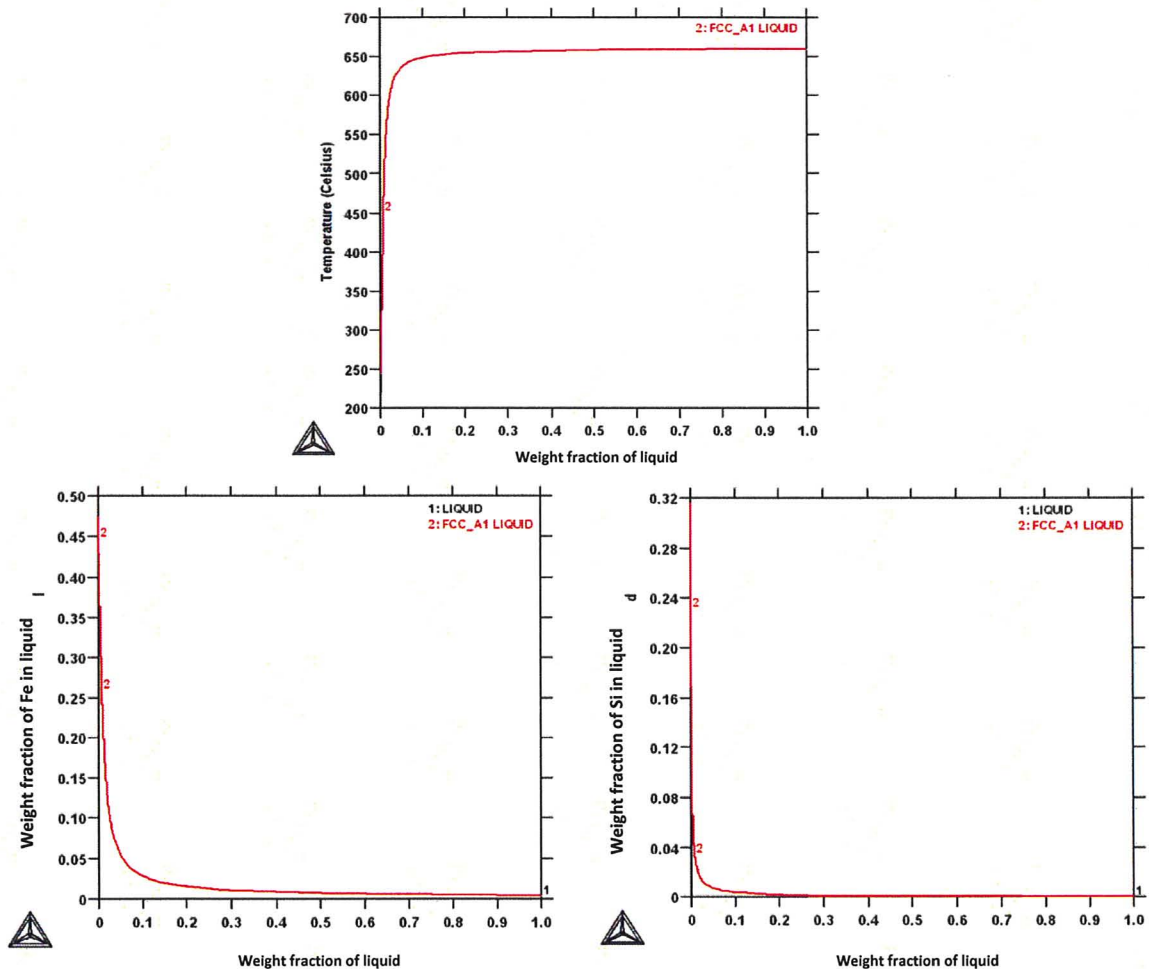


Figure 3-10 Scheil when only liquid and FCC participate in the equilibrium for alloy #1 with Fe=0.3 wt% Si=0.05 wt%

1. Amount of the required undercooling for precipitation of intermetallic phases is reasonably lower in comparison with the first scenario (global undercooling).
2. By increasing the amount of silicon, the α -AlFeSi becomes more and more likely to precipitate in such a way that in alloy #3 (Fe=0.3 Si=0.45) the α -AlFeSi has a very tight competition with $Al_{13}Fe_4$.

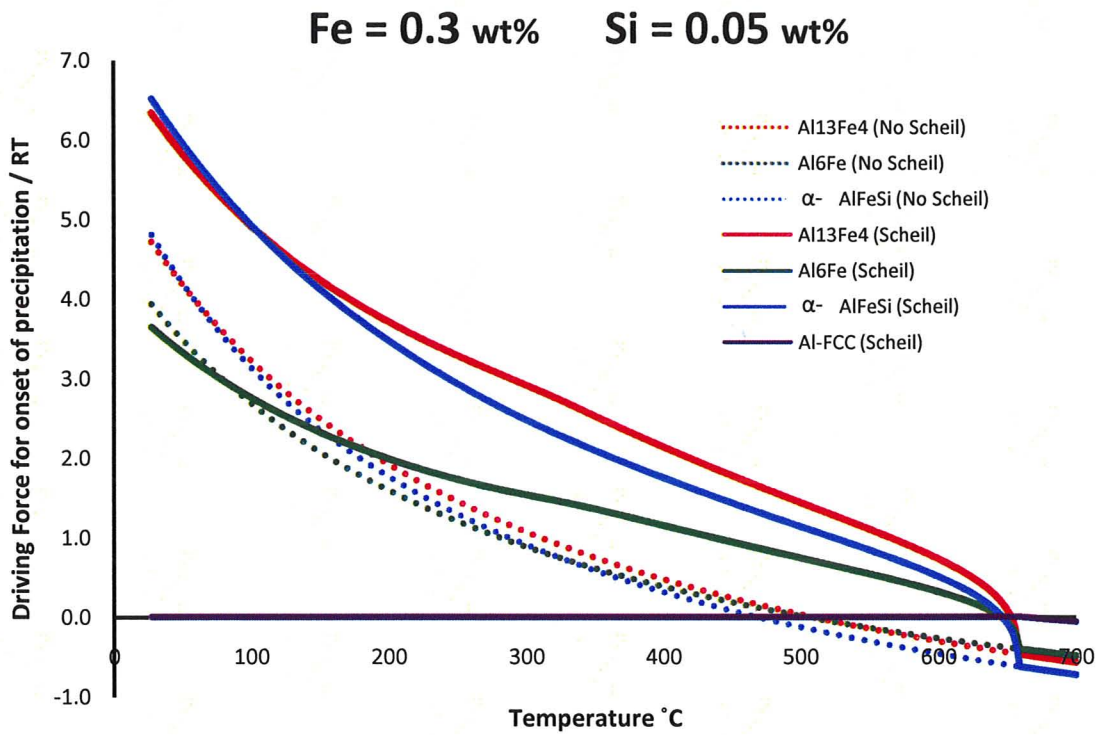


Figure 3-11 Driving forces for onset of precipitation Vs Temperature (Scheil-Gulliver model)– A1.Fe.3-Si.05

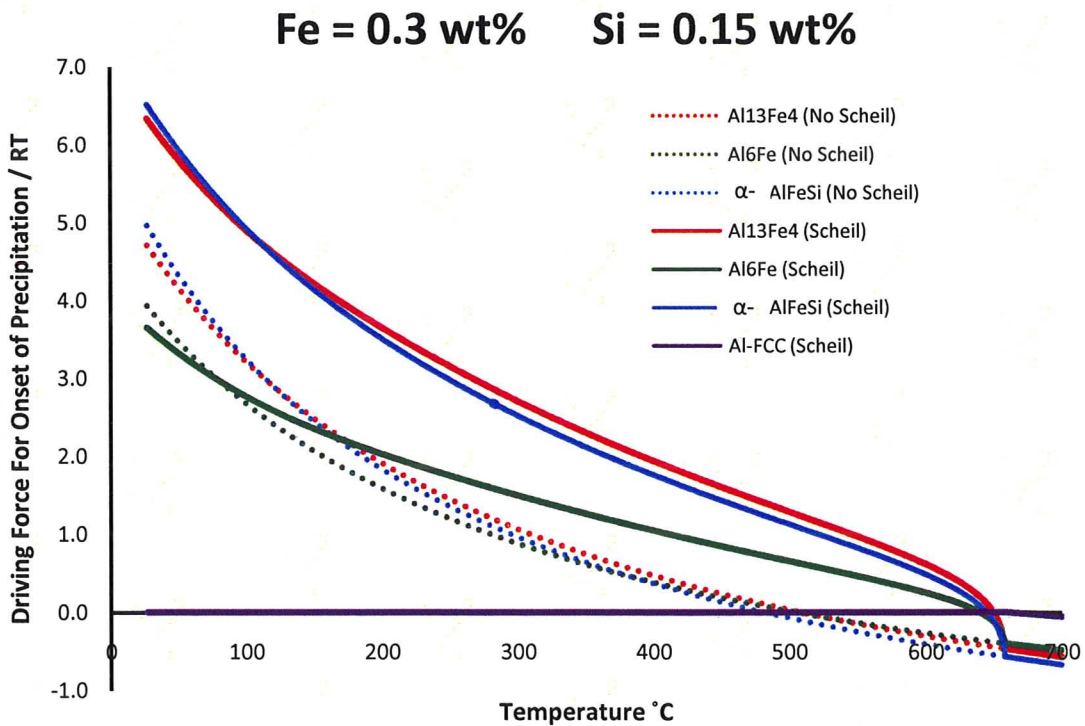


Figure 3-12 Driving forces for onset of precipitation Vs Temperature (Scheil-Gulliver model)– A2-Fe.3-Si.15

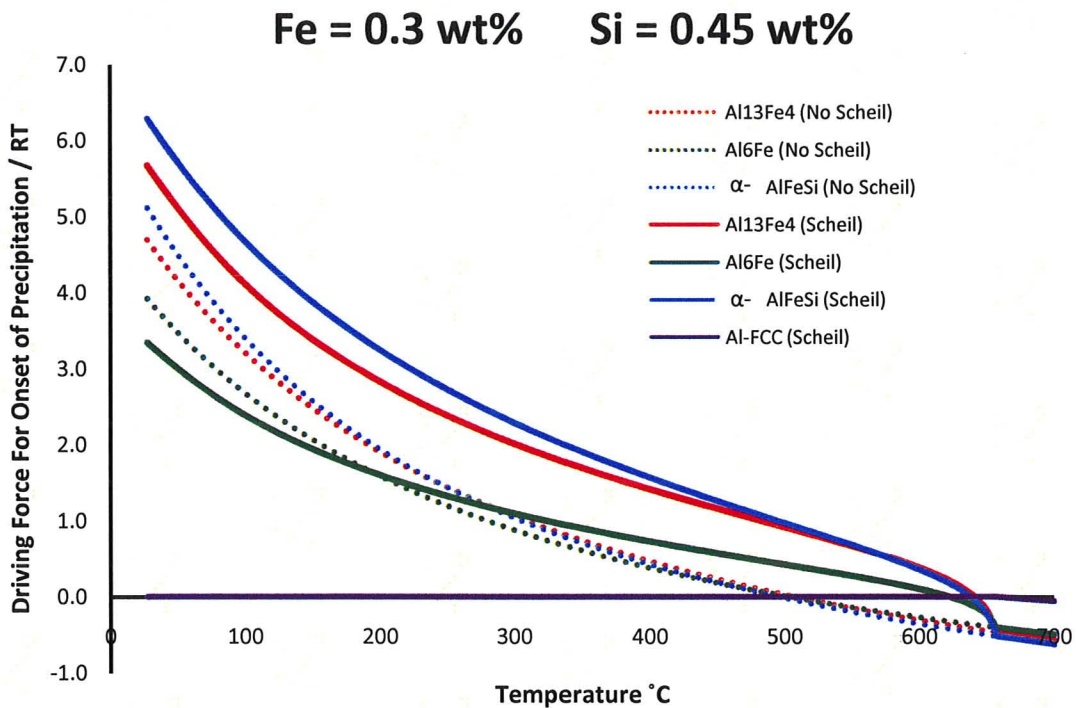


Figure 3-13 Driving forces for onset of precipitation Vs Temperature (Scheil-Gulliver model)– A3-Fe.3-Si.45

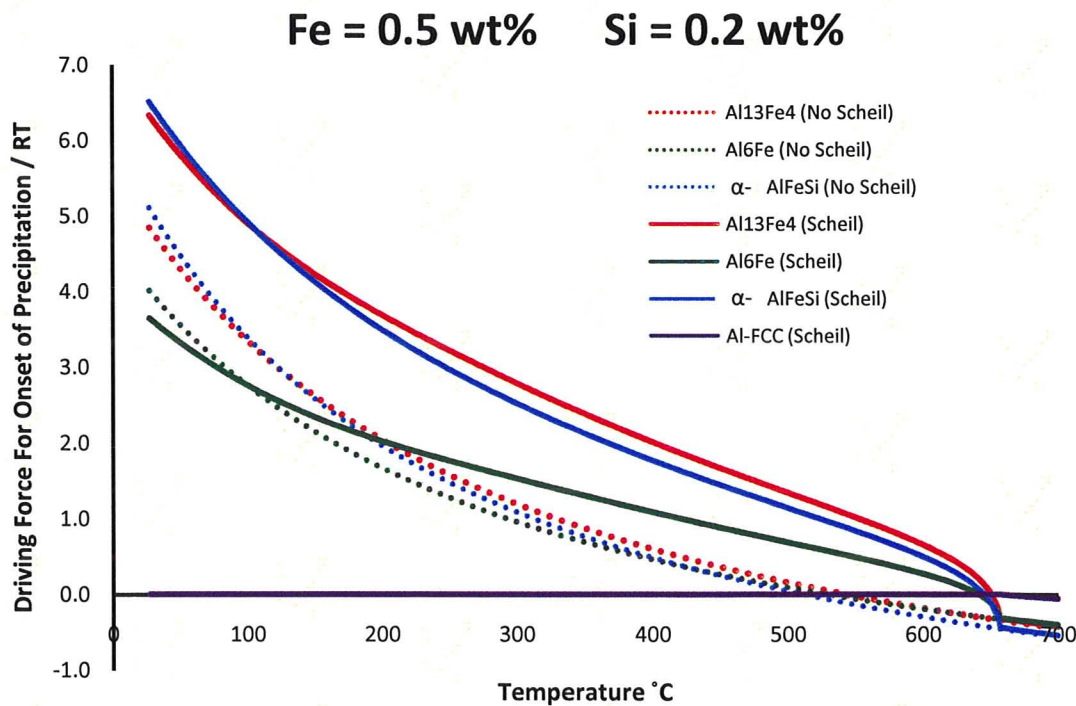


Figure 3-14 Driving forces for onset of precipitation Vs Temperature (Scheil-Gulliver model) – A4-Fe.5-Si.2

It is worth noticing that:

In all these cases, differences between computed values for α -AlFeSi and $\text{Al}_{13}\text{Fe}_4$ are not huge i.e. small changes in the thermodynamic properties of these phases, may completely change the situation in favor of the formation of α -AlFeSi. Let us recall that, there are different types of α -AlFeSi reported in the literature whose thermodynamic properties are not completely clear to be introduced in the databases.

4 Conclusions

The results obtained from both experiments and theories in the present investigation, can be summarized as following

1. Stable intermetallic, $\text{Al}_{13}\text{Fe}_4$, forms only at very low cooling rates.
2. By increasing both silicon content and cooling rate, formation of $\alpha\text{-AlFeSi}$ is promoted.
3. Fe-rich binary metastable intermetallics are stabilized by increasing iron content.
4. It seems that the concept of the driving forces for the beginning of precipitation from the liquid phase during rapid solidification provides a sensible conformity with the experimental findings.
5. At the moment, the concept provides a semi-quantitative prediction of the nature and sequence of phases precipitating during casting. A greater deal of accuracy and reliability of the model can be attained if the surface energies are taken into account.
6. A complete database in which the Gibbs energies of all metastable phases are included is needed. It is likely that first-principle calculations should be employed, because of a virtual impossibility to accumulate an amount of such phases (not in a mixture with other intermetallics) suitable for a calorimetric investigation.
7. In the case of a severe supercooling of the melt (hundreds of degrees), the predictions from the driving force concept are questionable, because a long-range

diffusion rather than the thermodynamic stabilities of various intermetallics may become (and likely becomes) a decisive factor.

For future works it seems that other features of non-equilibrium solidification, like competitive growth and suppression of solidification reactions, should be considered for complete comprehension of phase formation during solidification.

Appendix #1: ICP results

Table 1 ICP results for alloy #1 (Si=0.05 wt% Fe=0.3 wt%)

Element	Location #1	Location #2	Location #3	Location #4	Average
	Top of the ingot	Top of the ingot	Bottom of the ingot	Bottom of the ingot	
Si wt%	0.047	0.043	0.049	0.047	0.046 ± 0.003
Fe wt%	0.287	0.274	0.295	0.284	0.285 ± 0.010

Table 2 ICP results for alloy #2 (Si=0.15 wt% Fe=0.3 wt%)

Element	Location #1	Location #2	Location #3	Location #4	Average
	Top of the ingot	Top of the ingot	Bottom of the ingot	Bottom of the ingot	
Si wt%	0.135	0.138	0.138	0.141	0.138 ± 0.003
Fe wt%	0.289	0.283	0.281	0.275	0.282 ± 0.007

Table 3 ICP results for alloy #3 (Si=0.45 wt% Fe=0.3 wt%)

Element	Location #1	Location #2	Location #3	Location #4	Average
	Top of the ingot	Top of the ingot	Bottom of the ingot	Bottom of the ingot	
Si wt%	0.469	0.457	0.459	0.426	0.452 ± 0.026
Fe wt%	0.322	0.314	0.318	0.279	0.308 ± 0.030

Table 4 ICP results for alloy #4 (Si=0.2 wt% Fe=0.5 wt%)

Element	Location #1	Location #2	Location #3	Location #4	Average
	Top of the ingot	Top of the ingot	Bottom of the ingot	Bottom of the ingot	
Si wt%	0.229	0.173	0.170	0.173	0.186 ± 0.040
Fe wt%	0.489	0.461	0.481	0.504	0.484 ± 0.020

Appendix #2: Weight fraction of the extracted particles in phenol dissolution step

Table 1 Weight percent of the extracted particles from alloy #1

	Alloy #1 (Fe= 0.3 Si = 0.05)		
	Sample (g)	Extracted Powder (g)	Weight Percent
Graphite Crucible	3.034	0.017	0.560
Copper Mould	2.722	0.011	0.404
Water-Cooled Copper Mould	3.037	0.021	0.691
Ribbon 300 μm	3.049	0.027	0.885
Ribbon 150 μm	2.766	0.021	0.759
Ribbon 50 μm	3.061	0.028	0.915

Table 2 Weight percent of the extracted particles from alloy #2

	Alloy #2 (Fe= 0.3 Si = 0.15)		
	Sample (g)	Extracted Powder (g)	Weight Percent
Graphite Crucible	3.195	0.023	0.720
Copper Mould	2.847	0.020	0.702
Water-Cooled Copper Mould	3.141	0.028	0.891
Ribbon 300 μm	3.015	0.021	0.697
Ribbon 150 μm	3.031	0.021	0.693
Ribbon 70 μm	2.890	0.020	0.692

Table 3 Weight percent of the extracted particles from alloy #3

	Alloy #3 (Fe= 0.3 Si = 0.45)		
	Sample (g)	Extracted Powder (g)	Weight Percent
Graphite Crucible	3.145	0.029	0.922
Copper Mould	3.017	0.027	0.895
Water-Cooled Copper Mould (Top of the sample)	3.180	0.029	0.912
Water-Cooled Copper Mould (contact surface)	2.682	0.023	0.858
Ribbon 300 μm	3.023	0.021	0.695
Ribbon 150 μm	3.064	0.024	0.783
Ribbon 70 μm	3.162	0.026	0.822

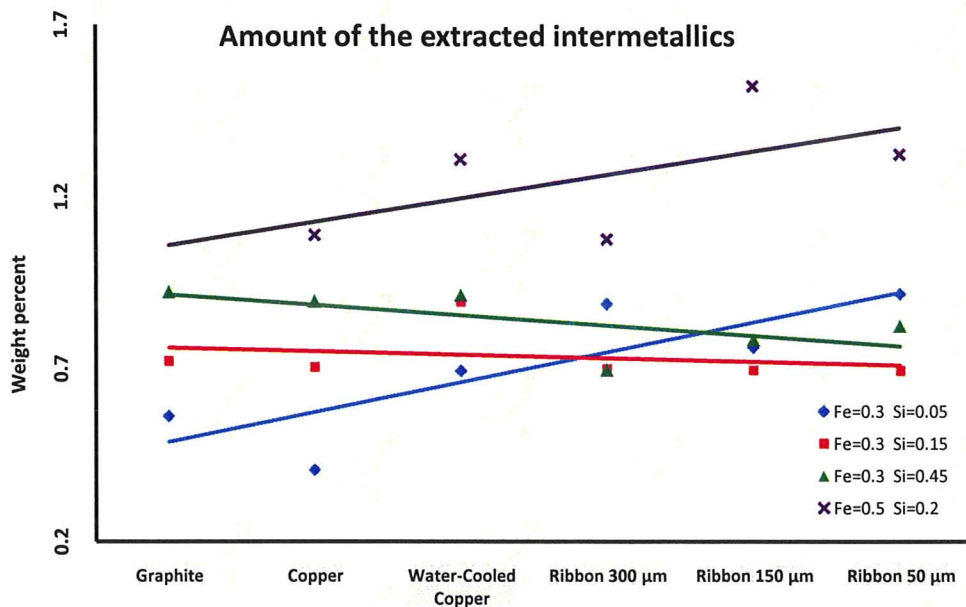
Table 4 Weight percent of the extracted particles from alloy #4

	Alloy #4 (Fe= 0.50 Si = 0.2)		
	Sample (g)	Extracted Powder (g)	Weight Percent
Graphite Crucible	-	-	-
Copper Mould	2.947	0.032	1.086
Water-Cooled Copper Mould	2.986	0.039	1.306
Ribbon 300 µm	2.888	0.031	1.073
Ribbon 150 µm	3.095	0.047	1.519
Ribbon 70 µm	2.955	0.039	1.320

Table 5 Weight percent of the extracted particles from samples casted at 1000 °C (high super heat)

	Super Heat (Casting temperature ≈ 1000 °C)		
	Sample (g)	Extracted Powder (g)	Weight Percent
Alloy #1 (Ribbon 150 µm)	2.950	0.018	0.610
Alloy #2 (Ribbon 150 µm)	2.922	0.024	0.821
Alloy #4 (Ribbon 150 µm)	2.967	0.038	1.280

The results are plotted in the following graph:



It is worth noticing that amount of error and reproducibility of these results are still questionable and more experiments are needed to confirm them.

Appendix #3: XRD patterns

XRD analyses of extracted particles were performed under the conditions tabulated below for all groups of samples.

Table 1 XRD conditions for particles extracted from alloy #1 (Fe=0.3 Si=0.05)

Sample	Range 2 θ	Step size (degree)	Dwell (s)	Anode	I (max) after background subtraction
A1.Graphite crucible	5.169/59.177	0.008	10.85	Cu	734
A1.Copper mould	5.169/59.177	0.008	10.85	Cu	396
A1.Water-cooled copper	5.169/59.177	0.008	10.85	Cu	534
A1.Ribbon Th= 300 μm	5.169/59.177	0.008	10.85	Cu	506
A1. Ribbon Th=150 μm	5.169/59.177	0.008	10.85	Cu	429
A1. Ribbon Th=70 μm	5.169/59.177	0.008	10.85	Cu	412

Table 2 XRD conditions for particles extracted from alloy #2 (Fe=0.3 Si=0.15)

Sample	Range 2 θ	Step size (degree)	Dwell (s)	Anode	I (max) after background subtraction
A2.Graphite crucible	13/65	0.017	20.05	Cu	1303
A2.Copper mould	13/65	0.017	20.05	Cu	1128
A2.Water-Cooled copper	15/65	0.017	40.7	Cu	2777
A2.Ribbon Th= 300 μm	5.169/59.177	0.008	10.85	Cu	511
A2. Ribbon Th=150 μm	5.169/59.177	0.008	10.85	Cu	392
A2. Ribbon Th=70 μm	-	-	-	-	-

Table 3 XRD conditions for particles extracted from alloy #3 (Fe=0.30 Si=0.45)

Sample	Range 2 θ	Step size (degree)	Dwell (s)	Anode	I (max) after background subtraction
A3.Graphite crucible	13/65	0.017	20.05	Cu	1953
A3.Copper mould	13/65	0.017	20.05	Cu	1584
A3.Water-cooled copper (Top of the sample)	13/65	0.017	20.05	Cu	1576
A3.Water-cooled copper (contact surface)	13/65	0.017	20.05	Cu	1874
A3.Ribbon Th= 300 μm	13/65	0.017	20.05	Cu	1369
A3. Ribbon Th=150 μm	15/65	0.017	40.7	Cu	1656
A3. Ribbon Th=70 μm	15/65	0.017	101.4	Cu	1697

Table 4 XRD conditions for particles extracted from alloy #4 (Fe=0.50 Si=0.2)

Sample	Range 2θ	Step size (degree)	Dwell (s)	Anode	I (max) after background subtraction
A4.Graphite crucible	15/65	0.013	20.7	Cu	1555
A4.Copper mould	15/65	0.013	20.7	Cu	1016
A4.Water-cooled copper	15/65	0.013	20.7	Cu	1584
A4.Ribbon Th= 300 μm	18/48	0.017	60.75	Cu	1785
A4. Ribbon Th=150 μm	15/65	0.013	20.7	Cu	955
A4. Ribbon Th=70 μm	18/48	0.017	60.75	Cu	960

Table 5 XRD conditions for samples produced with high amount of super heat (Casting temperature = 1000 °C)

Sample	Range 2θ	Step size (degree)	Dwell (s)	Anode	I (max) after background subtraction
A1. Ribbon Th=150 μm	18/48	0.017	60.75	Cu	1133
A2 .Ribbon Th=150 μm	18/48	0.017	60.75	Cu	1153
A3 .Ribbon Th=150 μm	15/65	0.013	20.7	Cu	379
A4 .Ribbon Th=150 μm	18/48	0.017	60.75	Cu	1107

The obtained XRD profiles for all samples are presented below. In the following profiles some peaks of the identified phases have selectively been marked by using different shapes and colors.

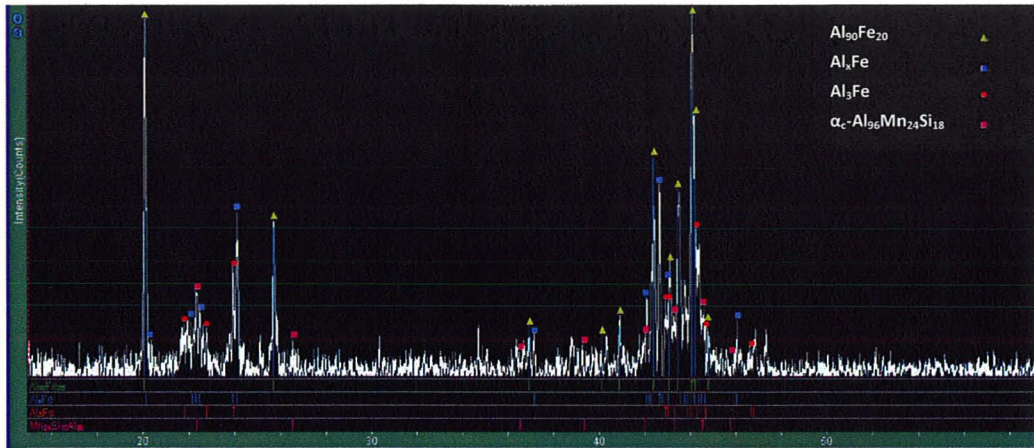


Figure 1 XRD result of alloy #1 (Fe=0.3 Si=0.05), Graphite Crucible

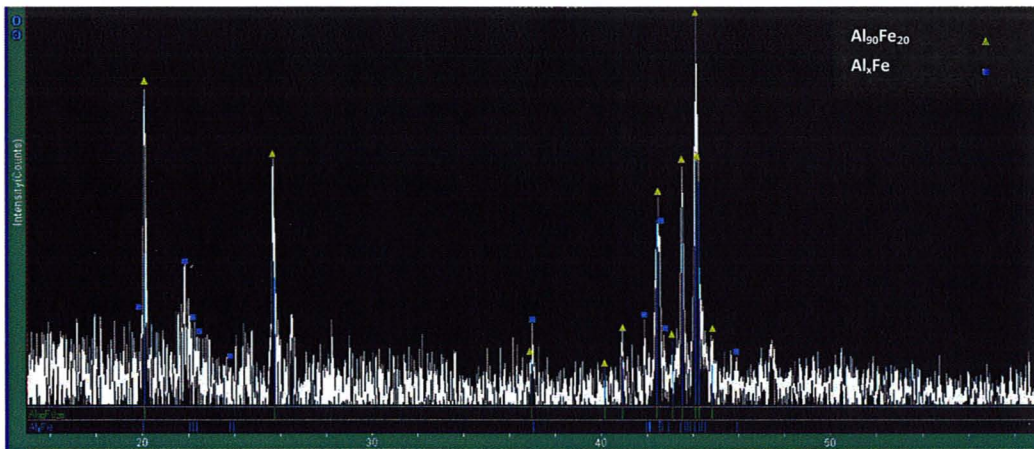


Figure 2 XRD result of alloy #1 (Fe=0.3 Si=0.05), Copper Mould

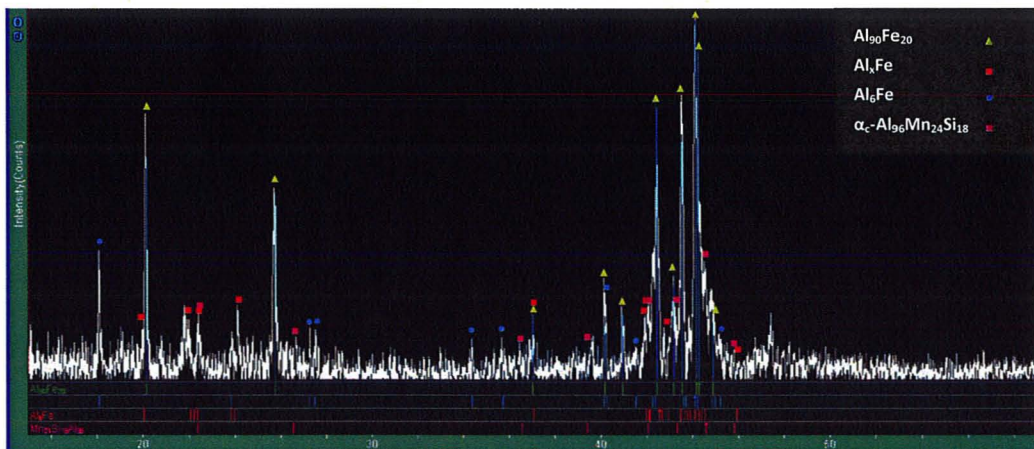


Figure 3 XRD result of alloy #1 (Fe=0.3 Si=0.05), Water-Cooled Copper Mould

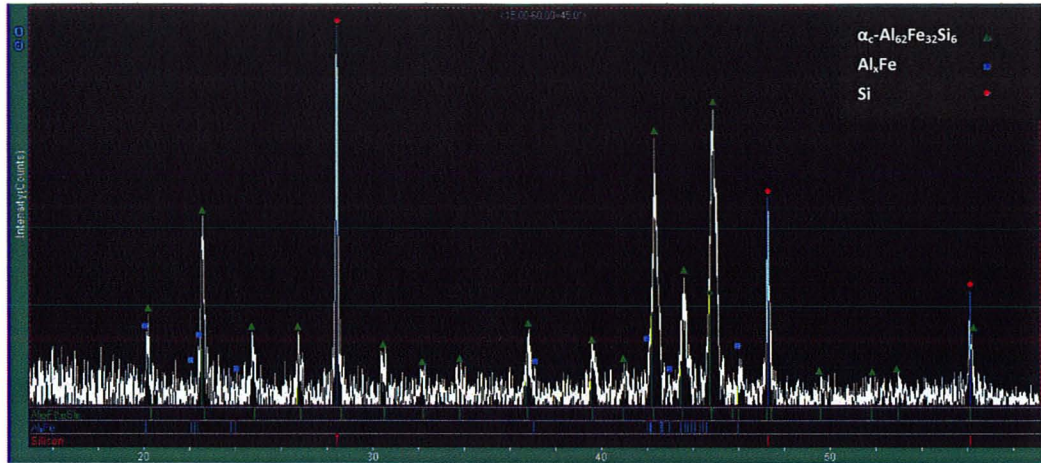


Figure 4 XRD result of alloy #1 (Fe=0.3 Si=0.05), Melt Spinner, Ribbon Thickness = 300 μm

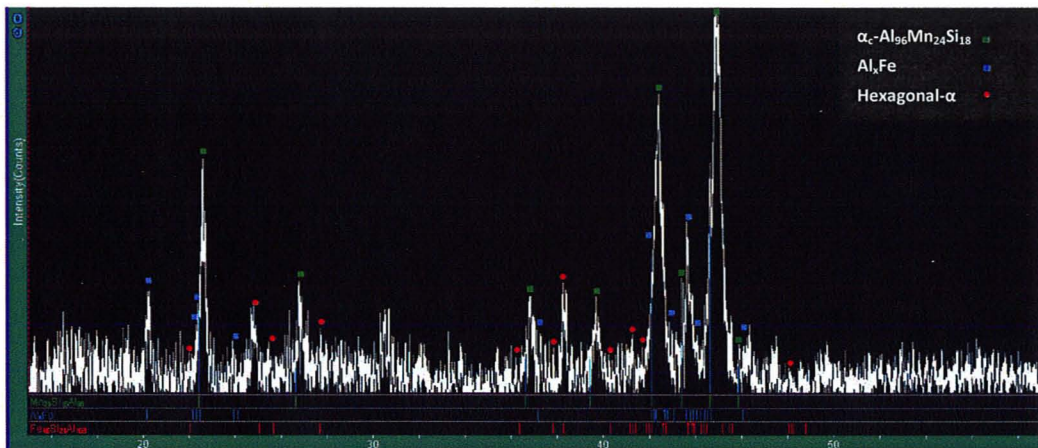


Figure 5 XRD result of alloy #1 (Fe=0.3 Si=0.05), Melt Spinner, Ribbon Thickness = 150 μm

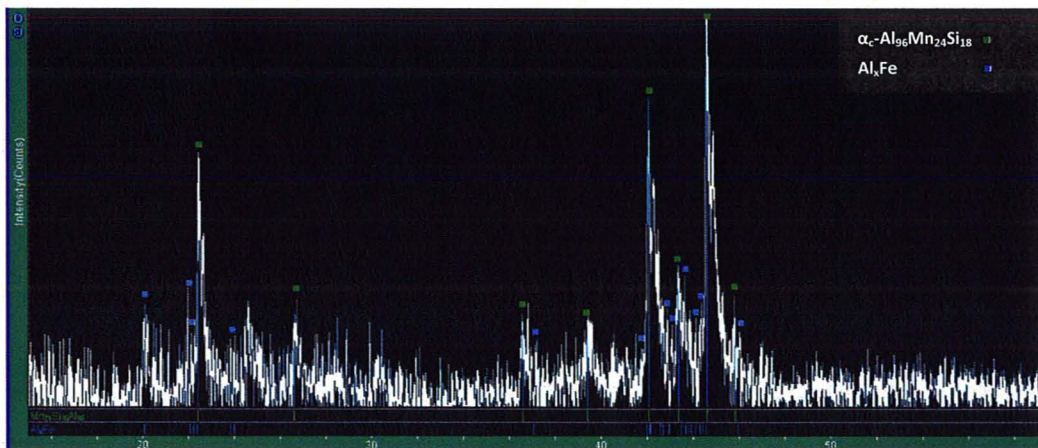


Figure 6 XRD result of alloy #1 (Fe=0.3 Si=0.05), Melt Spinner, Ribbon Thickness = 70 μm

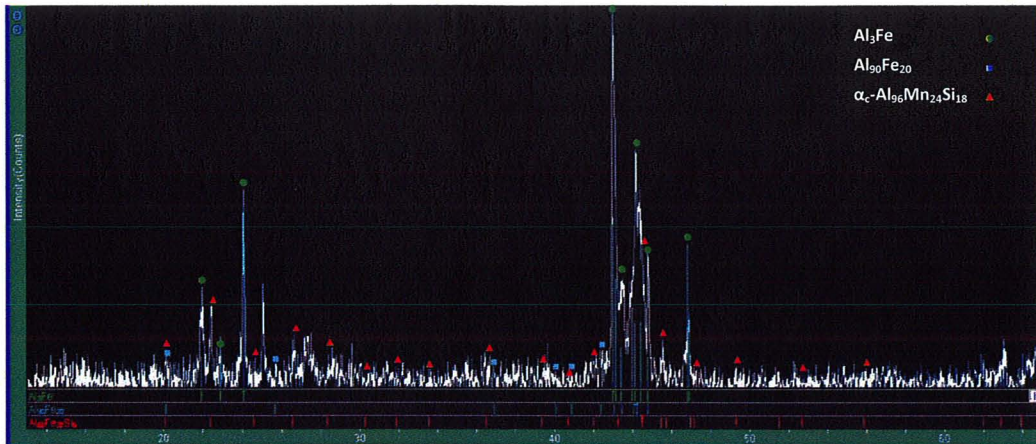


Figure 7 XRD result of alloy #2 (Fe=0.3 Si=0.15), Graphite Crucible

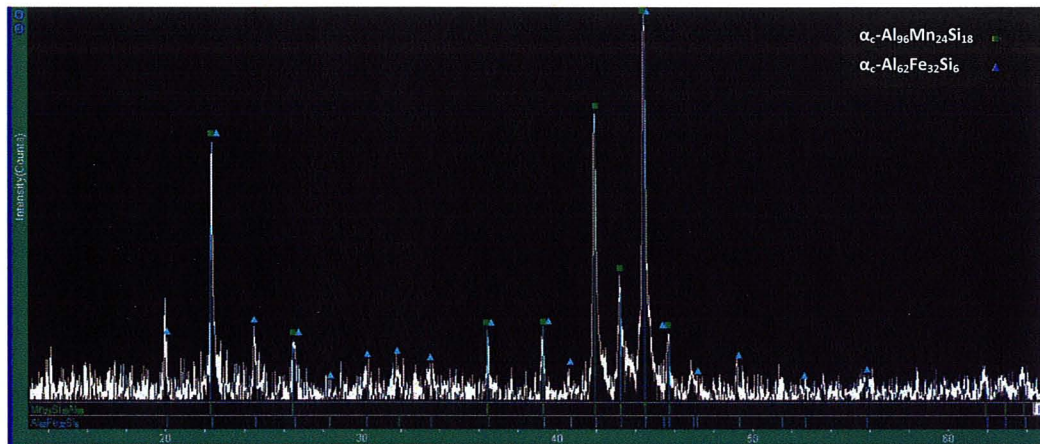


Figure 8 XRD result of alloy #2 (Fe=0.3 Si=0.15), Copper Mould

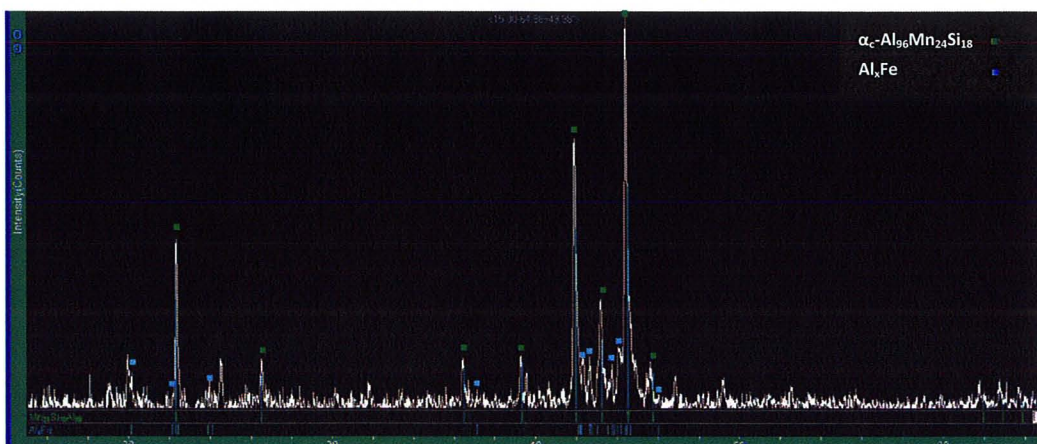


Figure 9 XRD result of alloy #2 (Fe=0.3 Si=0.15), Water-Cooled Copper Mould

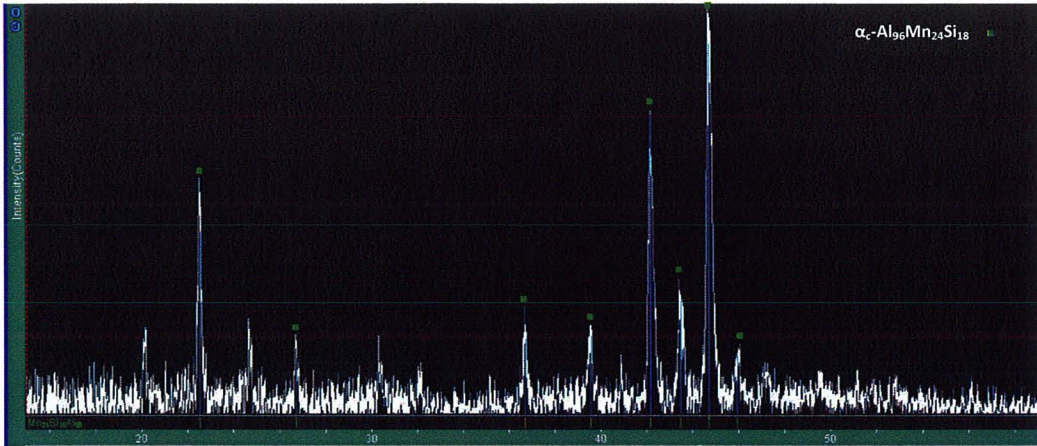


Figure 10 XRD result of alloy #2 (Fe=0.3 Si=0.15), Melt Spinner, Ribbon Thickness = 300 μm

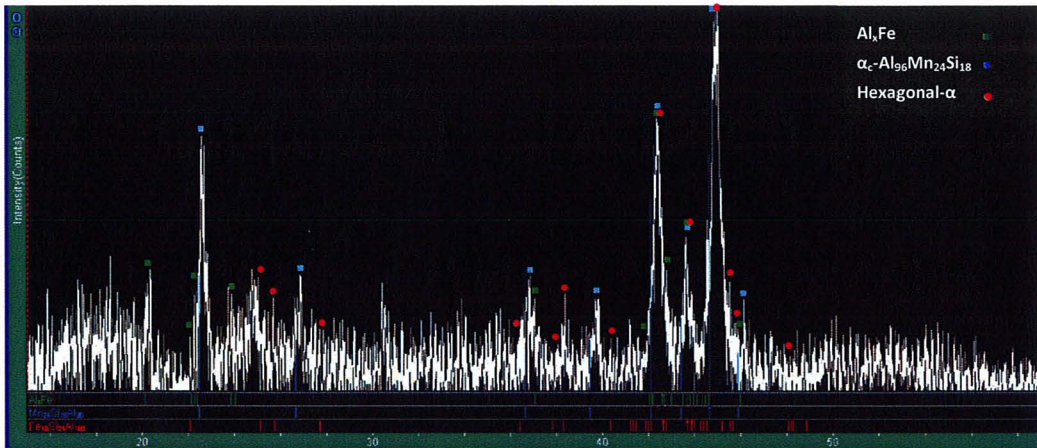


Figure 11 XRD result of alloy #2 (Fe=0.3 Si=0.15), Melt Spinner, Ribbon Thickness = 150 μm

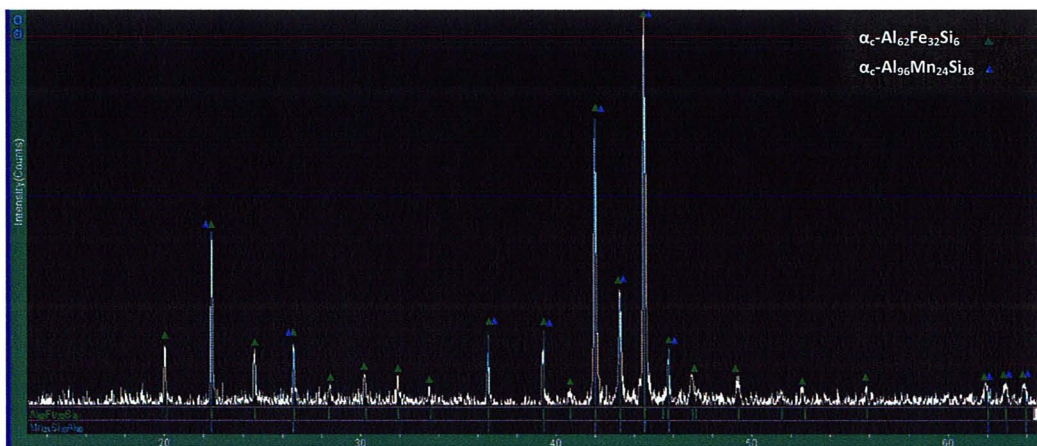


Figure 12 XRD result of alloy #3 (Fe=0.3 Si=0.45), Graphite Crucible

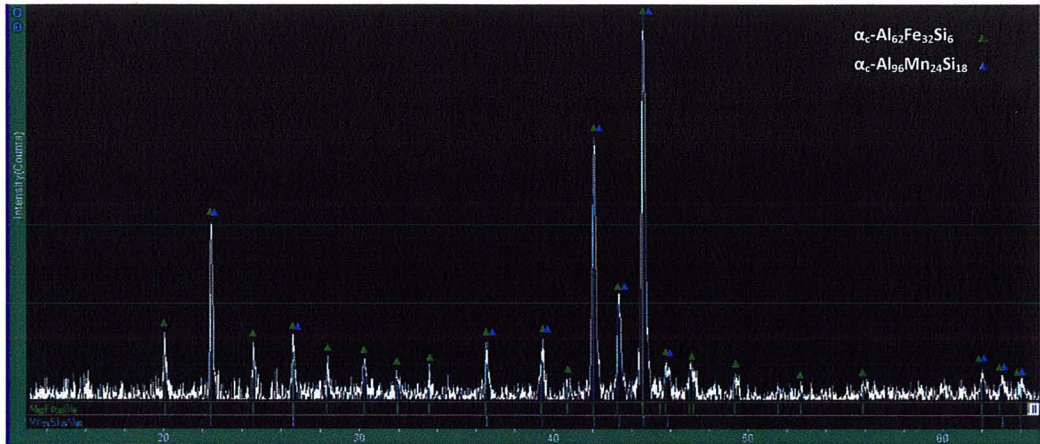


Figure 13 XRD result of alloy #3 (Fe=0.3 Si=0.45), Copper Mould

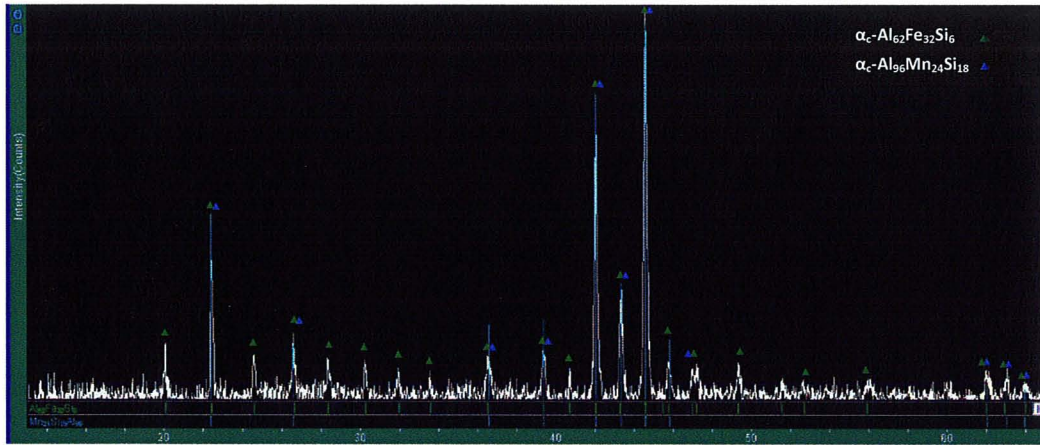


Figure 14 XRD result of alloy #3 (Fe=0.3 Si=0.45), Water-Cooled Copper Mould, TOP OF THE SAMPLE

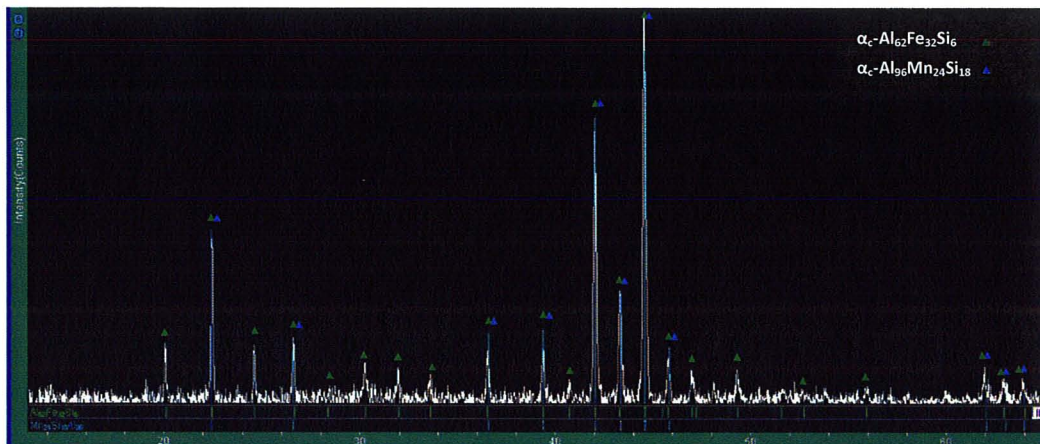


Figure 15 XRD result of alloy #3 (Fe=0.3 Si=0.45), Water-Cooled Copper Mould, CONTACT SURFACE

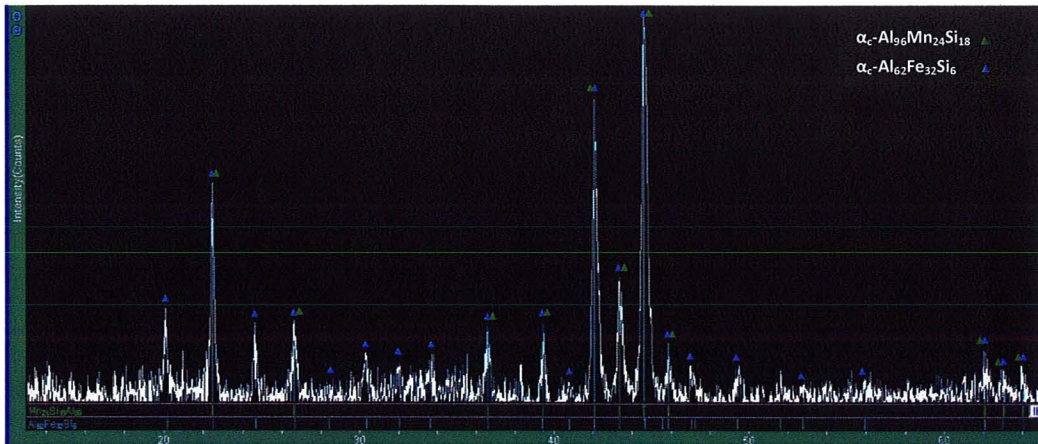


Figure 16 XRD result of alloy #3 (Fe=0.3 Si=0.45), Melt Spinner, Ribbon Thickness = 300 μm

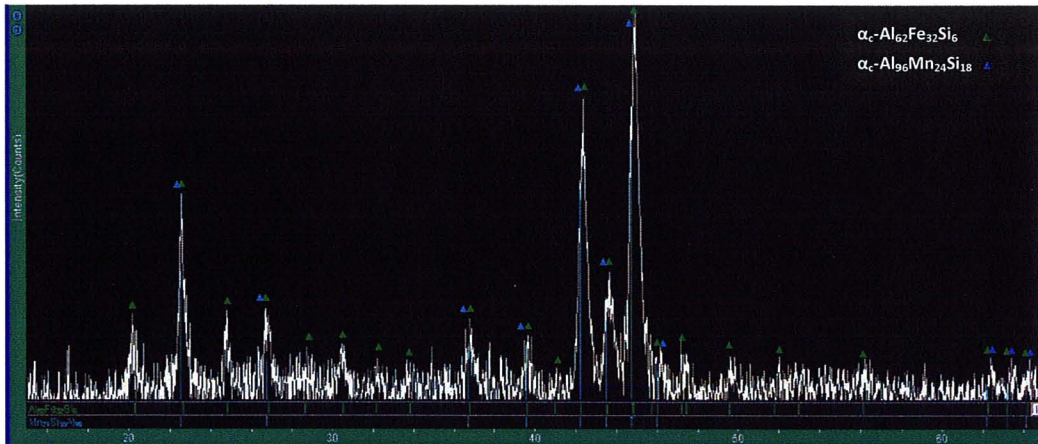


Figure 17 XRD result of alloy #3 (Fe=0.3 Si=0.45), Melt Spinner, Ribbon Thickness = 150 μm

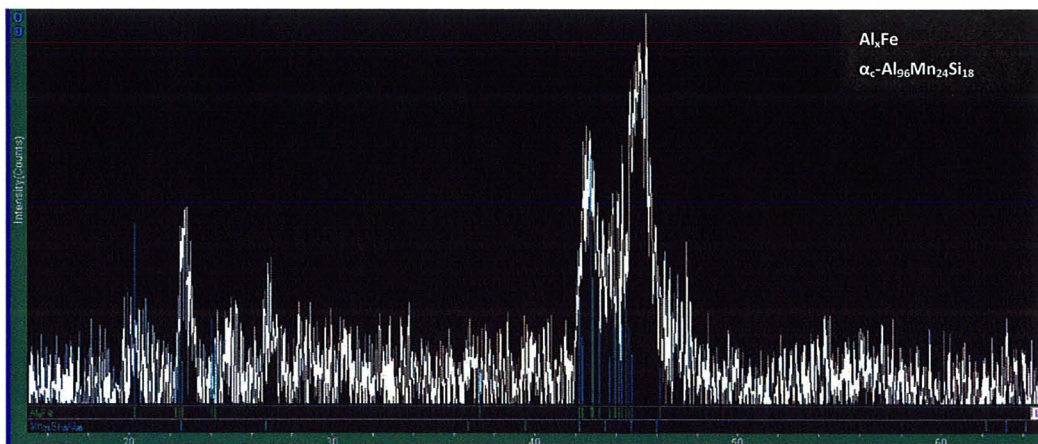


Figure 18 XRD result of alloy #3 (Fe=0.3 Si=0.45), Melt Spinner, Ribbon Thickness = 70 μm

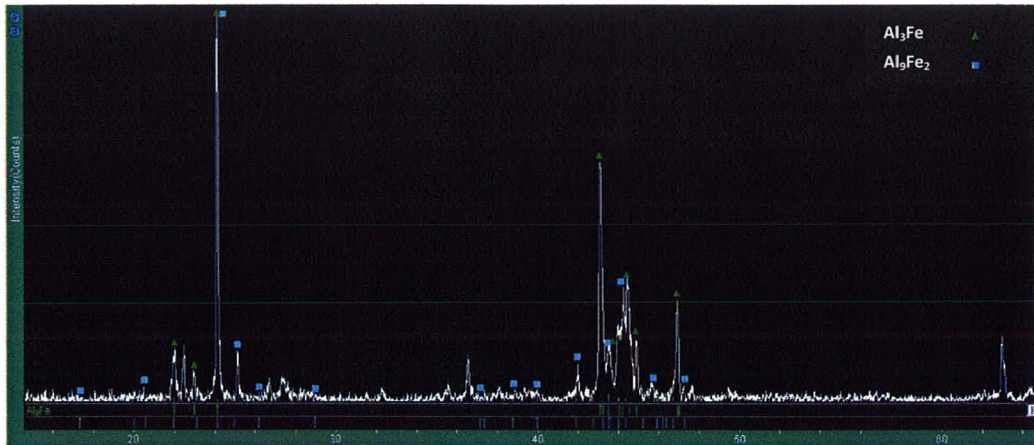


Figure 19 XRD result of alloy #4 (Fe=0.5 Si=0.2), Graphite Crucible

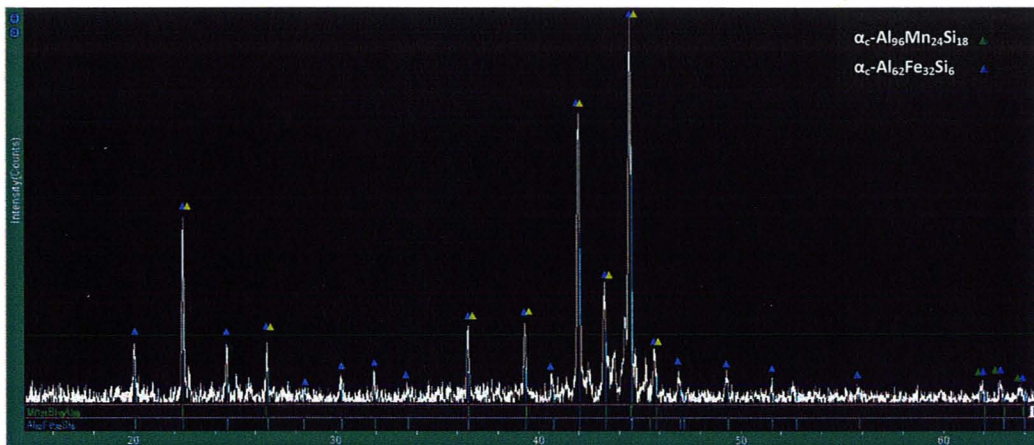


Figure 20 XRD result of alloy #4 (Fe=0.5 Si=0.2), Copper Mould

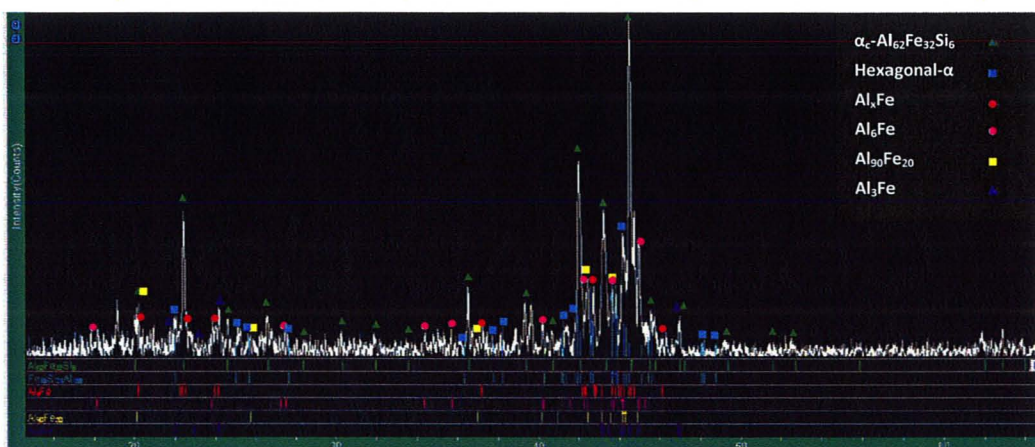


Figure 21 XRD result of alloy #4 (Fe=0.5 Si=0.2), Water-Cooled Copper Mould

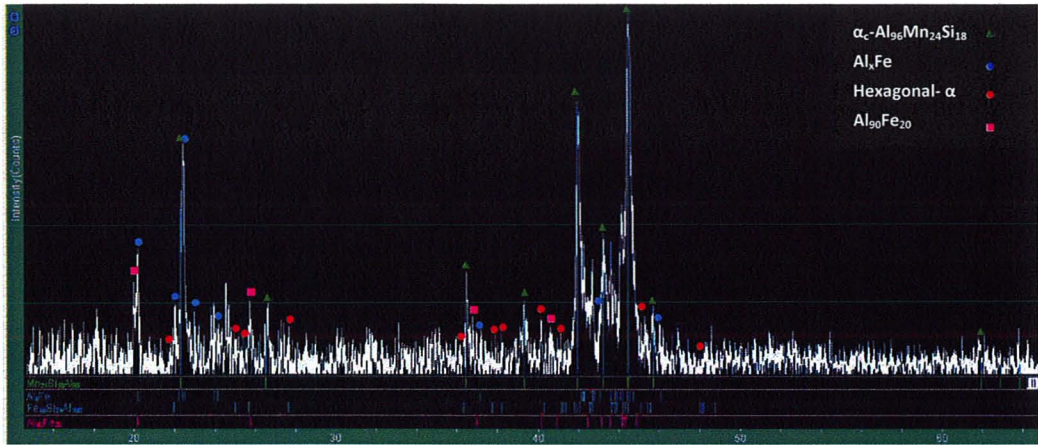


Figure 22 XRD result of alloy #4 (Fe=0.5 Si=0.2), Melt Spinner, Ribbon Thickness = 300 μm

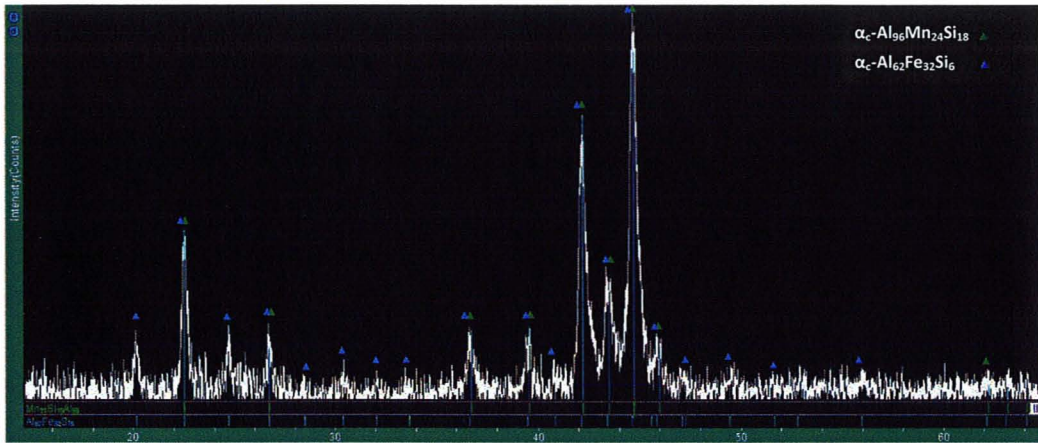


Figure 23 XRD result of alloy #4 (Fe=0.5 Si=0.2), Melt Spinner, Ribbon Thickness = 150 μm

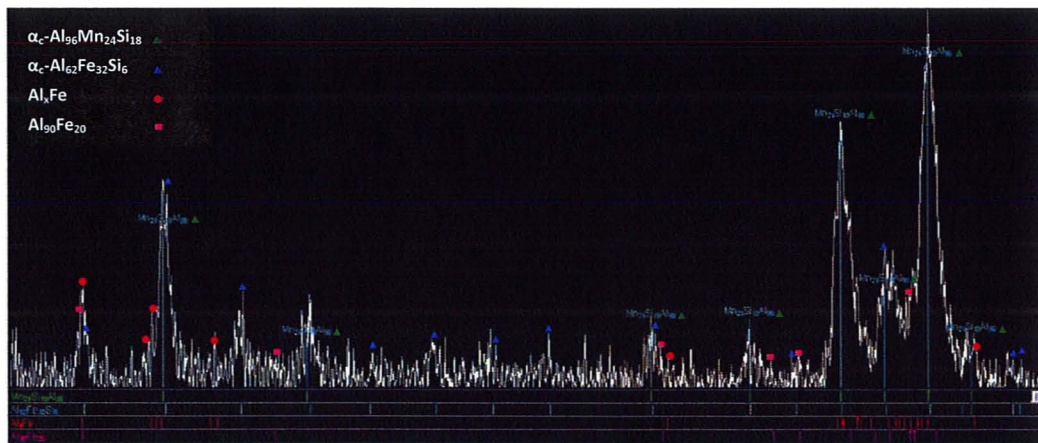


Figure 24 XRD result of alloy #4 (Fe=0.5 Si=0.2), Melt Spinner, Ribbon Thickness = 70 μm

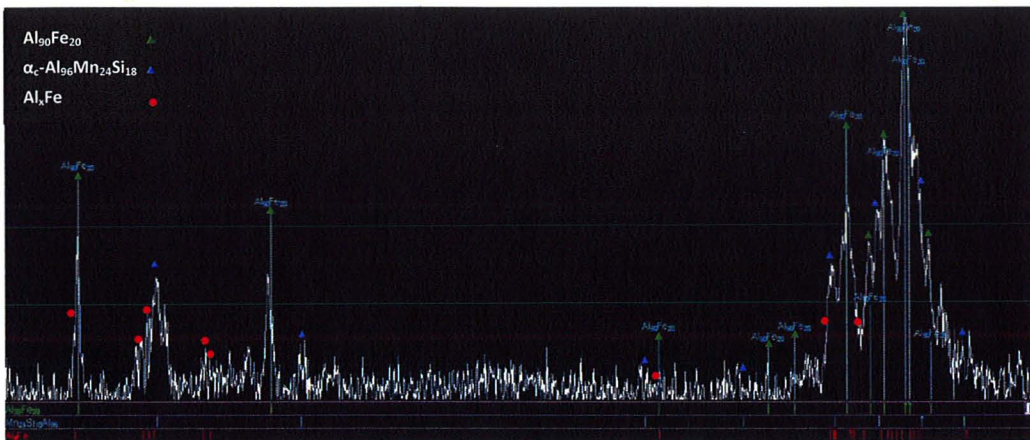


Figure 25 XRD result of alloy #1 (Fe=0.3 Si=0.05), Melt Spinner, Thickness = 150 μm , SUPER HEAT $\geq 1000^\circ C$

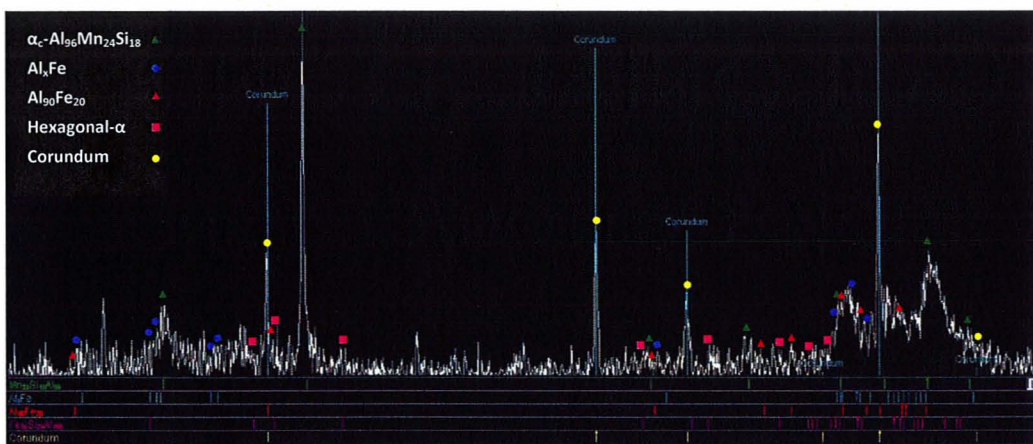


Figure 26 XRD result of alloy #2 (Fe=0.3 Si=0.15), Melt Spinner, Thickness = 150 μm , SUPER HEAT $\geq 1000^\circ C$

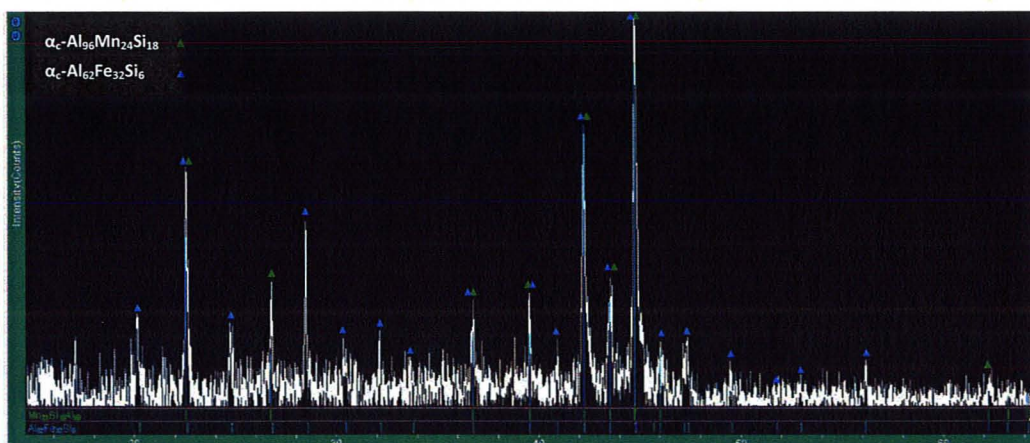


Figure 27 XRD result of alloy #3 (Fe=0.3 Si=0.45), Melt Spinner, Thickness = 150 μm , SUPER HEAT $\geq 1000^\circ C$

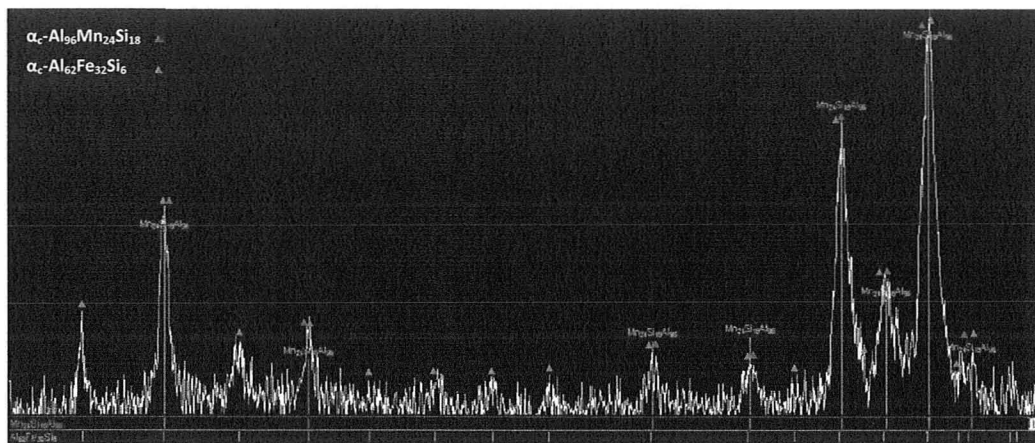


Figure 28 XRD result of alloy #4 (Fe=0.5 Si=0.2), Melt Spinner, Thickness = 150 μm , SUPER HEAT ≥ 1000 °C

Appendix 4: Solute redistribution (Scheil model, Lever rule)

During solidification of an alloying system, distribution of elements within solid and liquid occurs base on equilibrium phase diagram only if the following two diffusion processes are completely satisfied [Eskin 2008]:

1. Diffusion of the alloying elements in liquid to avoid solute pile-up (when partition coefficient K is less than unity) close to solid/liquid interface.
2. Diffusion of alloying elements in the solidified portion of the system to avoid the creation of concentration gradient within the solid phase.

These diffusion reactions are time consuming and as a result, due to the applied conditions during solidification in industrial processes (such as high cooling rates), these reactions remain incomplete. As a result, equilibrium phase diagrams can no longer be employed to predict solid and liquid compositions at different times and locations of the system.

In general, among different available models, "Scheil-Gulliver model*" and "Lever rule", which are attributed to the solidification under non-equilibrium and equilibrium conditions respectively, are commonly used for simulation of solute redistribution during solidification. These models are based on the following assumptions:

* This model was suggested by Gulliver in 1913 to 1922 and developed by Scheil in 1942 [Eskin 2008]

Lever rule ----> complete diffusion in both liquid and solid (no concentration gradient)

Scheil-Gulliver model ----> complete diffusion in the liquid and no solid-state diffusion

In Figure 1 an assumed concentration profile at solid/liquid interface and three boundary layers in liquid (A_1), in solid (A_3) and at the interface (A_2) are schematically shown.

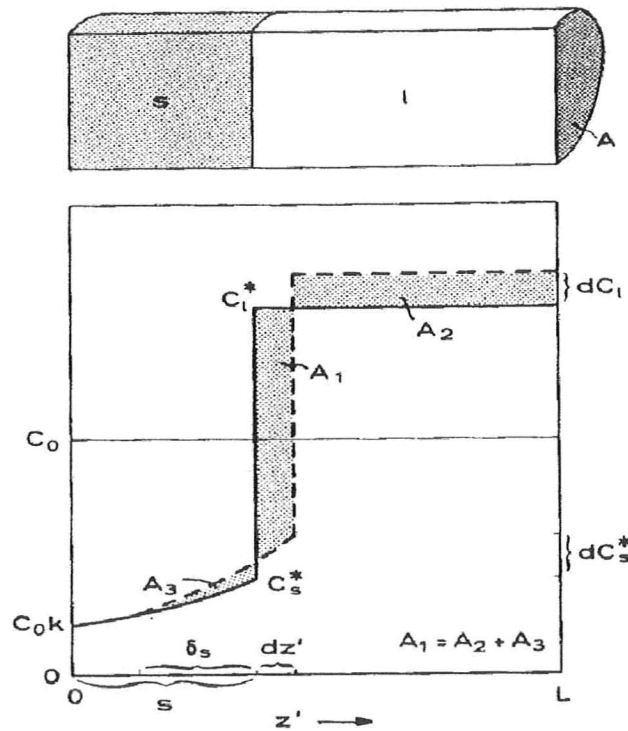


Figure 1 Schematic of concentration profiles in a solidifying system with complete liquid mixing and some solid state diffusion [Kurz 1986]

The mass balance is:

$$A_1 = A_2 + A_3$$

$$(C_l - C_s^*)df_s = f_l dC_l + \frac{\delta_s}{2L} dC_s^* \quad (1)$$

Knowing that

$$\left\{ \begin{array}{l} f_s = \frac{S}{L} \quad \text{Solid fraction} \\ df_s = \frac{ds}{L} \\ \delta_s = \frac{2D_s}{V} = \frac{2D_s dt}{ds} \quad \text{Diffusion boundary layer in the solid} \\ C_s^* = kC_l \quad \text{Interface concentration in the solid} \\ dC_s^* = kdC_l \end{array} \right.$$

Here L is the length of the solidifying system, D_s is the diffusion coefficient in solid (m^2/s) and k is the partition coefficient.

Then substitution into equation (1) gives the following:

$$\frac{dC_l}{pC_l} = \frac{df_s}{(1 - f_s) + 2\alpha k f_s} \tag{2}$$

Where

$$\left\{ \begin{array}{l} p = 1 - k \\ \alpha = \frac{D_s t_f}{L^2} \quad \text{Dimensionless solid-state back diffusion parameter} \end{array} \right.$$

And integration leads to: (3)

$$\frac{C_l}{C_s} = [1 - f_s(1 - 2\alpha k)]^{\frac{k-1}{1-2\alpha k}}$$

Clyne and Kurz in 1981 [Kurz 1986] proposed a modified version of solid state back diffusion parameter (α) which is presented bellow:

$$\alpha' = \alpha \left[1 - \exp\left(-\frac{1}{\alpha}\right) \right] - \frac{1}{2} \exp\left(-\frac{1}{2\alpha}\right)$$

In this modified version when α is very small (less than 0.1), $\alpha' = \alpha$ and when α is very large (greater than 50), $\alpha' = 0.5$.

Substitution of these values in equation 3 leads to the following equations corresponding to "Lever rule" (shown in Figure 2) and "Scheil-Gulliver model":

$$\alpha' = 0.5 \xrightarrow[\text{(Equilibrium condition)}]{\text{Lever rule}} \frac{C_l}{C_0} = \frac{1}{1 - pf_s}$$

$$\alpha' = 0 \xrightarrow{\text{Scheil_Gulliver}} \frac{C_l}{C_0} = \frac{1}{(1 - f_s)^p} = \frac{1}{f_l^p}$$

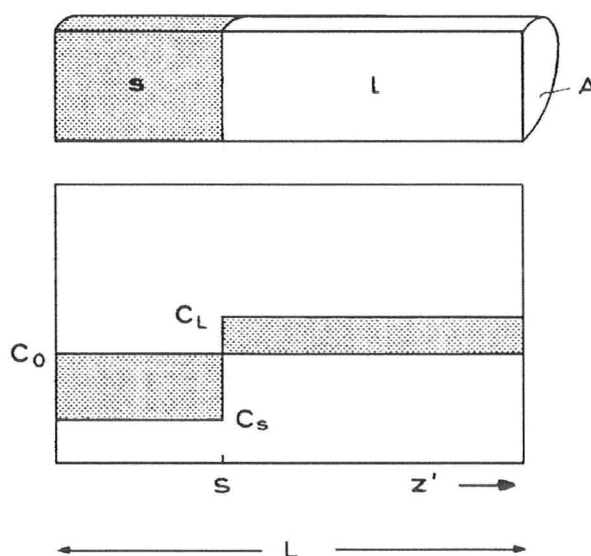


Figure 2 Solidification under equilibrium conditions (Lever rule) [Kurz 1986]

Appendix 5: Driving forces for onset of precipitation

From:

Purdy R.G., Malakhov D.V., Zurob H., "Driving forces for the onset of precipitation in the course of multicomponent alloys solidification", Proceeding of the 6th international school-conference, "Phase Diagrams In materials Science", MSI GmbH, (2004) 20-41

Driving force for onset of precipitation (D^α) of a phase (α) from a liquid with composition X_0^L is schematically shown in Figure 1.

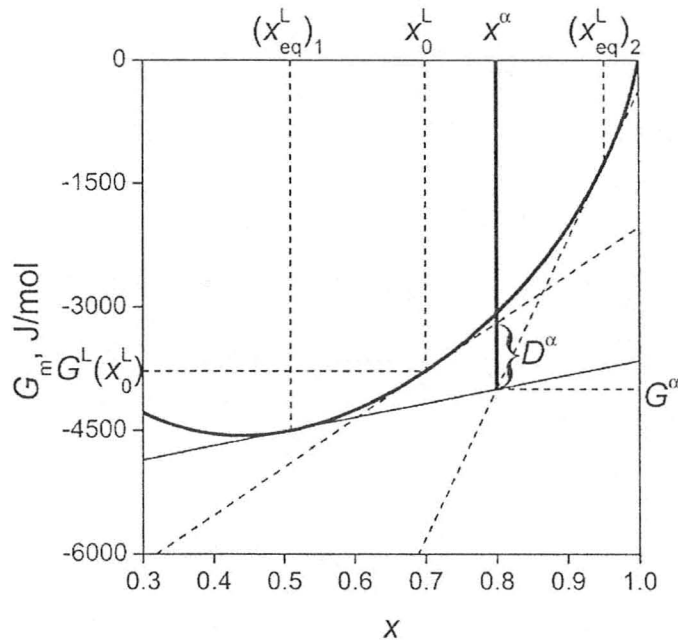


Figure 1 Illustration of the driving force for the beginning of precipitation of a stoichiometric binary phase α from a supersaturated liquid solution [Purdy 2004]

From this figure D^α can be written as:

$$D^\alpha = G^L(x_0^L) + \left(\frac{\partial G^L}{\partial x^L} \right)_{x_0^L} (x^\alpha - x_0^L) - G^\alpha$$

This equation can also be rewritten in the following way:

$$D^\alpha = G^L(x_0^L) + \left(\frac{\partial G^L}{\partial x^L} \right)_{x_0^L} (x^\alpha - x_0^L) - G^L(x_{eq}^L) - \left(\frac{\partial G^L}{\partial x^L} \right)_{x_{eq}^L} (x^\alpha - x_{eq}^L)$$

Expansion of $\left(\frac{\partial G^L}{\partial x^L} \right)_{x_0^L}$ and $G^L(x_{eq}^L)$ by using truncated Taylor's series and substitution leads to the following relation:

$$D^\alpha = (x^\alpha - x_0^L) \times \left(\frac{\partial^2 G^L}{\partial x^L^2} \right)_{x_0^L} \times (x_0^L - x_{eq}^L)$$

As seen, at low supersaturations, driving force D^α linearly depends on the supersaturation $x_0^L - x_{eq}^L$, on the difference between the initial composition of the liquid and forming stoichiometric phase $x^\alpha - x_{eq}^L$, and on the curvature of the concentration dependence of the molar Gibbs energy of the liquid phase $\left(\frac{\partial^2 G^L}{\partial x^L^2} \right)_{x_0^L}$.

Generalization of these results to a system containing K components gives:

$$D^\alpha = (x_2^\alpha - x_{2,eq}^L, \dots, x_K^\alpha - x_{K,eq}^L) \times \mathbf{H} \times \begin{bmatrix} x_{2,0}^L - x_{2,eq}^L \\ \vdots \\ x_{K,0}^L - x_{K,eq}^L \end{bmatrix}$$

where \mathbf{H} is the Hessian of the molar Gibbs energy.

Let us recall that precipitation of a phase (e.g. α) is possible only if $D^\alpha > 0$. Based on this, some concentration regions in which this minimum required condition (i.e. $D^\alpha > 0$) is satisfied, can be defined. It is worth mentioning that these regions named *nucleability regions* or *nucleability fields*, can not be span over the whole composition

range and as it is shown for α phase in Figure 2, are only seen in one connected region of concentration.

In the nucleability regions of " α " between $(X_{eq}^L)_1$ and $(X_{eq}^L)_2$, the driving forces for onset of precipitation are positive and α phase has the minimum required condition for nucleation.

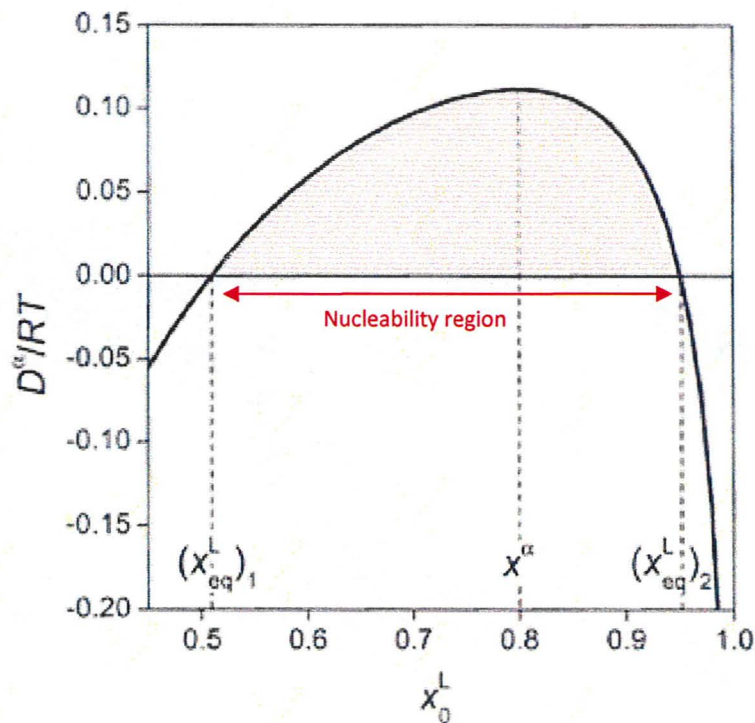


Figure 2 An example of how the driving force for the start of precipitation depends on the initial composition of melt [Purdy 2004]

In the case when two stoichiometric phases may have a chance to precipitate from the melt (Figure 3) the following equation can be written:

$$\begin{aligned}
 D^{\beta\alpha} &= D^{\beta} - D^{\alpha} \\
 &= \left[G^L(x_0^L) + \left(\frac{\partial G^L}{\partial x^L} \right)_{x_0^L} (x^{\beta} - x_0^L) - G^{\beta} \right] - \left[G^L(x_0^L) + \left(\frac{\partial G^L}{\partial x^L} \right)_{x_0^L} (x^{\alpha} - x_0^L) - G^{\alpha} \right] \\
 &= \left(\frac{\partial G^L}{\partial x^L} \right)_{x_0^L} (x^{\beta} - x^{\alpha}) - (G^{\beta} - G^{\alpha})
 \end{aligned}$$

Figure 4 shows the variation of the driving forces for onset of nucleation of α and β by changing the composition. It is worth noting that how the initial melt composition affects the driving forces for the start of precipitation of these phases.

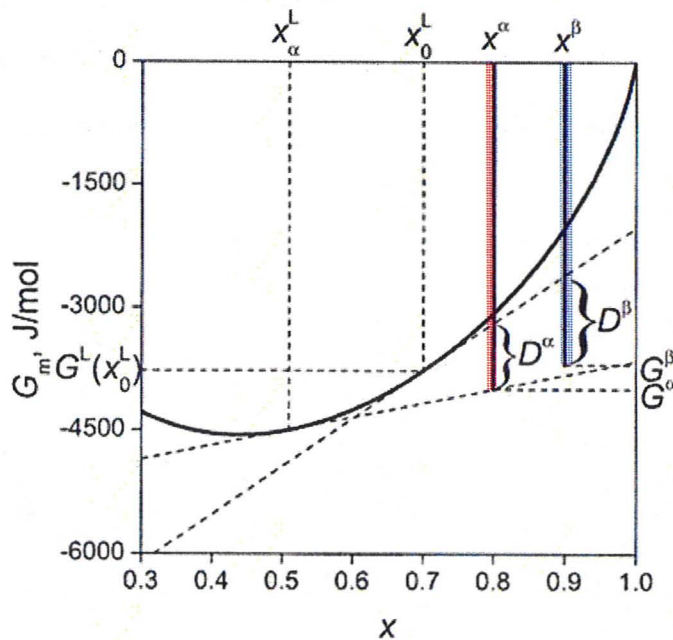


Figure 3 Driving forces for onset of precipitation of two competing stoichiometric phases [Purdy 2004]

It is demonstrated that by increasing supersaturation in the melt, the likelihood of the formation of β (metastable phase) is increased.

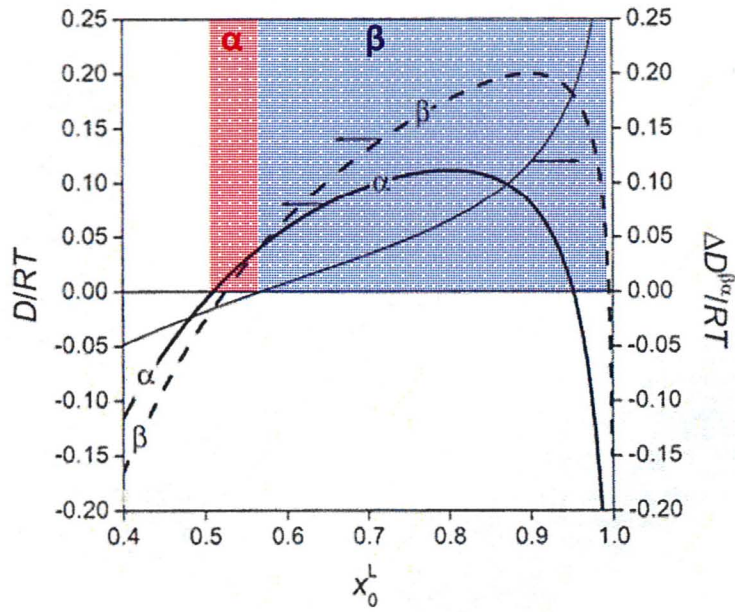


Figure 4 Illustration of how the likelihood of phase formation depends on the melt's composition [Purdy 2004]

Appendix 6: Heat equation (temperature profile)

Conduction heat transfer described by Fourier's law can be used to determine the heat flux vector, \mathbf{q} , for a given temperature profile in a system

$$\mathbf{q} = -K\bar{\nabla}T$$

where K is thermal conductivity ($\frac{W}{m.K}$).

Considering the law of conservation of energy, the following relation should be satisfied:

$$\begin{array}{ccccccc} \text{Heat} & & \text{Heat} & & \text{Heat} & & \text{Change of} \\ \text{conducted} & + & \text{generated} & = & \text{conducted} & + & \text{energy stored} \\ & & & & & & \text{within} \end{array}$$

The change of energy stored within a system ($\frac{W}{m^3}$) is attributed to the ability of that system to store heat by increasing its temperature

$$\frac{\partial U}{\partial t} = \rho c \frac{\partial T}{\partial t}$$

Where ρ is density of the system in which heat is stored and c is specific heat.

As a result the equation describing heat flow can be obtained as following (Figure 1)

$$\frac{\partial}{\partial x} \left(K_x \frac{\partial T}{\partial x} \right) + \frac{\partial}{\partial y} \left(K_y \frac{\partial T}{\partial y} \right) + \frac{\partial}{\partial z} \left(K_z \frac{\partial T}{\partial z} \right) + q'(x, y, z) = \frac{\partial(\rho c T)}{\partial t}$$

$$\nabla(K\nabla T) + q' = \frac{\partial(\rho c T)}{\partial t}$$

If thermal conductivity, K , and specific heat, c , are constant, then

$$a\nabla^2 T + \frac{q'}{\rho c} = \frac{\partial T}{\partial t}$$

Where $a = \frac{K}{\rho c}$ is thermal diffusivity which describes the rate at which heat diffuses through a system.

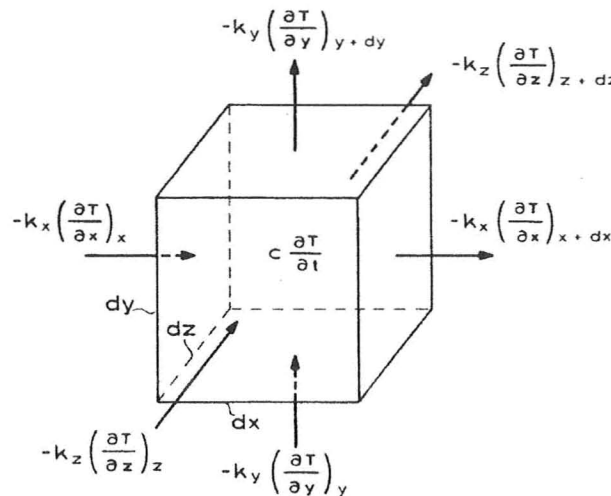


Figure 1 Heat balance in a three dimensional system [Kurz 1986]

It is worth mentioning that in the case of solidification, the heat source term, q' , contains the latent heat released at the solid/liquid interface. This release of latent heat can be linked to solidification front velocity and therefore to the amount of undercooling. For example, Chu *et.al.*[1985] used the following relations to simulate temperature profile in a ribbon of pure aluminum produced by a melt-spinner:

$$q' = R \cdot \frac{\Delta H_f}{\delta x} \left\{ \begin{array}{l} \Delta H_f = \text{latent heat of fusion} \\ \\ \delta x = \text{distance between} \\ \text{adjacent nodes in the} \\ \text{finite difference scheme} \end{array} \right.$$

The relationship used for growth velocity, R , was

$$R = 4.5 \times 10^{-2} \Delta T \quad \text{ms}^{-1}$$

Where ΔT is solid/liquid interface undercooling. The boundary conditions used

by Chu *et.al.* are

$$\left\{ \begin{array}{ll} x = 0 & -K \frac{\partial T}{\partial x} = -h (T - T_\infty) \\ \\ x = L & \frac{\partial T}{\partial x} = 0 \\ \\ \text{At solid/liquid interface} & q' = R \cdot \frac{\Delta H_f}{\delta x} \\ \\ & q' = 0, \quad \text{elsewhere} \end{array} \right.$$

Where L is the ribbon thickness and h is heat transfer coefficient which is usually considered between 10^3 to 10^4 up to around $10^6 \text{ Wm}^{-2}\text{K}^{-1}$ for melt spinning [Clyne 1984]

The obtained temperature profiles across a 100 μm melt spun ribbon and calculated solid/liquid interface velocities at different undercoolings are shown in Figure 2 and Figure 3.

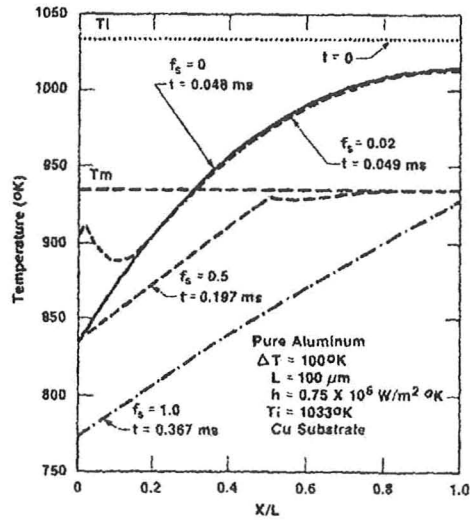


Figure 2 Calculated temperature profiles across a 100 μm Al melt spun ribbon during cooling and solidification (initial attained undercooling in this simulation is considered 100 K) [Chu 1985]

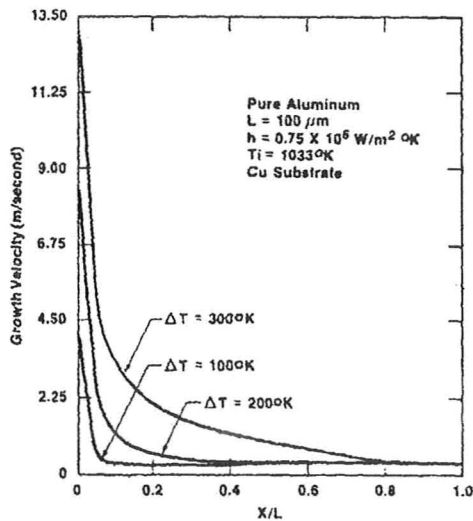


Figure 3 Calculate solid/liquid interface velocity V_s vs the position of the interface for different values of initial undercooling achieved in the region adjacent to the surface of the copper drum [Chu 1985]

References

- Allen C.M., O'Reilly K.A.Q., Cantor B., Evans P.V., "*Intermetallic Phase Selection in LXXX Al alloys*", Progress in Materials Science Vol.43 (1998) 89-170
- Allen C.M., O'Reilly K.A.Q., Evans P.V., Cantor B., "*A calorimetric evaluation of the role of impurities in the nucleation of secondary phases in LXXX Al alloys*", Mat. Res. Soc. Symp. Proc. Vol.481 (1998) 1-14
- Altenpohl D.G., "Aluminum: Technology, applications and environment" Sixth edition, TMS (1998), Chapter 6
- Bian X., Qin J., Wang W., Qi X. "*Medium range order and microstructure of Al-1% Fe alloy*", Materials Science Forum, Vol.331-337 (2000) 343-348
- Cahn J.W. "*The metastable liquidus and its effect on the crystallization of glass*", Journal of the American Ceramic Society, 52 (1969), 118-121
- Chu M. G. "*Microstructure and heat flow in melt-spun aluminum alloys*" Proceeding of international conference "Rapidly solidified alloys", (1985) 311-316
- Clyne T.W. "*Numerical treatment of rapid solidification*", Metallurgical Transactions B, Vol.15B (1984) 369-381
- Eskin D. G. "*Physical Metallurgy of Direct Chill Casting of Aluminum Alloys*" Fridlyander J.N. and Eskin D.G. (editors), CRC Press (publisher), 2008, P.28-43
- Feuerbacher B., "*Phase formation in metastable solidification*", Materials Science Reports, Vol. 4, No. 1 (1989) 1-40
- Griger A., Stefániay V., Kovács-Csetényi E., Turmezey T. "*Formation and transformation of binary intermetallic phases in high purity Al-Fe alloys*", Key Engineering Materials, Vols. 44 & 45 (1990) 17-30

Griger A., Stefaniay V., “*Equilibrium and non-equilibrium intermetallic phases in Al-Fe and Al-Fe-Si alloys*”, Journal of Materials Science, Vol.31 (1996) 6645-6652

Gupta A.K., Marois P.H., Lloyd D.J., “*Review of the Techniques for the extraction of second-phase particles from aluminum alloys*”, Materials Characterization, Vol.37 (1996) 61-80

Hillert M., “*Application of Gibbs energy-composition diagrams*” in *Lectures on the theory of phase transformations*, H.I. Aaronson (editor), Warrendale, Pennsylvania: TMS, 1999, P.1-33

Hillert M., Steffansson L.-I., “*The regular solution model for stoichiometric phases and ionic melts*”, Acta Chemica Scandinavica. 24 (1970), 3618-3626

Hughes I.R., Jones H., “*Coupled eutectic growth in Al-Fe alloys - Part 1 Effect of high growth velocity*”, Journal of Materials Science Vol.12 (1977) 323-333

Khalifa W., Samuel F.H., Gruzleski J.E, Doty H.W., Valtierra S., “*Nucleation of Fe-intermetallic phase in the Al-Si-Fe alloys*”, Metallurgical and Materials Transaction A, Vol. 36A (2005) 1017-1032

Khalifa W., Samuel F.H., Gruzleski J.E., “*Iron intermetallics phases in the Al corner of the Al-Fe-Si system*”, Metallurgical and Materials Transaction A Vol. 34A (2003) 807-825

Kral M.V., “*A crystallographic identification of intermetallic phases in Al-Si alloys*”, Materials Letters, Vol. 59 (2005) 2271-2276

Kral M.V., Nakashima P.N.H., Mitchell D.R.G., “*Electron microscope studies of Al-Fe-Si intermetallics in an Al-11 Pct Si alloy*”, Metallurgical and Materials Transactions A, Vol. 37A (2006) 1987-1997

Kurz W. Fisher D.J., “*Fundamentals of solidification*” Trans Tech Publications (1986)

Langsrud Y. "Silicon in commercial aluminum alloys-what becomes of it during DC-casting", Mechanical and Corrosion Properties series A. Key engineering materials, Vol.44-45 (1990) 95-115

Liang D, Jones H., "The effect of growth velocity on growth temperature of the Al-Al₃Fe and Al-Al₆Fe eutectics", Metallkde Vol.83(n.4) (1992) 224

Liu P., "Crystal structure determination of Al-Fe-Si phases by Convergent-Beam Electron Diffraction (CBED)", Key Engineering Materilas, Vols 44 & 45 (1990) 69-86

Miroshnichenko I.S., "Broadening of the region of primary solid solution in alloys of eutectic and peritectic type" In Crystallization process. N.N. Sirota, F.K. Gorskii, V.M. Varikash (editors), New York: Consultant Bureau, (1966), P.55-59

Perepezko J. H., Uttotmark M. J, "Undercooling and nucleation during solidification", ISIJ international, Vol. 35, No. 6 (1995) 580-588

Pettersen T., "Phase transformation for primary particles in the surface regions of an AA1200 alloy" Materials Science Forum, Vols. 539-543 (2007) 311-316

Plunkert P.A., "Aluminum", USGS reports, 1999

Porter D.A., Easterling K.E., "Phase transformation in metals and alloys" Second edition, Nelson Thornes Ltd, reprinted in (2001), Chapter 4 page 185.

Purdy R.G., Malakhov D.V., Zurob H., "Driving forces for the onset of precipitation in the course of multicomponent alloys solidification", Proceeding of the 6th international school-conference, "Phase Diagrams In materials Science", MSI GmbH, (2004) 20-41

Simensen C.J., Vellasamy R., "Determination of phases present in cast material of Al 0.5 Wt % Fe-0.2 Wt% Si alloy", Z.Metallkde Vol.68 (1977) 428-431

Sha G., O'Reilly K.A.Q., Cantor B, "Characterization of Fe-rich intermetallic phases in 6xxx series Al alloy", Materials Science Forum, Vol. 519-521 (2006) 1721-1726

Skejerpe P., Gjønnnes J. "*Structure and primary Al-Fe-Si particles in direct-chilled-cast aluminum alloys*", Ultramicroscopy Vol.22 (1987) 239-250

Skejerpe P., "*Structure of Al_mFe* ", Acta Crystal, B44 (1988) 480-486

Skejerpe P., "*Intermetallic phases formed during DC-casting of an al-0.25 wt Pct Fe-0.13 Wt Pct Si alloy*", Metallurgical Transactions A. Vol.18A (1987) 189-200

Smolej A., Slacek E., Turk R., "*State and development of some wrought aluminum alloys for special and general applications*", METABK Vol. 41(3) 149 (2002)

Stone I.C., Jones H., "*Effect of cooling rate and front velocity on solidification microstructure selection in Al-3.5 wt.%Fe-0 to 8.5 wt.%Si alloys*", Materials Science and Engineering A226-228, (1997) 33-37

Takeshita K., Shingu H.P., "*The undercooling attainable by rapid quenching of Al-CuAl₂ eutectic alloy melt*", Transactions of the Japan Institute of Metals, Vol.27 No.3 (1986) 180-186

Tibballs J.E., "*Al-Si substitution in Al(Fe,Mn)Si phases*", Key Engineering Materials, Vols. 44 & 45 (1990) 233-246

Todd I, Jones H., "*The effect of cumulative alloying additions on intermetallics phase selection in alloys based on Al-0.5 wt.%Fe*", Materials Science Forum, Vols. 217-222 (1996) 201-206

Turmezey T., Stefániay V., Griger A., "*AlFeSi phases in aluminum*", Key Engineering Materials, Vols.44 & 45 (1990) 57-68

Venkataramani R, Simpson R., Ravindran C., "*Effect of superheat on maximum nuclei density in A356 alloy*", Materials Characterization, Vol.35 iss.1 (1995) 81-92

Wang Y., Jones H. Evans P.V., "*Eutectic solidification characteristics of Bridgman grown Al-3Fe-0.1V alloy*", Journal of Materials Science 33(1998) 5205-5220

Warmuzek M., Gazda A., "*An analysis of cooling rate influence on intermetallic phases precipitation in some commercial aluminum alloys*", Journal of Analytical Atomic Spectrometry, Vol.14 (1999) 535-537

Westengen H., "*Formation of intermetallic compounds during DC casting of a commercial purity Al-Fe-Si alloy*", Z.Metallkde 73 (1982) 360-368

Young R.M.K., Clyne T.W., "*Al-Fe intermetallics formed during controlled solidification*", Scripta Metallurgica Vol.15 (1981) 1211-1216

Zheng J.G, Vincent R., Steeds J.W., "*Crystal structure of an orthorhombic phase in β -(Al-Fe-Si) precipitates determined by convergent-beam electron diffraction*", Philosophical Magazine A, Vol.80, No.2, (2000) 493-500